Characteristics of Forward Energy Production in Proton-Nucleus and Pion-Nucleus Collisions at $\sqrt{S} = 31.5$ GeV

A THESIS

SUBMITTED TO THE FACULTY OF THE GRADUATE SCHOOL

OF THE UNIVERSITY OF MINNESOTA

BY

Richard Scott Benson

IN PARTIAL FULFILLMENT OF THE REQUIREMENTS

FOR THE DEGREE OF

DOCTOR OF PHILOSOPHY

December 1989

/

AAB/792

Abstract

The construction and performance of a high energy particle calorimeter is described. Its operation in Fermilab's experiment 706 during 1987 through 1988 is discussed in the context of the experimental objectives. Correlations between the measured energy of particles striking this detector with kinematics of the remainder of the event is investigated. Comparisons to a monte carlo simulation are presented.

Adviser/Chairman

ACKNOWLEDGEMENTS

It is fair to say that hundreds of people have been brought togeather on the project described in this dissertation. I would like to take this opportunity to thank a few of them.

I would like to express my sincere thanks to my adviser, Keith Ruddick, and my mentor Pat Lukens. If there is any worth in this thesis then the credit must surely go to them.

I would also like to thank my collegues from Fermilab experiment 706: G. Alverson, W. Baker, G. Ballocchi, D. Berg, C. Bromberg, D. Brown, D. Carey, C. Chandlee, B.C. Choudhary, L. DeBarbaro, W. DeSoi, S. Easo, E. Engels, Jr., W. Faissler, G. Fanourakis, T. Ferbel, D. Garelick, G. Ginther, G. Glass, M. Glaubman, P. Gutierrez, K. Hartman, J. Huston, C. Johnstone, H. Johnstad, U. Joshi, V. Kapoor, I. Kourbanis, A. Lanaro, C. Lirakis, F. Lobkowicz, S. Mani, J. Mansour, R. Miller, C.A. Nelson, Jr. A. Nguyen, B.Y. Oh, D. Orris, G. Pedeville, E. Pothier, E. Prebys, P.F. Shepard, R. Shivpuri, A. Sinanidis, D. Skow, P. Slattery, W. Toothacker, N. Varelas, P.D.D.S. Weerasundara, J. Whitmore, G.-H. Wu, T. Yasuda, C. Yosef, M. Zielinski. They are E706.

I owe a great debt of gratitude to my family and friends as they were my carrot when the rest of the world seemed only to offer a stick.

I would like to thank my eldest brother, David. His questions to me as a child led me to see that understanding things deeply does not diminsh, but enhances the wonder of their being. This is undoubtably the single most important motivation for my fascination with elementary particles.

Finally, I would like to thank you, the reader, for taking an interest in finding out more about what I have done. I would also like to take this opportunity to relate an allegorical tale which may make what follows seem a bit more worthy of your consideration. It concerns a person who came upon two stone masons who were hard at work chipping huge stone blocks from the side of a quarry. The person asked the first what he was doing and received the reply "I'm making stone blocks.". This was an honest answer, however the person was not satisfied by it. And so he asked the second mason "And what are you doing?". "I'm building a cathedral.", he said.

Table of Contents

CHAPTER I. INTRODUCTION

In this thesis we describe the construction and performance of a calorimeter which measured the energy of particles produced at very small angles from the beam axis in high energy interactions of 530 GeV mesons and protons. The calorimeter was a major component in an experiment at Fermilab (E706). Particles which strike this calorimeter are said to form a forward jet and we present results of a study of correlations between this forward jet and particles detected elsewhere in E706. We also compare the experimental data to predictions generated by a widely accepted model of high energy particle collisions (ISAJET). Agreement is found between E706 and other experiments for the dependence of particle multiplicities on the energy available for multiparticle production. We find that there appears to be a significant anti-correlation between the transverse component of momentum P_{T} of the forward jet and that of other high P_{T} particles observed in events with large momentum transfers.

In order to expedite the following discussions a brief digression into the definitions of some kinematical variables and theoretical background is necessary.

§ I.1. Nomenclature

All particles fall into one of two broad categories: elementary or composite. Elementary particles such as electrons, photons, quarks and gluons (e, γ, q, g) are the more fundamental of the two as they can not be decomposed into constituent particles. Of these fundamental particles, the gluons and quarks are the only ones to participate in the strong force and they are referred to as partons. Composite particles, on the other hand, are formed from combinations of partons. Protons,

neutrons, pions and kaons (p, n, π, K) are all composite particles. From the point of view of very high energy collisions the pion, for example, can be decomposed into a quark, an anti-quark and an indefinite number of gluons. Very high energy collisions between composite particles may exhibit characteristics which are due to the nature of their parton substructure.

A very energetic collision will occur when one of the partons of the incident particle makes a direct hit on one of the partons in the target as is shown in figure 1. The partons which do not collide are referred to as "spectators" and proceed directly through this stage of the interaction without any change to their initial conditions. The hard scattered partons are deflected through large angles from their previous trajectories while spectators remain confined to relatively narrow cones in the forward and the backward directions relative to the beam-target axis, as illustrated in figure 2. Thus, particles emerging from very energetic collisions are grouped into three categories corresponding to the region where the underlying partons are believed to have been sprayed. We can identify these three categories as the forward (beam spectators), backward (target spectators) and central (hard scattered) regions.

A very useful parameter for determining which region a given secondary particle belongs to is the rapidity y and its relativistic approximation the pseudorapidity η. These are defined as

$$y = \frac{1}{2}\log_e\left(\frac{\mathrm{E} + \mathrm{p_z}}{\mathrm{E} - \mathrm{p_z}}\right) \tag{I.1}$$

$$\eta = -\log_e\left(\tan\left(\frac{\theta}{2}\right)\right) \tag{I.2}$$

where E = energy, z = axis along which the particles collide, p_z = component of momentum along the z axis and θ = angle between the z axis and the outgoing particle. One elegant feature of these variables is that a transformation from the center of momentum frame to any frame moving at constant velocity along the z axis simply produces an offset without any scale change, i.e. $\eta \rightarrow \eta' = \eta + constant$. Consequently the shapes of all distributions which are a function of these parameters remain invariant under such transformations. In the center of momentum frame the central region falls symmetrically about $\eta = 0$.

The total energy in the center of mass for fixed target experiments at very high energies is $\sqrt{S} = \sqrt{2m_{proton}E_{Beam}}$. For example, in E706 we used a beam of protons with a momentum of 530 GeV/c which struck another proton (or neutron) in the target and so $\sqrt{S}$ = 31.5 GeV. The maximum rapidity in pp collisions in the center of mass frame can be written $y_{max} = \log_e(\frac{\sqrt{s}}{m_{proton}}) = 3.5$ for this experiment. All particles fall within the rapidity interval from [-3.5,+3.5] in the center of momentum frame.[#1] The central region referred to above is the region from -1. to +1. while the forward region corresponds to the interval from $\approx +1$ to $\approx +3.5$.

The z axis is always chosen to represent the axis along which the particles collide and so the component of momentum transverse to this axis $P_T = \sqrt{p_x^2 + p_y^2}$ will always be zero in the initial state. Nonzero P_T in the final state must arise from interactions between the particles. High P_T final states correspond to "hard" scattering subprocesses. Very hard scattering is due to interactions between constituents.

#1 Or [0.,+7.] in the lab frame

Figure 3 shows the pictorial representation of a quark scattering off of a gluon. Since partons are bound by the strong force they do not escape from these processes without further interactions with the field. Instead, they produce cascades of additional particles (or "jets") that ultimately condense into hadrons that can be observed in the laboratory. This should be contrasted with figure 4 showing the identical process with the outgoing gluon replaced by a photon. In this latter process one would anticipate that the photon would escape from the interaction while the remaining quark would generate a spray of particles in the course of hadronization. A judiciously placed photon detector could measure these direct photons and utilize this information to probe the strong coupling. This was the primary objective in E706. However, the apparatus also allows one to explore the physics of the forward jet and the dependence of associated particles on the forward jet. This is the topic of this dissertation.

Perhaps the most profound difference between the study of the forward jet and that of most other types of elementary particle studies is that the forward jet is inextricably connected to the hadronization process. The fragmentation of the partons into the sprays of particles can be described by many means, although the understanding of how these processes are connected to the underlying force(s) is tenuous at best. The reason for this lies in the distinction between perturbative and non-perturbative processes.

Perturbative processes are those which can be represented by a polynomial expansion of the underlying subprocesses in powers of a coupling constant α which is characteristic of those subprocesses. For this procedure to be valid, the polynomial series must converge. Convergence is usually associated with $\alpha \ll 1$.

In this case one expects to have a relatively precise prediction after calculating the first few terms in the series. The catch here is that α (for the strong force) isn't a constant! In fact α is a function of the magnitude of the square of momentum transfer Q^2 as shown in figure 5. Consequently, as Q^2 becomes small, $\alpha(Q^2)$ becomes large. In practical terms this means that one can not use perturbation theory for processes in which Q^2 is on the order of the Fermi energy of the partons $k_t \approx 200$ MeV/c. In practice one typically stays well above 1 GeV/c when measurements are to be compared to a perturbative calculation such as in the direct photon process.

One common measurement in a typical particle experiment consists in the identification of specific event topologies (e.g. events with a very high P_T particle) and determining the probability of their occurrence within specific regions of phase space.[#2] The most common measurement is referred to as the cross section σ and is expressed in units of an area.

The structure function can be thought of as the probability of a particle existing in a specific region of phase space. Each parton has its own characteristic structure function.

It is the intention of E706 to measure differential cross sections for the production of direct photons. These differential cross sections can then be combined with the electromagnetic structure functions (which are measured in e^+e^- experiments) to determine the gluon structure function.

#2 Phase space refers to a coordinate system where the energy and momenta of the constituents define the axes. Conservation laws, coupled with the initial conditions, determine the kinematically accessible region of phase space to which most measurements are normalized.

§ I.2. Review of Related Developments

For very low momentum transfers (e.g. in the spectator region) very little is known about the non-perturbative mechanisms which describe the interactions. Despite this difficulty a large number of experiments have investigated non-perturbative processes and many models have been quite successful in duplicating the data.[1] One very exciting discovery in this field was the prediction by Koba, Nielsen and Olssen[2] and confirmed with experimental data by Slattery[3] demonstrating a scaling (KNO scaling) of the charged particle multiplicity distributions with $\sqrt{S}$ at energies below a few hundred GeV. More recent work at CERN by the UA5 collaboration[4] has shown that this scaling law is violated at higher energies indicating the possible onset of new processes in the underlying particle production mechanisms. A particularly elegant explanation of this phenomena was formulated by Rudaz and Valin[5] who reason that what is being observed in violations of KNO scaling is the transition from lower energy multiparticle production processes that are entirely dominated by the quark fragmentation characteristics to higher energy processes in which the contributions due to (soft) gluons have become a significant factor. Rudaz and Valin predict that as $\sqrt{S}$ is increased still further one will enter a regime where the multiparticle production processes are entirely dominated by the gluons, and that the KNO scaling previously encountered at lower energies will be recovered albeit with a parametrization that is now characteristic of gluons rather than quarks.

The energy dependence of charged particle multiplicities was investigated by Brick et al[6] for a number of incident beams and nuclear targets and found to be independent of beam type and to scale in a simple way with the "inelasticity",

$K = \frac{\text{Energy in central region}}{\text{Total Energy}=\sqrt{S}}$.

Theoretical progress on the shape of the energy spectrum in the central region has resulted in predictions[7,8] which appear to describe the data over a wide range of energies[9] for the inelasticity as a function of $\sqrt{S}$. The evolution of the inelasticity with $\sqrt{S}$ is especially pertinent to extrapolations of particle multiplicities expected in the detectors at future accelerator facilities (e.g. SSC) since the inelasticity gives a measure of how much energy exists in the central region and is available for multiparticle production. In a fixed target experiment such as E706 the inelasticity is essentially $K = 1 - \frac{E_{forward}}{E_{Beam}}$.

Fermilab's experiment E260 showed that the forward scattering cross sections for events triggered by a small single-arm spectrometer at $\theta_{\rm cm} = 90°$ could be fit to a hard scattering model.[10] They also found the fragmentation functions for the forward going particles, $f(x) = \frac{x}{\sigma}\frac{d\sigma}{dx}$ scaled with the E_t dependent variable $x = \frac{2p_L}{(\sqrt{S}-\alpha E_t)}$.[#3] Yet measurements of charge flow in pp collisions[11] have also shown that the leading particle does not contain all the kinematical information of the forward spectator jet. Consequently it is of interest to inquire how much the kinematics of the (multiparticle) forward jet are dependent upon the processes taking place in the central region.

Another exciting development, addressed in a recent series of papers[12], concerns the clustering of particles in rapidity space and has led to speculations that the underlying multiparticle production mechanisms are essentially chaotic

---

#3 The denominator here is a measure of the total energy in the forward cone while p_L is is the longitudinal component of momentum and α is a parameter (< 1) fit to the experimental data. In effect, this variable is very similar to the inelasticity in characterizing how much energy is in the central region.

(i.e. scale invariant and self similar) and may even exhibit fractal characteristics. There have also been reports[13] that measurements of the beam jet in pp and $p\bar{p}$ collisions at $\sqrt{S} = 27.4$ GeV demonstrate a transition from diquark to single quark characteristics as the transverse energy of the jet increases. In addition, there are indications from the CERN experiment NA22 that the beam jet structure in pp and $p\bar{p}$ collisions differ in ways not well described by currently accepted phenomenological models.[14] Clearly there is much more to be understood about the characteristics of these processes which dominate the hadronization process.

Taken together, these developments, along with the extremely scarce body of information on the forward jet in hadronic collisions, provide a strong motivation for the study of the forward jet in this experiment. In the remainder of this introduction I indulge in a brief survey of the endeavor in the broader context from which it springs: philosophy.

§ I.3. Philosophical Context

Throughout history human beings have developed philosophical models which place their experiences in the context of a rational structure and which thereby imbues their experience with the merit of a recognizable order. As humankind has evolved these models were required to account for an ever greater and sublime range of experiences and so many aspects of the models were modified. Around 350 BC Aristotle introduced a method of inquiry (the "scientific method") in order to provide guidelines by which to evaluate the validity of propositions regarding physical processes. This procedure was largely ignored and its application to practical circumstances were frequently misunderstood. However, it has

gradually established dominance in the field of natural philosophy.

By the twentieth century this procedure, coupled with careful observation and extremely sensitive measurements, has produced a (mathematical) model of natural phenomena commonly referred to as "the standard model". This model is capable of accounting for a very broad range of experimental measurements. Characteristics which tend to be the most troublesome for the standard model are those which fall into the non-perturbative regime described above and which often contain aspects which are intractable with any of the currently available computational tools.

By 1935 Karl Popper[15] had clearly shown how it is a logical truism of any scientific inquiry that a finite amount of data can never absolutely confirm a given proposition. In every theory it will always be possible to contrive a competing theory with an expanded set of assumptions and which mimics all the phenomena predicted by the initial theory. Any truly distinct (competing) theory must contain additional properties not present in the initial theory and which current data may be unable to resolve. Consequently, one can only disprove theories and may never truly prove them in any absolute sense. Strictly speaking, one may only claim that specific sets of data are either consistent or inconsistent with a particular model. For this reason scientist strive to push the limits of the comparison between the model(s) of physical phenomena and the data as far into the most troublesome areas of correlation as possible so that they might expose regions where the theory and the data diverge and thus obtain new clues as to what properties an expanded theory must posses.

Seen in this context, the comparison of the centrally produced high P_{T} parti-

cles with the forward jet is to some extent the connection of the well understood[#4] perturbative regime with the poorly understood[#5] nonperturbative regime. Indeed one may ultimately constrain the theory using these correlations of the perturbative and nonperturbative regimes. While much of the present work may seem suggestive of how this may occur it is by no means obvious how to proceed in that attempt.

REFERENCES

[1.] J.G. Rushbrooke, Proceedings of XIV International Symposium on Multiparticle Dynamics (1983) p. 542.

[2.] Koba et al, Nuclear Physics B40 (1972) 317.

[3.] Slattery, Physical Review Letters Vol 29 No. 24(1972) 1624.

[4.] UA5 collaboration, Physics Letters Vol. 138B No. 4(1984).

[5.] Rudaz & Valin, Physical Review D, vol. 34 No. 7 (1986) 2025.

[6.] Brick et al Physics Letters Vol. 103B, No. 3 (1981)241, Physical Review D Vol. 39, No. 9 (1989) 2484.

[7.] G. Wilk, Fermilab preprint No. 78,221.

[8.] Watanabe & Tone, Physical Review D 39 (1989) 195.

[9.] Fowler et al, Fermilab preprint No. 74,130.

#4 I.e. in the sense that the theory correctly reproduces measured values (to over 12 decimal places in the case of measurements of certain atomic spectra).

#5 i.e. in the sense that the data is described primarily by phenomenological models and are often insoluble *in principle* using any know computational technique. Parton confinement is a good illustration of such a problem in this regime.

[10.] Bromberg et al, Physical Review Letters 45 (1980) 769.

[11.] Ahn et al, Physics Letters B 177 (1986) 233.

[12.] W. Kittel, Mini-Rapporteur's Review at the XXIV International Conference on High Energy Physics, Munich, August 4-10, 1988.

[13.] Ahn et al, Physics Letters B, Vol. 183 No.1 (1987) 115.

[14.] W. Kittel, Fermilab preprint No. 82,815.

[15.] K.R. Popper, The logic of scientific discovery, 1934.

CHAPTER II. APPARATUS:BEAMLINE AND DETECTORS

In this chapter we describe the equipment shown in figure 6 which was used in the execution of this experiment. After a brief overview of the entire experiment in which each device is introduced, a more detailed description of each subsystem will be given. The description of the most downstream detector, the forward calorimeter, is reserved for the next chapter as it represents the primary source of data for this dissertation.

§ II.1. Overview

The primary design objective of Fermilab experiment 706 was the study of direct photons produced in high energy collisions between a variety of hadrons and nuclear targets. These hadrons were produced by a beam of 800 GeV protons striking a piece of aluminum over 300 meters upstream of the experimental target. The secondary beam was momentum selected through a series of remotely controlled apertures and dipole and quadrupole magnets to have an energy of 530 GeV with a spread of 53 GeV. Before this secondary beam arrived in the experimental hall the incident particles were identified with a Cherenkov detector.

The targets for the experiment consisted of multiple layers of aluminum, beryllium, carbon or copper. Scintillation counters were arranged to detect not only the passage of the incident (beam) particle, but also particles which resulted from collisions between the beam particle and the target. Counters were placed upstream of the target to define the incident beam. A set of four counters downstream of the target detected products of interactions. Finally, a Veto Wall,

consisting of two planes of counters, detected the presence of so called "halo" particles in the annular region around the beam axis. These halo particles were mainly muons and remnants of collisions along the beamline upstream of the target which were traveling roughly parallel to the beam axis.

In order to reconstruct both the energy and momentum of each outgoing particle, in addition to the sign of the particle's electric charge, we placed a charged particle spectrometer downstream of the target. The spectrometer consisted of a set of Silicon microStrip vertex Detectors (SSD's) followed by a series of Multi-Wire Proportional Chambers (MWPC's) with a large aperture, high field dipole magnet between them. Neutral particles remained undetected and undeflected by these devices.

All particles between -1 and +1 unit of rapidity in the center of momentum frame were detected by a pair of very large calorimeters immersed within a common dewar of liquid argon. The liquid argon acted as the sensitive medium in the calorimeters. Since high P_T particles were of primary interest for the objectives of E706, and these particles fall predominantly in the central region, the liquid argon calorimeters were designed to straddle this region of rapidity symmetrically. The first of the calorimeters was optimized for the detection of photons and electrons and was named the Photon (or Electromagnetic) Calorimeter. Since hadrons are much more penetrating than either photons or electrons, a second calorimeter placed just downstream of the photon calorimeter detected hadronic energy primarily and so was named the Hadron Calorimeter. These calorimeters enabled the identification of individual particles under most circumstances and permitted a precise determination of the particles' position and total energy.

They also allowed for the formation of a prompt P_T signal for trigger purposes.

Both the Photon and Hadron Calorimeters were manufactured with a relatively large hole about the beam axis through which undeflected and only slightly deflected particles might pass without ever interacting with one of the detectors. This hole allowed for a very high intensity incident beam and thereby a high interaction rate without simultaneously overburdening the data acquisition system or saturating the sensitive regions of the detectors. However, this did leave a large gap in the coverage of the forward region which was filled by a third calorimeter placed immediately downstream of the other two calorimeters. This Forward CALorimeter (FCAL) intercepted the forward jet of particles and measured their total energy.

The remainder of this chapter is devoted to a series of sections which describe each of the preceding elements in much greater detail. These sections are arranged according to the position of the apparatus along the beam direction and constitute a detailed description of the apparatus without any pretense at being truly exhaustive.

§ II.2. Beamline

A diagram of the beamline for E706 (MW9) is shown in figure 7. The primary beam consisted of 800 GeV protons with an intensity which varied between 5 x $10^{11} \rightarrow 2$ x 10^{12} particles/spill over the course of the run. The primary proton beam struck production targets composed of $\frac{3}{4}$ and 1 interaction length(s) of aluminum located a distance 313.6 meters upstream of the secondary target.

This produced secondary beams of 530 GeV hadrons with an intensity between $1 \rightarrow 7 \times 10^7$ particles/spill.

The 1987-88 Fermilab spill structure maintained 18.8 nS separation between adjacent RF "buckets".[#6] The probability of two particles occupying the same RF bucket was $\approx$ 3% (10%) for the negative (positive) beam. Considering that the typical interaction rate was $\approx$ 10% in the secondary target this meant that $\approx$ 5% of all interactions (or 0.5% of all occupied beam buckets) contained two simultaneous parallel interactions overlapping each other. This potentially troublesome problem was averted by identifying such events with a high resolution vertex detector (SSD) and a forward calorimeter (FCAL) so that the background from this process was far below the experimental sensitivity. The mean separation between occupied beam buckets was $\approx$ 5 (i.e. 94 nS) under normal operating conditions.

§ II.3. Differential Cherenkov Detector

The Differential Cherenkov Detector, seen in figure 8, was located 253 meters downstream from the primary target and 60 meters upstream from the secondary target. Helium gas was used as the radiator in a volume 42.1 meters long. The temperature inside the chamber was held to within 0.1°F with a series of computer controlled temperature probes in combination with a 1" thick insulating layer of *Flex-sulation•X*. The gas pressure was remotely monitored and manually adjusted throughout the course of the run. The pressure was maintained

#6 An RF "bucket" is the valley in the electromagnetic wave which contains and accelerates the charged particle through the beamline.

to within 0.01 psi ($\frac{\Delta P}{P} = 0.18$ %) of the nominal value during all phases of the data taking. The inner (coincidence) and outer (anti-coincidence) readout rings contained 6 photomultipliers each.

A Cherenkov detector exploits the property that charged particles passing through any material radiate (Cherenkov) light at an angle θ given by the expression $\cos\theta = (n\beta)^{-1}$ where n is the index of refraction and $\beta = \frac{\text{Velocity}}{\text{Speed Of Light In Vacuum}}$. Note that when the momentum is held constant, θ depends only on the mass of the particle. The index of refraction n depends on the gas pressure as $(n-1) \propto P$. Therefore the angle θ associated with a particle of constant energy can be adjusted simply by adjusting the gas pressure.

The efficiency for particle identification depends upon the combination of coincidence and anti-coincidence signals used to define the particle type. Two distinct Cherenkov profiles were used in our analysis: one for positive and one for negative. Particles which matched the criteria for which the Cherenkov detector was set were said to be "tagged". The Cherenkov detector tagged K^-'s on the negative beam and π^+'s on the positive beam (i.e. the minority particle). Untagged particles were presumed to be pions and protons (i.e. the majority particles) respectively. Contamination levels were calculated to vary between $\approx 1 \rightarrow 8\%$ and depended upon the combination of coincidence and anti-coincidence channels and with the particle type.[16] Pressure curves for both the positive and negative beams, shown in figure 9 and figure 10, indicate that the secondary beam's composition was:

Table 1 **Table of beam composition in E706 during 1987 → 1988**

POSITIVE BEAM	NEGATIVE BEAM
$p = 91.2 \pm 0.1\%$	$\bar{p} = 0.20 \pm 0.01\%$
$\pi^+ = 7.2 \pm 0.2\%$	$\pi^- = 96.9 \pm 0.20\%$
$K^+ = 1.7 \pm 0.1\%$	$K^- = 2.90 \pm 0.20\%$

Muon contamination within the secondary beam was measured to be 0.4% (0.5%) in the positive (negative) beam. An analysis based on calibration data for the forward calorimeter and monte carlo simulations indicate that $\frac{\Delta p}{p}$ for the secondary beam was $\approx 5\%$.

§ II.4. Hadron Shield

A hadron shield, shown in figure 11, was installed 2.7 meters upstream of the secondary target to reduce the contamination from hadrons in a halo around the secondary beam. This shield was formed from 557 tons of iron[#7] stacked in two cantilevered piles 1.9 m wide by 3.6 m high by 4.7 m long. The central gap in the hadron shield was filled by a 44 ton blade of stainless steel with dimensions of 0.3 x 3.6 x 4.7 m^3. This blade could be removed to facilitate calibration of the detectors by sweeping the beam vertically across their faces. A vacuum pipe containing the beam extended through the midline of the blade and terminated in a window of 0.003" thick titanium. A search for events with a vertex originating in this beam window uncovered no candidates.

#7 This was armour shielding salvaged from the battleship Virginia.

§ II.5. Veto Wall

A pair of veto walls composed of scintillation counters, seen in figure 12, was installed immediately downstream of the hadron shield and covered a total area of 260 x 260 cm^2.These walls contained 4 symmetric quadrants with each quadrant housing 8 overlapping scintillators for a total of 32 independent scintillation counters in each wall. The veto wall was designed to detect muons passing through the hadron shield and generated a trigger veto signal whenever at least one of the 32 plates in each of the two veto walls generated a signal. A 2" thick layer of lead with a 1" diameter hole was placed immediately upstream of the target assembly to reduce false veto signals which might arise from particles scattered backwards from the target towards the veto wall.

§ II.6. Beam and Interaction Counters

The beam was defined by the scintillation counters BA, BB as shown in figure 13. Both BA and BB were solid rectangular pieces of scintillator 2.54 x 2.54 x 0.15 cm^3 centered on the beamline. BA was located $\approx$ 162 cm upstream of the downstream end of the targets while BB was located immediately downstream of BA. The Beam Halo counter BH was a rectangular piece with dimensions of 12.7 x 12.7 x 0.65 cm^3 with a hole 0.95 cm in diameter centered on the beamline 3.0 cm downstream from BB. The discriminated signals from these detectors were collected in scalers, and the coincidence BA$\bullet$BB$\bullet\overline{\text{BH}}$ $\equiv$ BEAM was required in all triggers for the experiment.

Four "interaction" counters (SE1, SW1, SE2 and SW2) consisted of rectangular scintillation counters each with a semi-circular hole centered on the edge

facing the beam center as seen in figure 14. The signals from these elements were processed in the same manner as the beam counters. The counters with an E (W) were mounted on the east (west) side of the beamline and those with a 1 (2) were mounted 34.5 cm downstream of the downstream end of the target (on the downstream mirror plate of the analysis magnet).

The online definition of an interaction used in the data acquisition was kept as the logical OR of the four interaction counters. However, a detailed study of the interaction counters indicated that an interaction definition with at least two or more interaction counters being struck would provide the most efficient trigger for offline analysis.[17]

The discriminated signals from the veto walls as well as the beam and interaction counters were recorded in latches whenever an event trigger occurred. These latches were toggled by the beam and had 15 time ticks[#8] read out after each trigger. The 7th (8th) time tick in the latches corresponded to the beam & veto wall (interaction) elements in time with the trigger. This time structure information allowed us to remove out of time and halo particles from the data.

§ II.7. Secondary Targets

Downstream of the veto wall was placed a target stage with 5 separate target stacks. These targets were remotely maneuverable so that data taking was not interrupted when the target stack was changed. The characteristics of the targets are summarized in the table below.

#8 I.e. 1 time tick ≡ 1 RF beam bucket.

Table 2 **Table of nuclear targets used in E706 during 1987 → 1988**

Target	λ_{int}	$\#_{scatterers}$ ($x\frac{10^{23}}{cm^2}$)	# Layers	$\frac{\Delta Z}{Layer}$(mm)	$\frac{Gap}{Layer}$(mm)
Aluminium	2.4%	17.0	6	1.6	1.6
Beryllium	9.8%	45.7	20	2.0	1.6
Carbon	10.5%	55.6	20	2.0	1.6
Copper	4.2%	35.8	8	0.8	1.6
Copper+Beryllium	10.9%	54.3	2+20	0.8+2.0	1.6+1.6
Empty (i.e. Silicon)	0.5%	3.1	8	0.28	NA

§ II.8. The Silicon Microstrip Vertex Detector

Points along the trajectories of incident and secondary charged particles were determined with very high resolution by a Silicon micro-Strip vertex Detector SSD shown in figure 15. This system was capable of resolving tracks within $\Delta x = \Delta y = 30$ μm (and $\Delta z = 600$ μm). 6 planes were located immediately upstream of the target and 8 planes were located immediately downstream. The planes were grouped into 7 modules of 2 planes each and the planes within each module were oriented perpendicular to each other and to the beam axis. The 2 most downstream modules were created from silicon wafers with an active area of 5 x 5 cm^2 and contained 600 readout strips per plane while the remaining 5 modules were made from wafers with an active area of 3 x 3 cm^2 and contained 1000 readout strips per plane.

Each plane was formed from a wafer of silicon 250 → 300μm thick. A minimum ionizing particle traversing one of these planes would release 2.0 → 2.5 x 10^4

electron-hole pairs. The charge was collected in $\approx$ 20 nanoseconds by a low-noise, wide band, charge sensitive preamplifier designed at Brookhaven National Laboratories *(Rel-Lab 10-323-C)* . The preamplified signal was then further amplified *(Nanometric* wide band video amplifier N-277C), then discriminated (threshold discriminator) and converted into a logic signal and stored as binary data (ECL line driver to *Nanometric* N-278 latch). The SSD's retained information for 100 nanoseconds and the trigger was synchronized with the data acquisition system so as to fall directly in the center of this interval. The SSD's were found to degrade with exposure to the beam as manifested in a 4 fold increase in the noise current levels over the course of the run.[18] Since noise in the SSD's simply adds a few fake hits to an otherwise clearly defined charged track signal this process did not obscure genuine tracks. Consequently the radiation damage had negligible effect on the overall efficiencies of the vertex reconstruction algorithms.

The segmentation of the target is clearly evident in figure 16 which shows the vertex position (reconstructed using the SSD information) as a function of Z (the beam axis). Peaks are clearly evident at the locations of the modules of the SSD detector itself.

§ II.9. The Proportional Wire Chambers

The third detector system along the MW9 beamline was located immediately downstream of the analysis magnet and consisted of 4 Proportional Wire (drift) Chamber PWC modules. Within each module were readout planes with an X, Y, U($+37^o$) and V(-53^o) orientation of the sense wires. The sense wires were 20μm gold plated tungsten with a wire spacing of 0.1". The size of each module

increased with its distance from the target as can be seen from the table below. A .001" thick mylar sheet painted with a segmented graphite mask was used as the cathode. The segmentation of the graphite mask allowed the voltage on the outer regions of the detector (away from the beam) to be decoupled from the voltages on the two inner regions where the density of tracks was very high. By this means the center regions of the PWC's were operated at a much lower voltage than the outer regions in order to avoid saturation and slewing in this part of the detector. The innermost region directly surrounding the beam had no voltage applied to it, with the voltage being allowed to float freely. The total area contained within each of the three voltage regions (high voltage HV, low voltage LV and no voltage NV)[#9] along with a few other interesting parameters are tabulated below.

Table 3 **Table of Proportional Wire Chamber Parameters**

Module #	Z (cm)	# Channels	HV (in^2)	LV (in^2)	NV (in^2)
I	350	2496	162.6 x 121.9	15.2 x 15.2	2.5 x 2.5
IIA	455	3392	203.2 x 203.2	20.3 x 20.3	3.8 x 3.8
IIB	563	3392	203.2 x 203.2	20.3 x 20.3	3.8 x 3.8
III	670	4160	243.8 x 243.8	30.5 x 30.5	5.1 x 5.1

The efficiency of these chambers was measured to be $\approx$ 95% during the bulk of the data taking.

The data acquisition system for the PWC's was identical to that of the SSD's

#9 The inner two regions are referred to as the "diffractive" and "beam" regions respectively.

in most respects. The charge collected from the sense wires was fed through preamplifiers mounted directly on the frame of the modules. The signal then was sent via an ECL line driver to a second amplifier and then to a discriminator. The discriminated data were sent to a constellation of *Nanometric* latches where it was held pending a trigger decision. The information from the PWC's were accessible for a period of 100 nanoseconds and the data acquisition system was synchronized so that the trigger occurred 30 ± 10 nanoseconds into this interval.

Monte carlo calculations and studies of electron candidates indicated that the momentum resolution $\frac{\Delta p}{p} \approx 0.1\%$ for the PWC+SSD system. The angular resolution for tracks linking through the magnet was $\delta\theta = 0.1$ mR, implying a pseudorapidity resolution which is described by $\delta\eta = \frac{\delta\theta}{\sin(\theta)} = \frac{0.1}{\sin(\theta)}$. A study of the interior angle formed by 2 tracks as a function of the number of shared hits indicates that two tracks within 1.5 milliradians of each other could be resolved by the PWC's. This minimum interior angle increases from $1.5 \rightarrow 2.5$ milliradians as the angle between the beam line and the pair of tracks increases from $0 \rightarrow 40$ milliradians.

§ II.10. The Liquid Argon Calorimeters

At the center of the experiment was the world's largest Liquid Argon Calorimeter[19] (LAC) which consisted of 2 detectors and $\approx$ 50,000 liters of liquid argon[#10] in a large dewar shown in figure 17. The dewar vessel was formed from rolled stainless steel plates $\frac{9}{16}$" thick and had an internal diameter of 5.2 meters. The LAC electronics were mounted on the top of the dewar and enclosed within a

#10 This represented $\frac{1}{3}$ of the world supply of liquid argon at the time of the experiment.

room shielded from radio signals. A very low density cryogenic insulation covered the exterior of the LAC to minimize heat exchanges with its environment.

Liquid argon has two notable features which make it a desirable active medium for calorimetry. As a member of the noble gases it is inert and does not interact with other material under normal circumstances. Also, it has a very high electron mobility allowing for swift signal collection.

The upstream surface of the LAC dewar had a 2" diameter beam port with $\frac{1}{8}$" thick aluminum windows in order to reduce the amount of material in the beam. In addition, two low density argon excluder vessels were installed inside the dewar to further reduce the amount of material in front of the calorimeters. The first covered the entire upstream hemisphere and was composed of an epoxy coated, low density, cryogenic, closed cell foam (Rohacell^{TM}) encased in $\frac{1}{16}$" thick stainless steel skin. The second vessel was a truncated conical shell 172.5" in length tapering from a radius of $12\frac{9}{16}$" downstream to $17\frac{7}{16}$" upstream with a skin of $\frac{1}{16}$" stainless steel. This was inserted along the beam axis and excluded liquid argon from that region. The beam filler vessel was pressurized with gaseous helium.

§§The Photon/Electromagnetic Calorimeter

The most crucial detector for E706 was a lead-liquid argon ionization calorimeter[20] consisting of alternating layers of lead, argon and copper clad readout boards. This calorimeter was located 9 meters downstream of the secondary target and was optimized for the detection of photons coming from the target and therefore was named the ElectroMagnetic CALorimeter EMCAL. The EMCAL

had an annular geometry extending 145 cm outward from a radius 21.1 cm from the beam axis. This detector completely covered the rapidity range from -1 to +1 in the center of mass at 530 GeV. The detector was assembled in 4 physically independent quadrants and further subdivided (by readout boards) into 2 octants within each quadrant as can be seen in figure 18. All readout channels were focused on a point roughly in the center of the secondary target stack in order to easily generate a prompt P_T trigger. This also allowed for some discrimination between particles originating near the vertex and those from other sources (e.g. halo muons).

There were 33 active cells in the EMCAL each of which had a pair of subcells: one with a readout plane in R and the other with a readout plane in ϕ. Each subcell consisted of a 2 mm layer of lead followed by a 2.5 mm liquid argon gap and a 1.6 mm layer of double sided copper clad G-10 (fiberglass) etched with identical readout strip patterns on both sides. High voltage was applied to the lead sheet which served as the cathode and the charge collected in each readout strip was extracted with a system based upon the MX and RABBIT[21] data acquisition systems. The first 11 (upstream) cells were ganged together and read out as a single FRONT section as were the final 22 (downstream) cells in the BACK section. The front section contained $\approx$ 8 radiation lengths of material while the back section contained $\approx$ 16 radiation lengths. Other material between the EMCAL and the target represented $\approx$ 2 radiation lengths.

Very fine segmentation of the readout pads was introduced in order to spatially resolve both photons from the decay $\pi^0 \rightarrow \gamma\gamma$ which constitutes the primary source of background to the direct photon signal. At very high energies the 2

photons from a pizero decay are separated by a distance $x = L\Theta = L\frac{2m_\pi}{E}$, where L = distance from the π^0 decay. At a distance 9 meters from the target this gives a separation of 2.4 cm for a 100 GeV π^0.

There were 252 (238) radial (R) strips in the front (back) readout section, each covering 0.5 mR in the polar angle Θ The azimuthal (ϕ) strips were further divided into inner and outer readout sections. ϕ channels in the inner section each covered an angle of $\delta\phi = \frac{\pi}{192}$ radians and extended from the edge of the beam hole (R = 23 cm) to a radius of 40 cm where the outer readout section began. The outer readout in ϕ extended radially from 40 cm to 160 cm (the outer radius of the detector) with readout channels which covered an angle of $\delta\phi = \frac{\pi}{384}$ radians. There were 48 (96) inner (outer) ϕ strips per octant in both the front and back readout sections.

There were 3936 channels in R[#11] and 2304 channels in ϕ for a total of 6240 channels in the entire EMCAL detector all of which could be read out on any particular event. In order to reduce the dead time in the data acquisition process and to compress the size of the data structure, all channels with collected charge corresponding to an energy deposition of less than $\approx$ 150 MeV were suppressed. This reduced the mean number of strips readout to $\approx$ 500 channels under our standard trigger.

Dedicated tests with beams of electrons indicated that this detector had a resolution of $\frac{\sigma_E}{\text{Energy}} = \frac{14\%}{\sqrt{\text{Energy}}}$ for electromagnetic showers. A separate study of charged tracks reconstructed by the planes indicated the EMCAL was capable

#11 This number includes the irregular "flash" strips located on the outermost and innermost edges of the readout boards.

of reconstructing the position of these showers to within a few millimeters of the SSD+PWC system's projection of the track dependent upon the angle.

§§The Hadron Calorimeter

The second detector in the LAC was a 181 ton liquid argon hadron calorimeter HALAC. The upstream face of the HALAC was located 9.72 m downstream from the secondary target and it had a depth of 2.5 meters.[22] The hadron calorimeter also employed the liquid argon as an active material and employed 52 layers of stainless steel as an absorber. The absorber plates were 2.5 cm thick, had an outer diameter of 3.8 meters and a inter-plate argon gap of 2.4 cm. The readout channels in the HALAC were focused on the secondary target in the same fashion as in the EMCAL.

A circular beam hole was located in the center of each of the octagonal absorber plates and had a diameter which increased with the distance from the target and which was intended to match the acceptance of the readout planes. Unfortunately this tapered beam hole was inadvertently manufactured slightly undersized with an upstream diameter of 43.58 cm and a downstream diameter of 46.43 cm which was approximately 4 cm smaller than the readout boards.[#12] The dead region between the edge of the beam hole and the edge of the readout boards covered the region from $\theta = 19.0$ to 22.4 mR relative to the beam axis.

The readout system for the HALAC consisted of 53 octagonal planes with hexagonal beam holes divided into two sections: a front section of 14 planes reading out 2 interaction lengths of material and a back section with 39 planes

#12 This reduced the geometrical acceptance of the forward calorimeter to a radius of 31.6 cm.

reading out 6 interaction lengths of material. The beam hole in the readout planes had an upstream diameter of 43.2 cm and a downstream diameter of 54.7 cm. Each readout plane consisted of a laminate of four layers of copper clad G-10 (fiberglass) and unclad G-10 spacers. The two outermost layers in each readout plane served as the high voltage cathode planes while the two inner layers were the anode planes from which the signals were extracted. The anode planes were etched with a tessellated pattern of equilateral triangles as shown in figure 19 and presented a focused tower structure to the secondary target. The sizes of the triangular readout pads increased from a height of 10.8 cm on the upstream end to a height of 13.7 cm on the downstream end, and were closely matched the mean width of a typical hadronic shower.

The resolution of the HCCAL was measured to be $\frac{\Delta Energy}{Energy} = \frac{120\%}{\sqrt{Energy}}$ and covered the rapidity interval from -1 to +1 in center of momentum frame. An effective threshold of 5 GeV was introduced to compensate for relatively high noise levels which were encountered below that point.

The final detector in this experiment was located just downstream of the LAC and represents a major source of effort for this dissertation. Consequently it will be described in a separate chapter which follows.

REFERENCES

[16.] I.Kourbanis, PhD. Thesis, Northeastern University, (1989) unpublished.

[17.] R. Benson, E706 note # 174.

[18.] E. Engels et al, Nuclear Instrumentation & Methods A279 (1989) 272.

[19.] B. DeSoi, PhD. Thesis, University of Rochester, (1989) unpublished.

[20.] Ibid.

[21.] D. Skow, PhD. Thesis, University of Rochester, (1989) unpublished.

[22.] C. Lirakis and A. Sinanidis, PhD. Theses, Northeastern University, (1989) unpublished.

CHAPTER III. THE FORWARD CALORIMETER

The final detector in E706 covered the most forward region relative to the beam and was designed to measure the momentum of the collision products within the rapidity interval from +1.1 to +3.5 as measured in the center of momentum frame. This corresponds to an angular coverage from 0.1 mR to 33 mR although the shadow from the LAC reduced this outer edge to only 19 mR. It was composed of 90 alternating layers of $\frac{3}{4}$" iron and $\frac{3}{16}$" scintillator arranged in three separate modules and stacked perpendicular to the beam as shown in figure 20. The construction and operation of the Forward CALorimeter (FCAL) formed the basis for the work described in this dissertation and so will be described in detail.

This chapter is divided into 6 sections which describe the forward calorimeter from a number of vantage points. The first section (*Design Considerations*) provides an explanation of the design considerations for this detector. The next 3 sections (*Construction, Electronics, Light Collection*) describe the hardware and some of the peculiar features associated with it. The last 2 sections (*Data Reconstruction, Calibration*) describe the algorithms used to convert the raw data into meaningful kinematical quantities. Data analysis and comparisons to other experiments are presented in the next chapter.

§ III.1. Design Considerations

The forward calorimeter was designed as a total absorption calorimeter. It was optimized for the measurement of the total energy and mean P_T of very high energy showers due to particles produced close to the beamline. All hadrons

which struck this detector were to be completely absorbed in iron with the resulting cascades producing scintillation light in layers of acrylic scintillator. The scintillation light was absorbed in light guides doped with a wavelength shifting chemical. This chemical (BBQ) captured the blue light of the scintillator and converted it into green light which was transported along the light pipes to photomultiplier tubes placed outside the detector. Each of these steps will be discussed below in addition to the reasoning behind the particular choices of detector dimensions.

§§Shower Containment

Length

The length of the calorimeter was determined by considerations of the amount of leakage energy out the end. The absorption of hadronic showers is characterized by the nuclear collision length λ_I. In iron, $\lambda_I = 17.4$ cm. Absorption of electromagnetic showers is characterized by the radiation length λ_{rad} which is 1.82 cm in iron. Figure 21 shows the amount of material required to contain 95% (98%) of the energy of a shower due to an incident hadron (electron or photon).[23] From this it is clear that 10 $\lambda_I = 172$ cm of iron is adequate to contain showers up to the primary beam's energy of 800 GeV.

Diameter

The diameter of the calorimeter was determined by the diameter of the beam hole in the LAC and by the transverse spread of hadronic showers. For geometrical containment the rear of the calorimeter had to be $\approx$ 60 cm in diameter. The transverse width of hadronic showers is independent of energy in the range

between 20 and 700 GeV[24]. In the following table is shown the fraction of energy outside a plane a distance x from the center of a shower.

Table 4 **Transverse Leakage in Hadronic Showers**

x (cm)	Leakage (%)
10	7
15	4.5
20	3
25	2

The FCAL was fabricated with an additional 23 cm of material beyond that of its geometrical acceptance so that less than 2% of the total energy would be expected to leak out the sides. This provided sufficient containment with negligible effect on the expected resolution of the device.

§§Sampling Rates

In the forward direction of a high energy interaction, there are likely to be several high energy particles in close proximity, with the result that both electromagnetic and hadronic showers overlap in the FCAL. We decided to optimize the detector for the hadronic component of these showers and to make adjustments to the reconstruction algorithms to account for the effects of the electromagnetic components. For design and construction purposes this decision simplified the geometry by making the detector longitudinally symmetric.

No general formula can be given to describe the dependence of a sampling calorimeter on material, energy and sampling thickness x_p and one must resort to a monte carlo and previous measurements to arrive at some reasonable estimate. The overall resolution of a calorimeter depends upon the frequency with which the shower is sampled. To a certain point, the more frequently the shower is sampled the better the resolution. However, at some point statistical fluctuations in the number of charged particles crossing the sensitive material will limit the usefulness of reducing the sampling frequency. Figure 22 shows some published results of energy resolutions versus energy for a number of calorimeters with a variety of sampling frequencies.[25] Several groups have found[26] that the resolution

$$\left(\frac{\sigma(\mathrm{E})}{\mathrm{E}}\right)^2 \approx \left(\frac{50\%}{\sqrt{E(GeV)}}\right)^2 + \left(40\%\sqrt{\frac{4x_p}{\lambda_{\mathrm{rad}}\mathrm{E(GeV)}}}\right)^2 \qquad \text{(III.1)}$$

where the first term arises from shower fluctuations and the second term can be attributed to sampling fluctuations. Sampling sizes smaller than $x_p \approx \lambda_{\mathrm{rad}}$ cease to improve the resolution as the first term on the right hand side of equation III.1 then dominates. This is approximately the sampling frequency which we choose.

A monte-carlo program was used to optimize the transverse dimensions of the FCAL light collection system such that the resolution in the observed total energy and P_{T} distributions are independent of the geometrical factors involved in light collection. Firstly, the separation between the readout channels was determined. This depended primarily on the shower width. As can be seen from figure 23 the average transverse shower size of hadronic showers is $\approx$ 4 - 5 inches. The monte-carlo program showed that sampling the scintillation light at a spacing of greater than 4.5 inches caused the observed energy distribution to become

dependent on the particle interaction point. At a smaller spacing the resolution was independent of the separation.

§ III.2. Construction

The FCAL consisted of three cylindrical modules containing alternating layers of $\frac{3}{4}$" iron and $\frac{3}{16}$" acrylic scintillator as shown in figure 24. Each of these modules was 30" long and had a diameter of 45". A $1\frac{1}{4}$" diameter beam hole was drilled along the longitudinal axis of the calorimeter along with 76 clearance holes of diameter $\frac{7}{16}$" for the wavelength shifting light pipes as can be seen in figure 25. The spacing of these holes was 4.5 inches. All of these clearance holes in the scintillator were smooth cut and unpolished as were the outer rims of the scintillator plates. A coating of reflective white paint *(Nuclear Enterprises NE560)* was applied to both the outer rim and the beam hole of the scintillator in order to minimize light losses. The upstream and midstream modules contained twenty-eight layers of iron and twenty-nine layers of scintillator while the downstream module contained thirty-two layers of iron and thirty-three layers of scintillator for a total of 10.5 interaction lengths of material.

The scintillator was a standard type called *Plexipop* consisting of 10% naphthalene, 1% POPOP and 0.01 % PPO in acrylic. The use of acrylic made machining simple and inexpensive. This scintillator radiates 98% of its light in the range between 380 and 530 nanometers as can be seen in figure 26. The scintillation light was collected in a regular square array of wavelength shifting light pipes and conducted downstream to a photomultiplier tube *(Hamamatsu*

#R1666). The light pipes were doped with 90 *mg/l* of BBQ[#13] to capture the scintillation light. The end opposite the PMT was coated with a layer of silver backed by the reflective paint. The silver reflected up to 95% of the incident light and noticeably improved the light transportation efficiency of the BBQ rods.

Each BBQ rod was attached to a PMT with a silicone optical coupler *(National Diagnostics ND-711)* which has a transmission of 99% in the relevant optical band. In both the upstream and midstream module these BBQ+PMT assemblies were configured so that 34 channels were read out on the upstream end of the BBQ rod and the remaining 42 channels were read out on the downstream end. The downstream module was read out entirely on the downstream end. Although these alternate readout directions were introduced in order to partially compensate for attenuation effects in the BBQ rods it also gave some measure of the longitudinal development of the energy deposition in the two most upstream modules. The alternating readout scheme would have had little effect in the downstream module since it typically received less than 5% of the total hadronic energy and so it was left with a single readout plane.

In order to perform calibration and analysis tasks and to monitor the possible effects of radiation damage[27] a calibration system based upon an ultraviolet laser was installed. This is shown in figure 27. It consisted of a pulsed ultraviolet nitrogen laser directed upon a number of optical elements before finally falling onto the input coupler of a quartz fiber optical bundle. A fraction of the beam was split off and directed onto a high-speed linear photodiode *(EG&G* FND 100) which provided a trigger signal for the calibration data. The quartz fiber

#13 A wavelength shifter

optical bundle was divided by a septum at the input coupler into 2 bundles of 225 fibers each, and each of those bundles was further subdivided into 3 bundles of 75 fibers. The individual fibers within a given bundle were directed onto the extreme upstream and downstream scintillator plates within a module and centered in the plaquettes formed with a BBQ rod at each corner. This can be seen in figure 28. This allowed us to selectively inject ultraviolet light into either the upstream and/or the downstream end of the modules. It was used extensively for setting the gains of the tubes initially and performing diagnostic tests as described below.

§ III.3. Electronics

The voltages to the dynodes of the photomultiplier tubes were supplied with the circuit shown in figure 29. Power transistors on the final three dynode stages stabilized the voltage levels against sagging under high pulse rates. The high voltages to the PMT's were supplied by a *LeCroy 1440* high voltage system with the initial settings for each tube determined via software which drew upon the nominal tube characteristics according to data sheets supplied by the manufacturer. Finer adjustments to individual tubes were made after studying the response of each tube to a standard pulse of light delivered by the laser calibration system described previously. After collecting data from $\approx$ 100 laser pulses the high voltages to the PMT's were adjusted so as to equalize the response from all channels. The dynamic response of this system was measured as a function of the amplitude and rate of the incident pulses (see figure 30) with a characteristic cutoff current occurring around 0.3 mA yielding very stable responses for large

pulses up into the megahertz range.

The PMT pulses were taken directly from the anode into fast operational amplifiers (*NE5529*) configured with a net gain of 30 as shown in figure 31. Each of the 228 amplifier bases were individually adjusted so that there was $\approx$ 40 mV DC level on the output line when the input was held at ground. Fitting the rising edge of a pulse from the amplifier to an exponential of the form $exp(\frac{t}{\lambda})$ yields λ = 4.7 nanoseconds as in figure 32. This is a measure of the amplifier risetime. A fit to the falling edge of a standard pulse yields a value of λ = 15.8 nS and is a measure of the decay time of the BBQ fluorescence in the wavelength shifter rods.

§§Readout Electronics

The analog signals from the PMT amplifier bases were sent over a pair of identical coaxial cables (RG 58) of 100' length. One of the pair was used for generating a fast $P_{\text{transverse}}$, $E_{\text{transverse}}$ and E_{total} signal with modules in a NIM environment while the other was fed into a 6 bit Flash Analog to Digital Converter (FADC) system housed in a CAMAC environment. The former signal path was designed primarily for use as a veto on multiply occupied beam buckets. However, it was not included in our trigger during the 1987 $\rightarrow$ 88 run.

The FADC was a *Siemens* 5200 integrated circuit which digitized the analog pulse once every 11.2 nS[#14] and passed the digitized data into a wrap-around

#14 Adjacent beam buckets were spaced 18.8 nS apart however the clock which strobed the FCAL was not directly synchronized with the RF tune of the accelerator nor were adjacent FCAL channels synchronized with each other to better than $\pm$ 3 time ticks. Consequently all events with an occupied bucket within $\pm$ 2 RF beam buckets of the trigger ($\approx$ 25% of the data under high intensity running conditions) were inseparable as far the FCAL data was concerned.

memory *(Hitachi 10422)* which was used as a buffer.[#15] A trigger decision would stop the clock which toggled the FADC's and their associated buffers, thereby freezing the information from the previous 2.87 μS (256 time ticks) in the buffers.

The Data Acquisition (DA) procedure consisted of determining the address of the pointers at the time of the trigger and subtracting the trigger delay of 80 time ticks from that address and then moving the pointers to the resultant address of the buffers. At that point a serial read (DMA) would transfer 15 data words from the buffer into a PDP 11/34 computer which acted as the front end of our DA system. After the data had been transferred to the PDP the final buffer addresses were read out to ensure that the buffers had been incremented properly. Finally, the clock was restarted thereby allowing data taking to continue.

§ III.4. **Light Collection**

Scintillation light was created by charged particles passing through scintillation sheets and was absorbed in wavelength shifting light pipes referred to as BBQ rods. These BBQ rods transport the wavelength shifted light from the interior of the detector out to the ends of the detector where it is observed by photomultiplier tubes.

The attenuation properties of a typical BBQ rod is shown in figure 33. The two component character of the attenuation curve can be understood in terms of the geometrical characteristics of the rod combined with the absorbtion characteristics of the rod material. If all of the scintillation light were absorbed precisely

#15 The FADC is described in detail in P. Lukens, E706 note # 173.

on the axis of the BBQ rod the critical angle Θ_c for the wavelength shifted light to be totally internally reflected would be completely independent of the azimuthal angle Φ and would only depend upon the polar angle Θ of emission (see figure 34) and the indices of refraction in air and in acrylic $n_{\rm air}, n_{\rm acrylic}$. I.e.

$$\Theta_c = \arccos(\frac{n_{\rm acrylic}}{n_{\rm air}}) + \frac{\pi}{2} \qquad \text{(III.2)}$$

However, once light is absorbed and reemitted (isotropically) off the axis of the rod the critical angle(s) becomes dependent on the absorption/emission point and both the azimuthal and polar angles.

The source of the very short range ($\lambda = 10$ in) component to the attenuation curve can be attributed to light which follows a wide spiraling path through the BBQ and which is therefore attenuated in a very short distance along the longitudinal axis. The long range ($\lambda = 25$ in) component is simply the attenuation length due to the light traveling along paths which are closer to parallel with the longitudinal axis of the rod.

The effect of these transport properties in the FCAL was to make the total light collected dependent on the depth of the shower maximum. This is most evident when the shower maximum occurs near one of the ends of the detector. This non-linearity was reduced by leaving an $\approx$ 3" gap between the PMT and the nearest layer of scintillator and also by reading out the light created in the scintillators at both ends of the modules, as described below. However, this characteristic of the FCAL was a noticeable feature of our data from the 1987 $\rightarrow$ 88 run and steps to reduce this effect for future runs are currently being implemented.

§ III.5. Data Reconstruction

The FADC technique of encoding the signals from the detector allowed for several sources of error as well as several unique means of error correction. For example the discreteness of our sampling meant that an interpolation was necessary in order to determine the signal integral. A typical pulse is shown in figure 35.

Differences in time between the start of a pulse and the digitization times resulted in an $\approx 2\%$ fluctuation in the integral of the signal from the FADC. Another potential problem results from noise in the readout system[#16] which occasionally produced a single "spike" in the signal which, if it were integrated over, could produce an error comparable in magnitude to the underlying signal. An example of this is shown in figure 36. In this situation there is an obvious advantage to the FADC system since these events were easily identified and corrected (by replacing the spike with the average of adjacent channels). These digitization errors were negligible.

The (non-zero) pedestal was defined on a channel by channel basis as the FADC value immediately preceding the start of a pulse. This pedestal value was subtracted from the signal within the integration window. Occasionally, hysteresis would result in an FADC value which fell below this pedestal; the integration was stopped at that point.

Other notable features of the digitized pulses include the shape and length of

#16 E.g. A particle striking one of the dynodes and thereby initiating an electron cascade in a PMT could produce such a signal or (more likely) a failure of the memory chip to register the data from the ADC properly

the tails periodically associated with the pulse. It was found that the inclusion of data beyond 56 nS of the beginning of a pulse (5 time ticks) served only to introduce an overall offset in the total reconstructed charge. This was due to the apparently random distribution of hysteresis in the FADC's which tended to produce very long tails on some pulses. It was observed that the settling time for some channels to return to the pedestal value could occasionally be on the order of 1 μS. For large pulses the contribution from that mechanism was entirely negligible. However, for some of the smaller pulses it could be the dominant effect: in the most extreme cases, the pulses were reduced to a step discontinuity as shown in figure 37. Figure 38 shows that the contribution from the "step-like" pulses is less than 10% with 50 GeV deposited in the FCAL and was typically on the order of 3% in the range above 100 GeV where most of the data falls. These errors are far below our experimental resolution.

Figure 39 shows the sum of the signals from the eight PMT's with the largest signals. They account for more than half of the total signal over the entire range of energies.

§ III.6. Calibration

The calibration of the FCAL proceeded through several stages. First the gain factors for each of the PMTs were adjusted to produce a uniform response from the detector without any residual sensitivity to the position of the incident particles. Further corrections to the raw (uncalibrated) data were made to compensate for time dependent effects due to numerous sources. After that, we created a monte carlo computer program and adjusted its internal parame-

ters so that it accurately simulated the response from the FCAL. The scale for the program was adjusted to match the raw (single particle) calibration data precisely. A calibration curve was then extracted from the monte carlo by comparing the simulated response of the FCAL to the known incident energy of a set of events simulating a minimum bias trigger. Each of these intermediate steps are described in the subsections which follow.

§§PMT Gains

Calibration data were taken at 18 distinct positions along the midline of the detector using a negative beam of 530 Gev pions (98%) and kaons (2%). These data were obtained by scanning the beam across the midline of the detector. Due to the aperture formed by the LAC beam hole[#17] the calibration beam could not be swept along the vertical plane nor could it be moved from side to side by more than a couple of centimeters. Therefore the detector itself was driven across the beam using a remotely controlled DC motor connected to a drive screw monitored by a shaft encoder. The shaft encoder generated $1\frac{count}{mm}$. Consequently the position of the detector was known very precisely.

The common technique of determining calibration factors C_i is to minimize χ^2 with respect to the $C_i's$ where χ^2 is defined as

$$\chi^2 = \sum_{Events} (E_{\text{predicted}} - \sum_{channels} C_i * E_i)^2 \qquad \text{(III.3)}$$

and where

#17 It might be noted that a scan of the beam window in the dewar obtained by moving the LAC gantry through the beam coupled with measurements of mean reconstructed positions on the calorimeters indicated that the beam might have been as much as 1 cm off center relative to the LAC beam window.

C_i = correction factor for the i^{th} channel

E_i = reconstructed signal from the i^{th} channel.

This technique requires all channels being used in the fit to have approximately the same mean contribution to the second term on the right hand side and would therefore require roughly uniform exposure of the detector to the test beam.

Since the LAC aperture precluded a vertical sweep of the calibration beam this technique could not be exploited. Instead, we chose to fit the mean response of each PMT as function of the separation between its BBQ rod and the test beam. This procedure ascribes a correction factor to every readout channel and attempts to minimize the effects of the beam position on the sum of the reconstructed signals.

Before calibration, we observed a strong correlation between the position of the calibration beam and the raw, uncalibrated reconstructed signal from the forward calorimeter as shown in figure 40. Much of this variation can be attributed to residual channel to channel variations not properly accounted for in the nominal PMT conversion factors which convert the integral of the FADC signal to an equivalent light output.

Several characteristic features of data from single channels are illustrated in figure 41 which shows the mean raw signal from a single PMT channel plotted as a function of the position of the beam. The most significant features are:

- Dip in the reconstructed signal near the point of closest approach
- Dip in the reconstructed signal near the beam hole
- Data on the far side of the beam hole systematically lower than data on

the near side

- Rise in the reconstructed signal near the edge of the detector

All these effects arise from either shadowing of the BBQ rod (by either another BBQ rod or the beam hole) or from reflections near the edges.

Numerous requirements were placed on the data in order to account for these and other effects. These requirements are collected in the table below.

Table 5 **Requirements imposed on data used to determine gains**

The data (in arbitrary units) were averaged over entire runs
Channel Total Signal > 2
Readout Section Total Signal > 80
Module Total Signal > 100
Data > 2 cm from the X projection of the BBQ
Data < 15 cm from the X projection of the BBQ
Data > 2 cm from the X projection of the beam hole
Data on the far side of the beam hole were excluded for the channels along the midline
$\frac{Data}{Error} \geq 1.9$ for each channel

Data passing all cuts were used to fit the parameter A_{ch} in the following formula :

$$\langle Data(position) \rangle * R(position) = A_{ch} * e^{\frac{-R(position)}{R_0}} \qquad \text{(III.4)}$$

where R = separation between the test beam and the light pipe for a given

position of the modules

$$R = \sqrt{ybbq^2 + (xbbq - x_0)^2} \qquad \text{(III.5)}$$

$xbbq, ybbq$ = Module coordinates of channel position

R_0 = constant = 35.0 cm

x_0 = Shaft encoder position - 68.6 cm (coordinate transform)

Both x_0 and R_0 were determined by minimizing the value of the χ^2 for channels along the midline in the upstream module. All but the four outermost channels along the midline of the upstream module were used in determining these constants. In general, the quality of the fits was found to vary quite slowly with respect to the values of these parameters and an estimate of their uncertainty is $\pm$ 5 cm for R_0 and $\pm$ 1 cm for the offset. These parameters were fixed at their nominal values to allow comparison of the fit amplitudes between channels. Each of the 228 channels was fit separately.

Channels having no data passing the cuts or which failed the fit were assigned a correction factor of 1 (i.e. their gains were left unchanged). These channels were generally located near the edge of the FCAL and signals from such tubes had a negligible effect on the total signal. The remainder of the channels were assigned a correction factor C_i determined on a readout section by readout section basis. Note that there are 5 distinct readout sections: upstream & downstream readout of modules 1 & 2 and only a downstream readout of module 3. The normalization for each readout section $\langle A \rangle_{Section}$ was determined using only those

channels which were successfully fit by the fitting routine. The prescription for these correction factors follows

$$C_i = \frac{\langle A \rangle_{Section}}{A_i} = \text{ Gains Correction Factor} \qquad \text{(III.6)}$$

where

$$\langle A \rangle_{Section} = \frac{\sum_{Section} \frac{A_i}{\sigma^2_{A_i}}}{\sum_{Section} \frac{1}{\sigma^2_{A_i}}} = \text{ Normalization Factor} \qquad \text{(III.7)}$$

The results of taking the raw data used in figure 40 and applying these correction factors are demonstrated in figure 42. Clearly this procedure has significantly reduced the sensitivity of the total reconstructed signal with respect to the shower's center.

§§Removal of Long Term Drifts

At this point there remained one more correction which had to be applied to the raw data in order to obtain a stable and reliable response. The position of the beam itself would wander relative to the location of the FCAL beam hole, resulting in drift of the average shower center as can be seen in figure 43. Since this drift is not compensated by any adjustments to the detector or its readout system during the data taking we monitored the mean reconstructed position of the shower center of the interaction triggers and adjusted the nominal position of the detector so as to keep this quantity fixed relative to our known calibration points. Typically these corrections were on the order of 10% of the reconstructed signal.

§§Determination of the Calibration Curve

Having optimized the relative response of each channel in the detector let us turn now to the overall correlation of the reconstructed signal with the incident energy.

General Considerations

One basic difficulty present in this detector is the fact that the detector response is nonlinear. The primary reason for this nonlinearity is the fact that there is a finite threshold associated with each PMT channel below which the channel will not register any signal whatsoever. This is due to the finite bit size of the flash ADC's. The effective threshold value varies from channel to channel, with typical values corresponding to a light level equivalent to 2 GeV in the reconstructed signal. At high energies these thresholds are very small in comparison with the magnitude of the total signal. However, at lower total energies, they become an important factor with the consequence that the normalization factor between raw signal and reconstructed energy is energy dependent.

One must also grapple with the fact that a shower in the forward calorimeter is composed of a number of particles with different energies distributed over the face of the detector, each interacting and depositing their energy over a variety of depths in the detector. This means that the detector may respond differently to multiparticle showers than it will to single particle showers. From the foregoing discussion on the thresholds we see that this must be the case at some level since multiparticle showers are less localized than single particle showers and may have more (or less) PMT channels above their thresholds. Furthermore, the longitudinal development of electromagnetic showers differs significantly from

that of hadronic showers. Electromagnetic showers were primarily due to photons resulting from pizero decays and deposited their energy in the FCAL quite promptly in an electromagnetic cascade which was entirely absorbed in the first few layers of iron of the FCAL, even for very high energy showers. Hadrons shower very deeply, and would typically deposit 10 to 30% of their energy in the midstream and downstream modules. Hence the convolution of the particle type and multiplicity distributions with the absorption and attenuation properties of the calorimeter material was essential to a genuine understanding of the correlation between the raw reconstructed signal and the most probable value of the incident energy. These are precisely the tasks to which a monte carlo program is ideally suited. We chose to generate the calibration curve by means of a monte carlo program which was tuned to reproduce the observed behavior of the single particle calibration data and which then used multiparticle events to simulate the conditions under which that actual experimental data were obtained.

Initial Monte Carlo Adjustments

Before any monte carlo simulation was attempted the transmission properties of the BBQ rods and scintillator sheets along with all the geometrical information about the FCAL were encoded into the monte carlo program. However, there remained an overall uncertainty in the scale of the output simply due to the residual uncertainties in the true gain factors under our operating conditions. Consequently, the scale for the monte carlo was first tied to that of the calibration data. This was done by generating a set of over 500 events simulating the 530 GeV calibration beam and then comparing the monte carlo predictions to the real data. The particles in the monte carlo were allowed to start in the target

region with the target removed and all the material along the beam line included (as it was under actual data taking conditions). The total energy of all resulting particles striking the upstream surface of the FCAL was added together and stored in a variable E_{Hit}. The simulated reconstructed signal E_{Raw}, shown in figure 44, was then compared to the calibration data, figure 45, to obtain the over all normalization factor for the monte carlo. At this point the monte carlo would accurately reproduce the raw signal for single particles.

Fitting the Calibration Curve & Determining the Resolution

The calibration curve itself was obtained from over 1000 multiparticle events generated with the ISAJET[28] kinematics algorithms. These events had relatively high energy in the forward region (MINBIAS algorithm) and dominate the curve near the high energy limit. We generated a second set of data at a value of $\sqrt{S} =$ 16 GeV in order to more completely cover the lower energy regime. The energy spectra (E_{Hit}) for these events are shown in figure 46. A scatter plot of $\frac{E_{Hit}-E_{Raw}}{E_{Raw}}$ $=\frac{\Delta E}{E}$ versus E_{Raw} is seen in figure 47. The calibration curve was obtained by fitting this data to a function of the form

$$\frac{\Delta E}{E} = A_0 + A_1 E + exp(A_2 E) \qquad \text{(III.8)}$$

over the range of $E_r = 50$ to 800 GeV resulting in the following values:

Table 6 **Calibration Curve Parameters**

Parameter	Value
A_0	3.13×10^{-1}
A_1	-7.44×10^{-4}
A_2	-2.31×10^{-2}

It should be noted that the higher order terms are much smaller smaller than the lower order terms and so make their most significant contributions at the lowest energies. As can be seen in figure 48 the results of applying this calibration curve to the monte carlo data produces a fairly uniform detector response across the entire kinematical region with a residual error of $\frac{\Delta E}{E}$= 9.0% as shown in figure 49.

Calibration Data

Reconstructed energy spectra for 50, 100, 200 and 530 GeV calibration beams are shown in figure 50. As indicated previously, these spectra do not peak directly over their nominal values due to the differences in the detector's response for single particle events in contrast to multiparticle events with the same energy. Two peaks are clearly visible at the lower energies where a large number of very high energy electrons have contaminated the calibration beam. A useful parameter for investigating this phenomenon is the longitudinal asymmetry α in the upstream module defined as $\alpha = \frac{E_u - E_d}{E_u + E_d}$ where E_u, E_d are the reconstructed energies in the upstream and downstream sections respectively. A plot of this asymmetry as a function of the reconstructed energy for the 50 GeV calibration data is shown in figure 51. Note that the energy spectra for events with $\alpha < 0.2$ (the deeply penetrating hadrons) peaks much lower than that with $\alpha > 0.2$ (the quickly absorbed γ 's and e's). The asymmetry was used to distinguish between electrons and hadrons. For showers due to single particles our $\frac{E_e}{E_\pi} \approx 1.40$.

The resolution σ_E decreases with increasing energy as can be seen in figure 52. This is as expected from equation III.1. Superimposed on this plot is the function $\frac{\sigma_E}{E} = \frac{130\%}{\sqrt{E}}$ which represents the best fit to the data.

REFERENCES

[23.] U. Amaldi, Physica Scripta, Vol. 23, pp. 409-424 (1981).

[24.] Ibid.

[25.] C. Fabjan, Techniques and Concepts of High Energy Physics-III, T. Ferbel, ed. (Plenum Pub. Corp., 1985).

[26.] Op. Cit.

[27.] Ibid.

[28.] Fermilab publication PM00053.

CHAPTER IV. DATA ACQUISITION & SOFTWARE

There were over 23,000[#18] channels of information which were accessible in each of the $\approx$ 3.7 million events[#19] collected during the course of this experiment. Clearly a tremendous amount of computing power and associated software was essential for the operation of the detectors and analysis of their data. Because this topic is so vast in its scope and extremely technical in its substance merely an outline of the data acquisition (DA) system and its software will be provided here.

§ IV.1. Data Acquisition Hardware

The hardware in the DA system for E706 is diagrammed in figure 53. The basic operating philosophy in this system was that the entire procedure be conducted and synchronized by the central DA μVax. The four PDP's, 11 MX's and the confusion of CAMAC, NIM and RABBIT environments were as slaves to this one system's master. Before data taking began, the μVax would send out all the necessary instructions to initialize the electronics, assign tape drive units to the output streams, assign all the CD links to the input streams, perform all the bookkeeping tasks and enable the actual triggering of the experiment. Once the system had been initialized and data taking commenced the μVax would receive the data from each of the four input streams (PDP's) and pack it along with some of the relevant local parameters[#20] into a single data structure which was

---

#18 Cerenkov detector = 14, Scalers = 138, SSD = 712, PWC = 13,440, EMCAL = 6264, HCCAL = 2368, FCAL = 472

#19 1,798,881 positive beam + 1,936,886 negative beam

#20 E.g. The run number

then sent out to the tape drive and a variety of additional consumers.

The trigger signal itself originated in the latch house's trigger logic after the information from all the apparatus had been received. This signal was sent to a BISON box[29] where the global DA ("B") interrupt was formed and broadcast to all the apparatus thereby initiating the DA procedure on the PDP's. Each of the PDP's formed its own subevent data structure from the data it extracted from the latches independent of the 3 other PDP systems. Once a subevent was assembled the PDP's signaled the μVax and the μVax then concatenated the subevents into a single global data structure. This global data structure was then directed to the output streams according to their priority. The tape unit which recorded the permanent record of the data always had highest priority so that none of the triggers could be lost from this stream.

In addition to the μVax which we used for the online DA we employed two additional μVax's and a Vax 780 for both the online and offline analysis. After the entire run was over this was increased to include a VAXstation 2000 and 3100, three VAX 3200's and the considerable resources of the associated universities and Fermilab itself for assisting in the offline analysis. The bulk of our processing of the data was performed with the Fermilab Advanced Computing Project's (ACP) cluster of CPU farms[30]. These ACP machines had up to 56 nodes (CPU's) running in parallel and each of which drew upon 6 MBytes of local memory. The processing nodes themselves had a serial architecture. However, the "parallelism" above refers to the fact that these nodes would process information without any regard to their neighbors beyond that dictated by their competition for the communications link to the master CPU.

§ IV.2. Computer Software for the Data Acquisition

A tremendous amount of the software for this experiment was developed outside the E706 collaboration and was suitably tailored to meet the specific characteristics of our apparatus[31]. The computer's logic for data acquisition in terms of the more extensive pieces of imported and domestic code[#21] are diagramed in figure 54. Of particular merit is the recognition that at each stage of the DA one encounters a different level of abstraction as far as the code is concerned; the electronics with its packing of binary data into 32 bit words in a CAMAC environment represents one extreme while the interactive, cursor driven, color graphics analysis packages implementing a commercial product (DI3000) represents the opposite extreme. As the 1987 → 88 run was the first for this apparatus all of the software for E706 was either created from scratch or extensively modified from previously existing versions. Perhaps even more impressive than the complexity and sophistication of all this computer hardware and software is the realization that it all was created and integrated into a completely functional system within a two year period almost entirely by physicists without any formal education in computer design or programming.

#21 "Domestic code" ≡ entirely developed by members of the E706 collaboration

REFERENCES

[29.] Fermilab publications HN 3 and PN 101

[30.] Fermilab Publications ACP 4,5,6,7,8

[31.] Fermilab Publications BD 1;DS 105, 113, 120, 121, 122, 123, 125, 126, 128, 129, 169; RN 2, 21, 22, 23, 24;PN 93, 96, 134, 159, 160, 252, 254, 255, 271, 272, 277, 278, 279, 280, 285, 289, 302, 304, 315, 318, 323, 382

CHAPTER V. CHARACTERISTICS OF THE FORWARD JET

The data described in this chapter fall into one of two categories according to the trigger requirements they satisfy: Interaction (Minimum Bias) triggers and High P_T LAC triggers. The data set was obtained during the first two months of 1988 when both positive and negative beams were collided with copper and beryllium target, resulting in $\approx$ 2 million triggers for each polarity of the beam. Since most of the interactions of the beam resulted in an Interaction trigger, these triggers were reduced by a factor of 10^4. This reduced their contribution to the overall trigger rate to a level somewhat below that of the much rarer high P_T events.

The high P_T LAC triggers[32] were of two types, both of which were intended to respond to high energy photons or photon combinations. Local triggers required a local deposition of energy in the EMCAL that exceeded some minimum trigger threshold. Global triggers added all the energy in an entire octant of the EMCAL together before checking to see whether the trigger threshold was exceeded. These triggers selected relatively rare events which were most likely due to hard parton-parton scattering, and were combined in this analysis. All the high P_T triggers were software selected to have at least 1 photon or multi-photon combination with a total momentum transfer P_T of at least 3 GeV/c. "Interaction" triggers required only one or more of the interaction counters to fire and thus selected a sample of all possible interactions with minimal constraints. Selection criteria winnowed the number of these interaction events down to 25,374 triggers for the negative beam and 8359 positive triggers. 16,238 ("select") high P_T events

remained after additional severe offline cuts were applied to remove events feeding into the sample from the extremely copious lower P_T events. Both these data sets had 86% of their events with a vertex reconstructed in the beryllium target with the remaining 14% in the copper.

This chapter will have an initial section, in which the basic elements and quantities in this analysis are introduced followed by two sections which study the correlations between the forward jet and the highest P_T particles in these events for each of the two main categories of events.

§ V.1. Categories of Objects

There were 4 categories of objects defined in this analysis: charged tracks, photons, hadrons and forward jet.

§§Charged Tracks

A charged track was any entity which was reconstructed in the PWC+SSD system that passed within 1 cm of the reconstructed vertex. All charged tracks had reconstructed segments both upstream and downstream of the analysis magnet. These segments were required to intersect in the center of the magnet.

§§Photons

The photon analysis was by far the most extensive collaborative effort as it formed the core of this experiment. Here we simply describe some of the cuts which were significant in this study and direct the interested reader to one of the principle photon study architect's thesis[33] for further details on the photon reconstruction algorithms.

To distinguish between photons and charged particles striking the EMCAL it was required that no reconstructed charged track point to within 1 cm of a reconstructed photon candidate. Similarly, when a reconstructed hadron shower in the HCCAL was projected onto the upstream surface of the EMCAL and fell within 10 cm of a photon candidate, the photon candidate was rejected.

To remove massive particles from the photon sample a parameter (α) which measures the longitudinal spread of a shower was introduced. This longitudinal "asymmetry" consisted of the difference between the shower's reconstructed energies in the front and back readout section of the EMCAL normalized to the shower's total energy, i.e. $\alpha \equiv |\frac{E_{\rm front}-E_{\rm back}}{E_{\rm front}+E_{\rm back}}|$. Photons rarely penetrate much material before depositing the bulk of their initial energy. Requiring $\alpha > 0.8$ resulted in negligible hadron contamination in the photon sample.

Muons also formed a significant source of background to the photon signals. They were created far upstream and traveled parallel to the beam and clearly did not originate from the primary vertex of the interaction. These particles were identified with a "directionality" parameter which was the radial separation between the centroid of the energy in the back readout section and that in the front when the energy in each section was projected onto the upstream surface

of the EMCAL. All showers with a separation greater than 0.4 cm were removed from the data.

Furthermore, photon candidates were required to be within -10 nS to +40 nS of the trigger in order to remove particles out of synchrony with the rest of the event. To assure that the reconstructed particles were indeed genuine and in the kinematic region where the reconstructor was highly efficient the photons were required to have a minimum total energy of 2 GeV. A photon candidate was accepted as a real photon only when all the preceding criteria were satisfied.

§§Hadrons

Hadrons reconstructed in the HCCAL were required to have a total energy of at least 10 GeV, reflecting the very high noise rate below this level. No other cuts were placed on these objects and they constitute a very small fraction of the energy in most events.

§§Forward Jet

The forward jet had three requirements placed upon it and a failure to meet any of these preconditions by an event resulted in that event's removal from the data set. In order to insure that the information from the FCAL did not mix multiply occupied beam buckets or overlapping event structures in the data set the following requirements were imposed:

1. No BEAM or INTERACTION signal within ± 2 beam buckets (38 nS) of the trigger

2. Total Energy in the FCAL < 800 GeV

3. Centroid of the forward jet within acceptance of the FCAL (radius of 32 cm)

§ V.2. Constraints on the Data Set

Since the following analysis concerns gross topological features of the data it was not essential that the final sample contain all possible events but rather that systematic biases be understood and removed (when possible). Events were classified according to whether a photon or a charged track carried the highest P_T in the event. For global P_T LAC triggers, where a pizero or some other composite object was responsible for the trigger, the highest P_T photon would only carry some fraction of the trigger P_T and, in some cases, would have a charged track in the same event with an even higher P_T. In this case the event would not be included in the high P_T photon sample but would be placed in the high P_T charged track sample. In addition to the above, the following definitions were developed to clearly identify the genuine interactions from spurious events.

Table 7 Table of constraints on the data set

Detector(s) involved	Requirement	Purpose	Triggers
Beam counters	BA, BB and not BH	Define beam	All
Interaction counters	Two of SE1, SW1, SE2 or SW2	Define interaction	All
Trigger	P_T in EMCAL above threshold	Select hard scattering process	High P_T
Veto Wall	VW Plaquette in trigger quadrant not fire	μ suppression	High P_T
SSD	More than 2 tracks with an impact parameter of less than 50μm in the target stack	Identify vertex	All
SSD + PWC	Tracks link through magnet and have impact parameter of less than 1 cm with the vertex	Charged track identification Fake track suppression	All
SSD + PWC + EMCAL + HCCAL	Photon with energy, timing, and directionality cuts	Identification of photons	All
SSD + PWC + HCCAL	Hadron with energy cut and charge identification	Hadron identification	All
Beam + Interaction counters + FCAL	Timing, energy and position cuts	Forward jet identification	All

§ V.3. Interaction Triggers

The Interaction Counters (see §II.6) covered the pseudo-rapidity intervals $\eta = [-2.0, +0.7]$ on the upstream counters and [+0.2,+1.9] on the downstream counters. These counters formed the primary signal for the interaction trigger and

at least one counter had to fire in order to satisfy the interaction trigger definition. The purpose of these triggers was to acquire a set of data with a minimum number of constraints on the underlying kinematics in order to study the backgrounds to our hard scattering data set. Several offline requirements have been added to the online interaction definition in order to remove triggers that were found to be due to accidental coincidences and noise in the readout electronics which mimicked an interaction trigger. Most significantly, we imposed a requirement that a vertex be reconstructed (using a minimum of 3 SSD tracks[#22]) which has two advantages: it allows the identification of the specific target element for the interaction and it offers a means of distinguishing charged tracks originating in the primary vertex from those resulting from secondary interactions elsewhere. These requirements actually excluded two classes of interactions which form a significant part of the total cross section: elastic scattering, which contains only 2 outgoing tracks, and diffractive dissociation where several outgoing particles, mainly pions, travel almost precisely along the beam axis with negligible momentum transfer to the target.

In figure 55 we show the forward energy spectra for a variety of interaction counter multiplicities for both positive (proton) and negative (pion) beam. We see no compelling differences between these two data sets. Consequently, the data have been added in all further analyses. Despite the constraints the vertex requirement has imposed on these data, the spectrum with only one interaction counter being struck is identical to that of a selection of beam triggers which are

#22 Note that SSD tracks are not the same as the charged tracks defined above as they are not required to link up with a track in the planes downstream of the magnet as the charged tracks must do.

known to have no interaction in the target. They are believed to be a consequence of accidental triggers and have been excluded from the data sets.

Figure 56 shows the mean charged particle multiplicity for these interaction triggers as a function of K, the inelasticity, defined as $1 - \frac{E_{FCAL}}{E_{Beam}}$. In these data events with $E_{rec} > 425$ GeV have been excluded since they clearly include contamination from overlapping events and/or gross reconstruction errors. The data indicate that, as expected, the charged particle multiplicity increases with increasing values of K except near K=1. This latter effect may be an artifact arising from diffractive interactions (which yield fewer secondary particles) and where most of the forward energy goes into the beam hole in the FCAL.

In order to compare the charged particle multiplicity distributions to other data, figure 57 shows the the charged particle multiplicity distribution along with the KNO scaling violating function determined[34] by the UA5 collaboration to account for data from $\sqrt{S} = 10$ to 1000 GeV. This function has the form

$$P(n, \langle n \rangle, k) = \frac{k}{n(n-2)} \frac{\langle n \rangle^n k^k}{(\langle n \rangle + k)^{n+k}} \qquad \text{(V.1)}$$

$$\langle n \rangle = (2.7 \pm 0.7) - (0.03 \pm 0.21)\log_e(\mathrm{S}) + (0.167 \pm 0.0162)\log_e^2(\mathrm{S}) \qquad \text{(V.2)}$$

$$\frac{1}{k} = -(0.104 \pm 0.004) + (0.058 \pm 0.001)\log_e\left(\sqrt{\mathrm{S}}\right). \qquad \text{(V.3)}$$

While the shapes of these two curves are very similar it appears that the interaction triggers have roughly 1 to 2 tracks fewer than the UA5 function would predict. One possible explanation might be that the present data do not exactly

match the minimum bias criteria. However, all the additional hardware and software constraints on the events would tend to conspire towards selecting slightly more energetic collisions which would have a higher charged particle multiplicity spectrum rather than a lower one. It is most likely that these tracks are lost to two distinct mechanisms: acceptance limitations and secondary scattering. The first produces losses by having the the target fragments fail to pass through the spectrometer at all. In the second mechanism a secondary scattering event knocks the particle outside the acceptance or causes it to be absorbed.

Our results may also be compared to those from other experiments by comparing the charged particle multiplicity dependence on the energy deposited in the central region. The effective energy available in the central region can be written as $\sqrt{S_{\text{effective}}} = \sqrt{S} * K$. Figure 58 is a plot of the mean charged particle multiplicity as a function of $\sqrt{S_{\text{effective}}}$ (and is simply figure 56 multiplied by $\sqrt{S}$ = 31.5 GeV). The dashed line on this figure represents the data of Brick et al[35] at 200 GeV, which is shown in figure 59. The two sets of data agree very well at low energies while Brick's data at the highest energies seems to show a lower mean multiplicity than ours. However, the data point of Brick et al at their highest energy falls directly on the corresponding point of our data which indicates that our data are consistent with each other. From this, we are confident that our definition of mean charged particle multiplicity and inelasticity correspond quite closely to those used in other experiments.

In figure 60 is plotted the inelasticity as a function of the momentum transfer (P_T) of the highest P_T charged track for the interaction triggers. Once more, no significant differences based on particle type or target material were observed.

A smooth transition from low inelasticities with $\langle K \rangle = 0.4$ to high inelasticities with $\langle K \rangle = 0.6$ occurs as the P_T increases to approximately 2 GeV/c. The similar plot for the highest P_T photon is identical, with poorer statistics.

§ V.4. High P_T LAC Triggers

Unlike the interaction triggers, the high P_T LAC triggers are strongly biased towards event topologies containing one or more very high P_T photons. At the highest P_T's (i.e. above 5 GeV) the photons are likely to be direct products of the fundamental hard scattering process itself as the background from other processes falls off with increasing P_T. It is therefore of interest to determine how the inelasticity for these events compares to the minimum bias events represented by the interaction trigger data set.

§§Inelasticity of the events

In figure 61 is shown the inelasticity as a function of the P_T of the highest P_T photon in the high P_T data set. Note that there are many events below the nominal trigger threshold of 2.5 to 3 GeV. These are attributable to global triggers in the data set. Global triggers typically have several isolated photons combining to satisfy the trigger criteria rather than a single photon. The single highest P_T photon will thus have a P_T smaller than the total P_T used for the trigger. The behavior of the inelasticity is very different than the behavior in the interaction trigger events. We find that K = 0.7 in the region from $P_T = 1$ to 4 GeV/c while above 4 GeV/c the inelasticity falls to a level similar to that of the interaction triggers. Figure 62 shows the particle multiplicities as a function of K for these events, and demonstrates that the amount of phase space available

for partitioning amongst the particles in the central region is reduced in direct proportion to the P_T taken away by the high P_T particle. This may provide some explanation as to why the inelasticity falls in figure 60. The high inelasticity at $P_T < 4$ GeV/c is a reflection of the hardness of the scattering in these events.

§§Correlations Between Forward Momentum and High P_T Photons

Evidence that the transverse momentum in the forward calorimeter is correlated with the direction of the trigger photon is seen in figure 63 and figure 64. The X (horizontal) and Y (vertical) components of momentum of the forward jet are plotted as a function of the azimuthal angle Φ of the highest P_T photon. The recoil of the forward jet is opposite that of the high P_T photon. We shall discuss two possible mechanisms for this effect: k_T biasing in the trigger definition and leakage from the away side jet into the forward region.

As indicated in chapter I there exists a thermal excitation momentum k for partons contained within a hadron and the magnitude of this Fermi momentum is a few hundred MeV/c. The hard scattering cross section falls very rapidly with momentum transfer P_T and is proportional to $\frac{1}{(P_T)^6}$ and so lower P_T processes are produced much more copiously than higher P_T processes. Consequently, at any given P_T there will be a large contribution from low P_T subprocesses where both the interacting partons have initial transverse momenta k_T in the **same** direction. This is illustrated in figure 65. To balance momentum, the remaining partons in the projectile form the spectator jet with k_T in the opposite direction. Thus the spectator jets would be expected to recoil opposite to the trigger particle strictly on the basis of k_T momentum conservation.

A second mechanism to explain the anti-correlation of the transverse component of the forward jet is leakage from the (non-triggering) recoil jet into the forward region. The amount of this leakage should depend on the rapidity of the trigger particle. The very highest P_T photons tend to have a more negative rapidity (i.e. be directed in the backward hemisphere) than do the lower P_T photons as can be seen in Figure 66. The recoil jet tends to have the opposite rapidity of the trigger particle[36] and so events with higher P_T photons may have more leakage from the away side jet into the forward region. Consequently, we can consider the P_T to be an indirect measure of the amount of recoil jet energy in the forward region.

In figure 67 the component of the momentum of the forward jet in the direction of the highest P_T photon is shown as a function of the P_T of the photon. At low P_T the forward jet appears to recoil opposite the highest P_T photon but then shows no correlation or perhaps even tends towards carrying some of the associated fragmentation products in the direction of the highest P_T photons. This does not support the leakage hypothesis which would predict that the recoil would increase as more of the recoil jet contaminates the forward jet. The data favor the k_T biasing hypothesis described above.

REFERENCES

[32.] C. Yousef, PhD. Thesis, Northeastern University, (1990) unpublished.

[33.] G. Ballocchi, B. DeSoi, A. Lanaro, J.P. Mansour, E. J. Prebys, D. Skow: all of University of Rochester, 1989; C. B. Lirakis, Northeastern University, 1989

[34.] UA5 collaboration, Physics Letters Vol. 138B No. 4(1984)

[35.] Brick et al Physics Letters Vol. 103B, No. 3 (1981)241, Physical Review D Vol. 39, No. 9 (1989) 2484

[36.] S. Easo, PhD Thesis, University of Pittsburgh, (1989) unpublished.

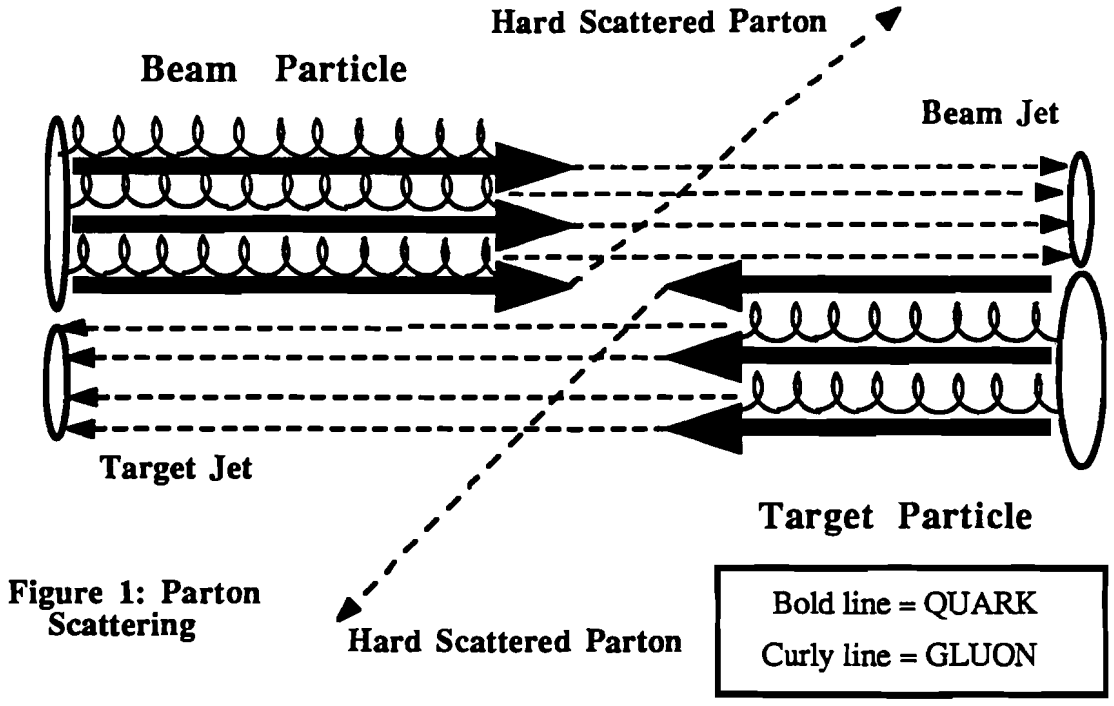

Figure 1: Parton Scattering

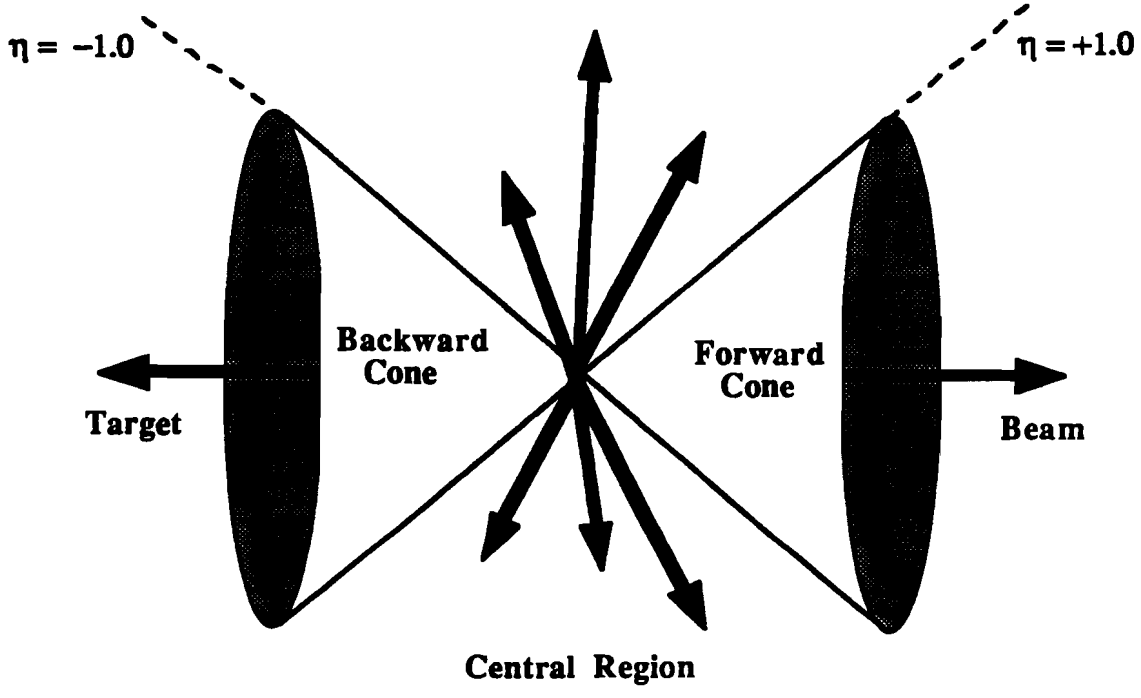

Figure 2: Scattering Regions

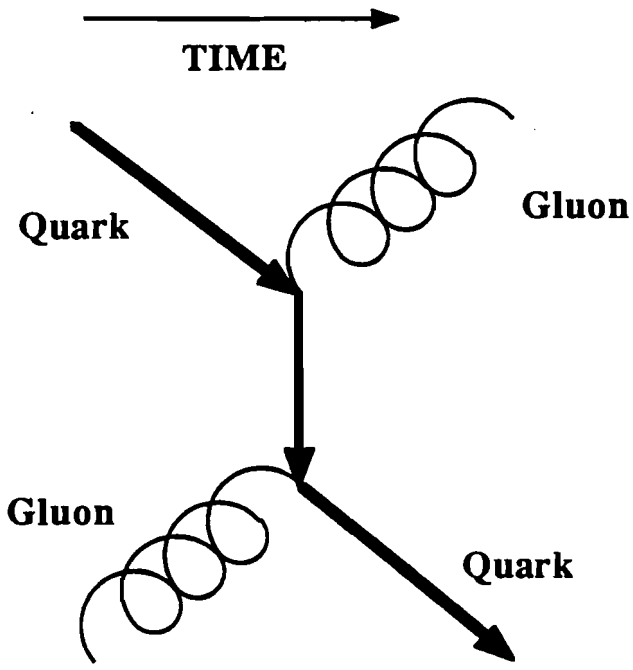

Figure 3: Compton Scattering

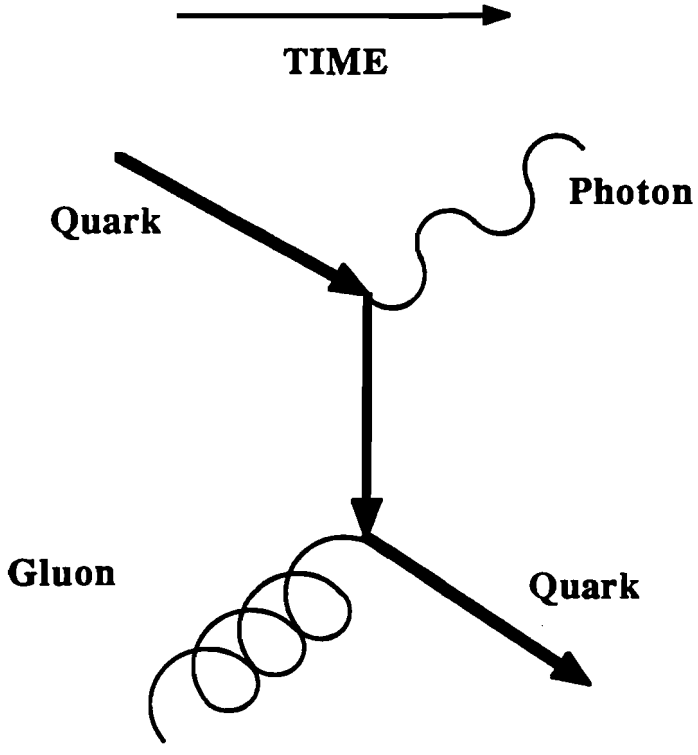

Figure 4: Direct Photon Production

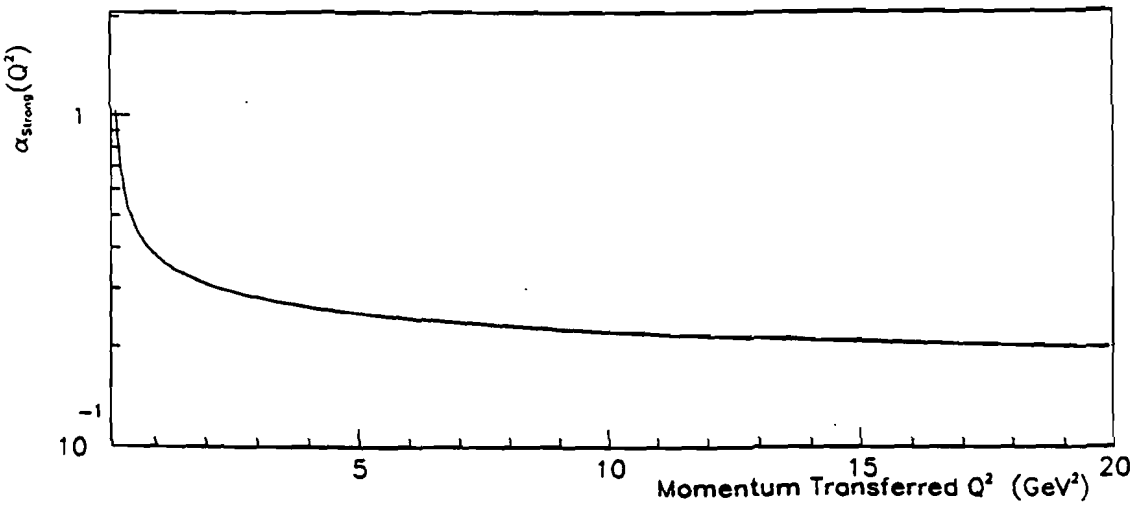

Figure 5: Q^2 Evolution of the Strong Coupling constant.

Figure 6: E706 Layout

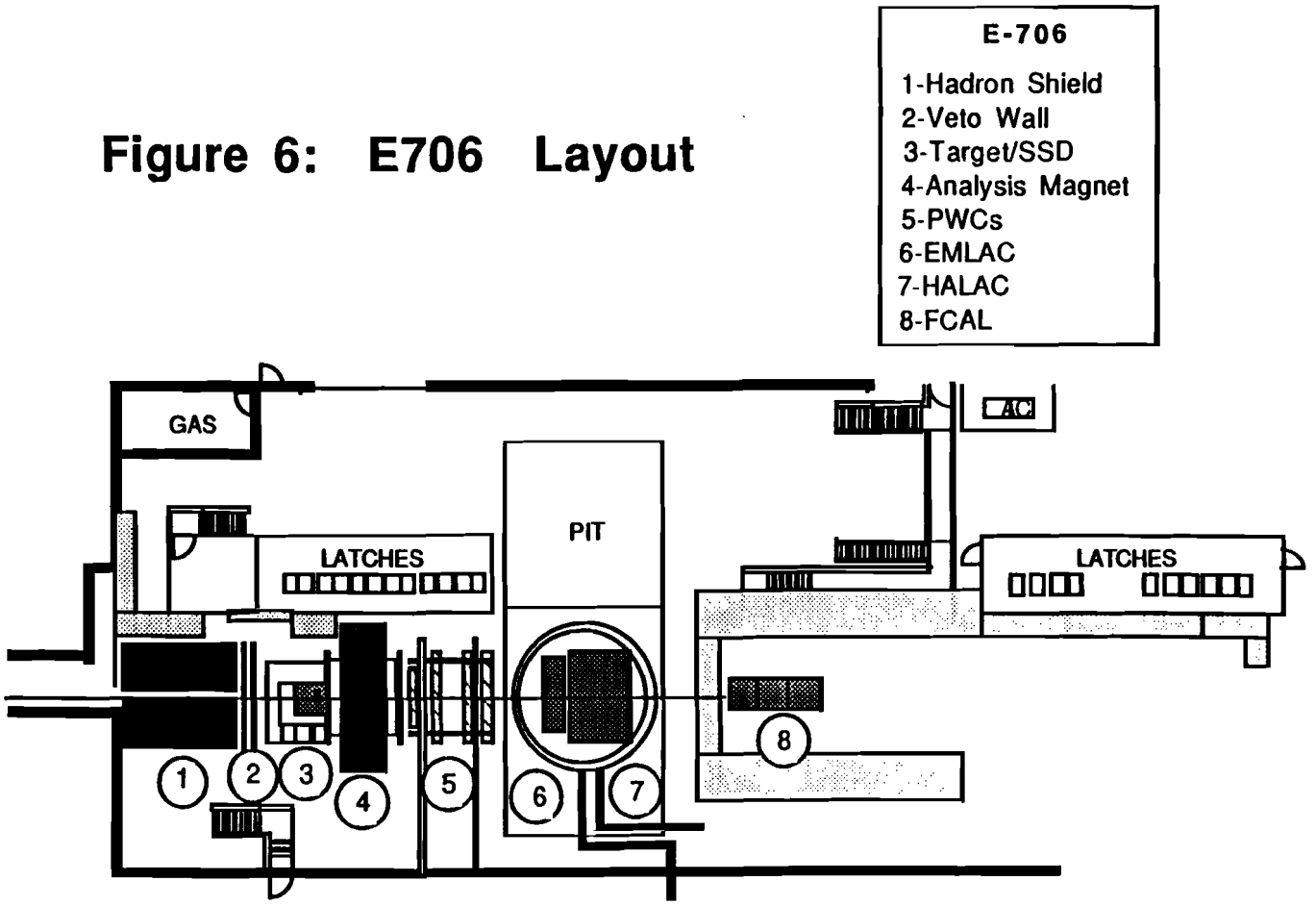

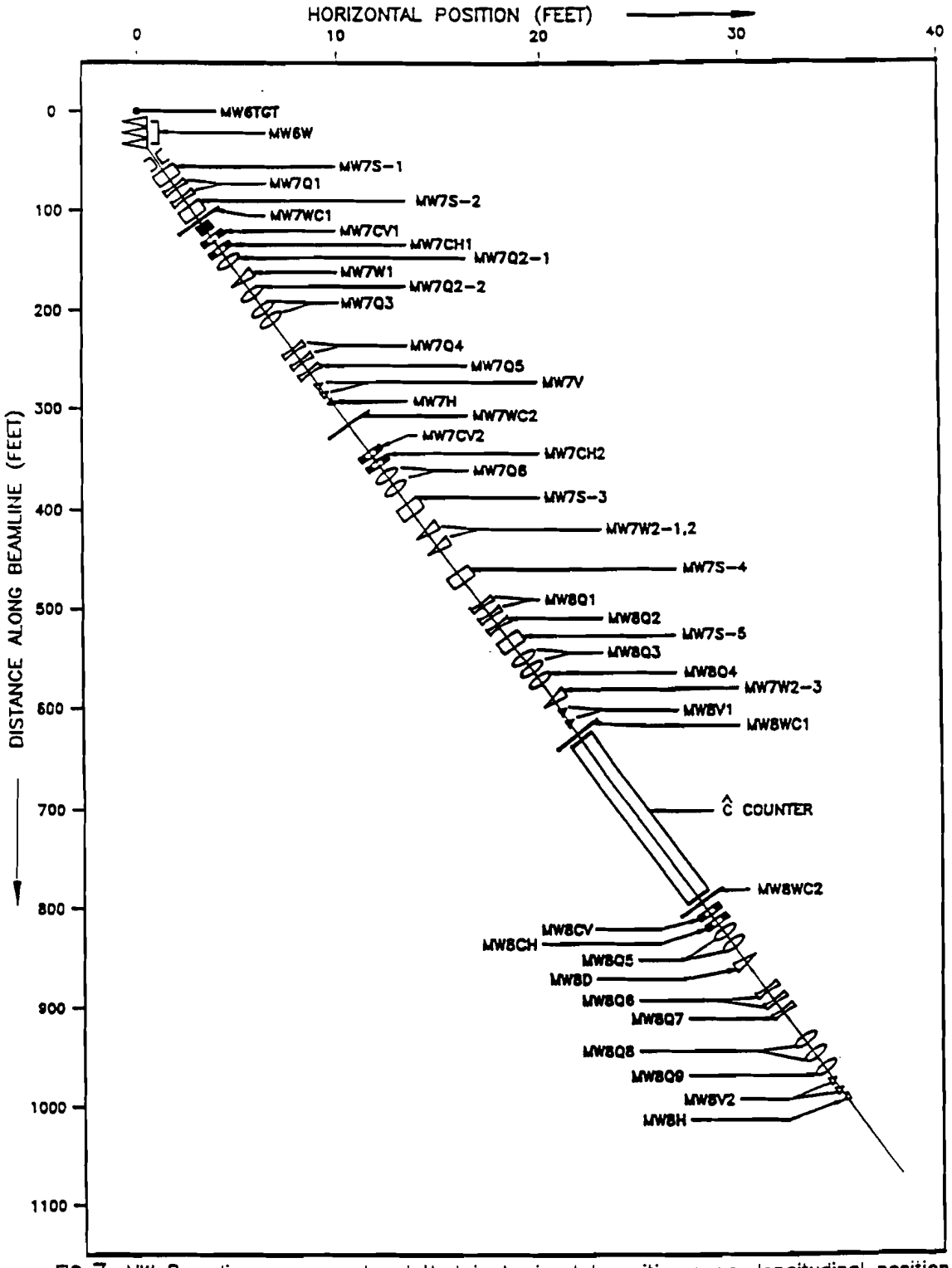

FIG. 7 MW Beamline components plotted in horizontal position x vs. longitudinal position

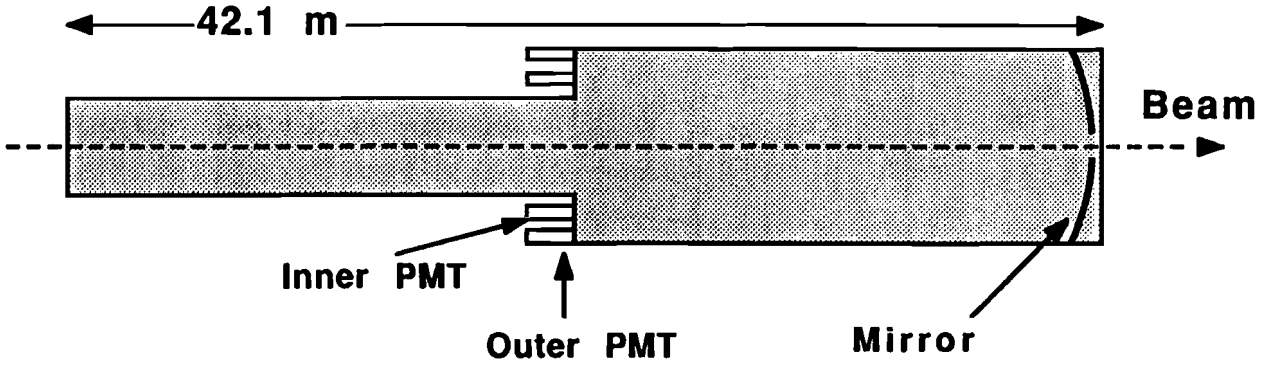

Figure 8: Differential Cherenkov Detector

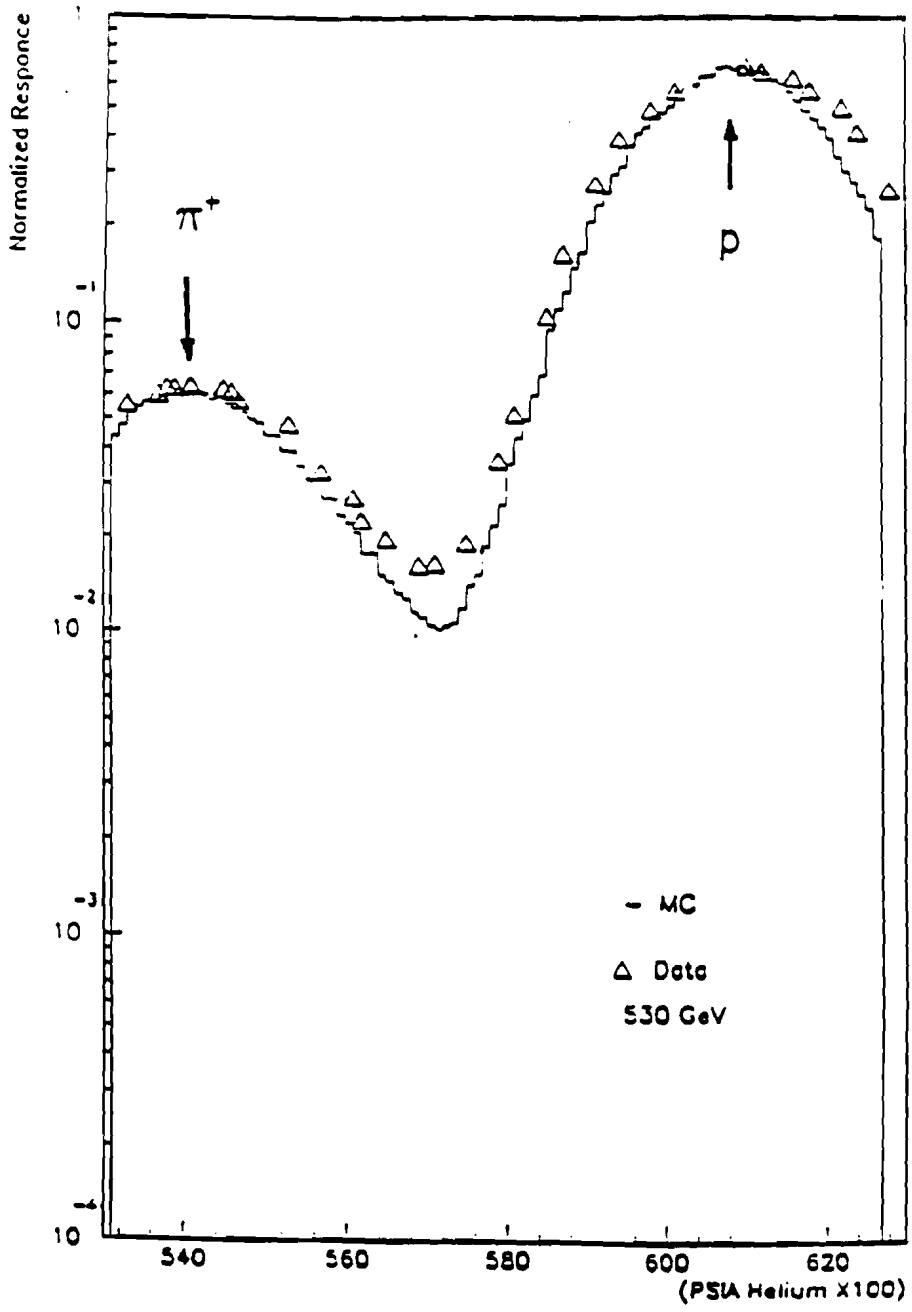

Figure 9 Experimental Cherenkov gas pressure excitations for positive beam. Indicated by the arrows are the particle types whose light is focused on the Cherenkov coincidence ring for specific values of the helium gas pressure. The solid line is a Monte Carlo fit.

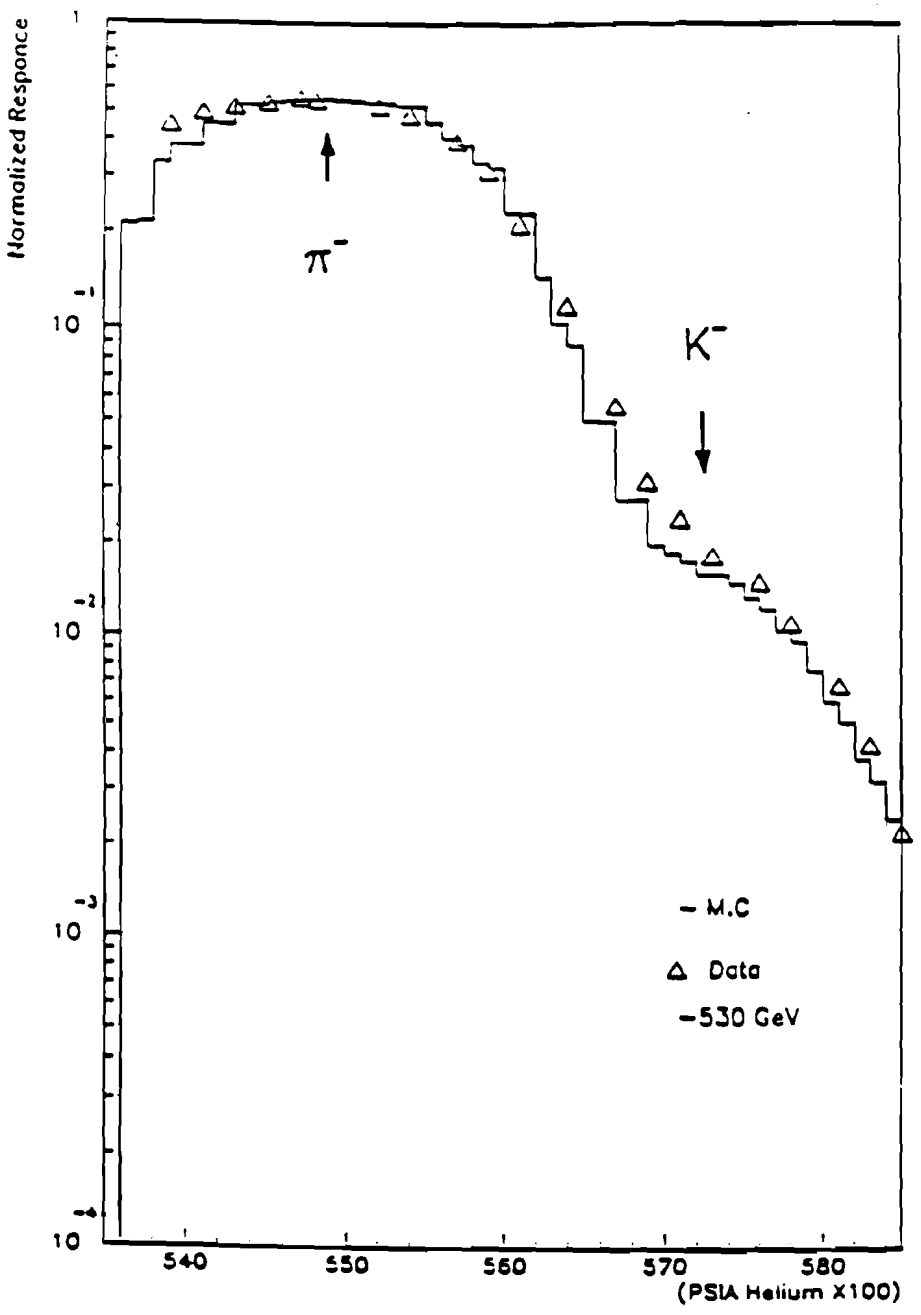

Figure 10 Experimental Cherenkov gas pressure excitations for negative beam. Indicated by the arrows are the particle types whose light is focused on the Cherenkov coincidence ring for specific values of the helium gas pressure. The solid line is a Monte Carlo fit.

Figure 11: Hadron Shield

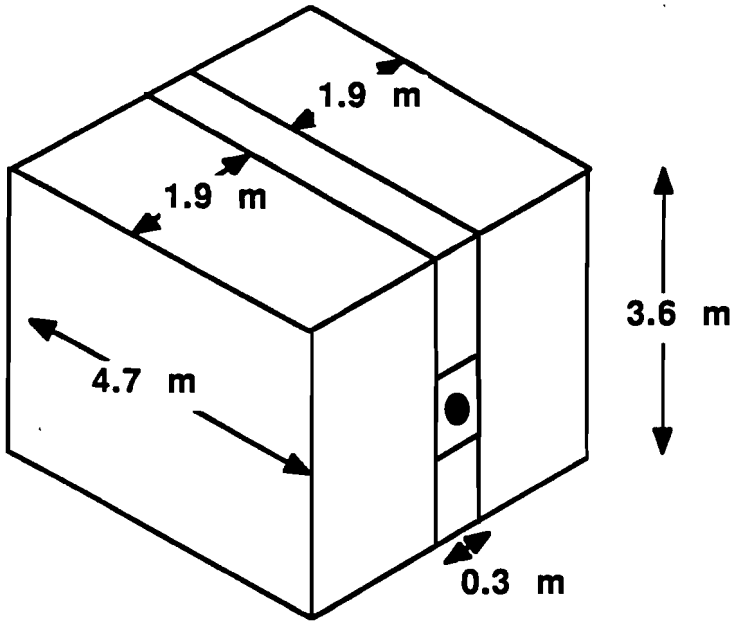

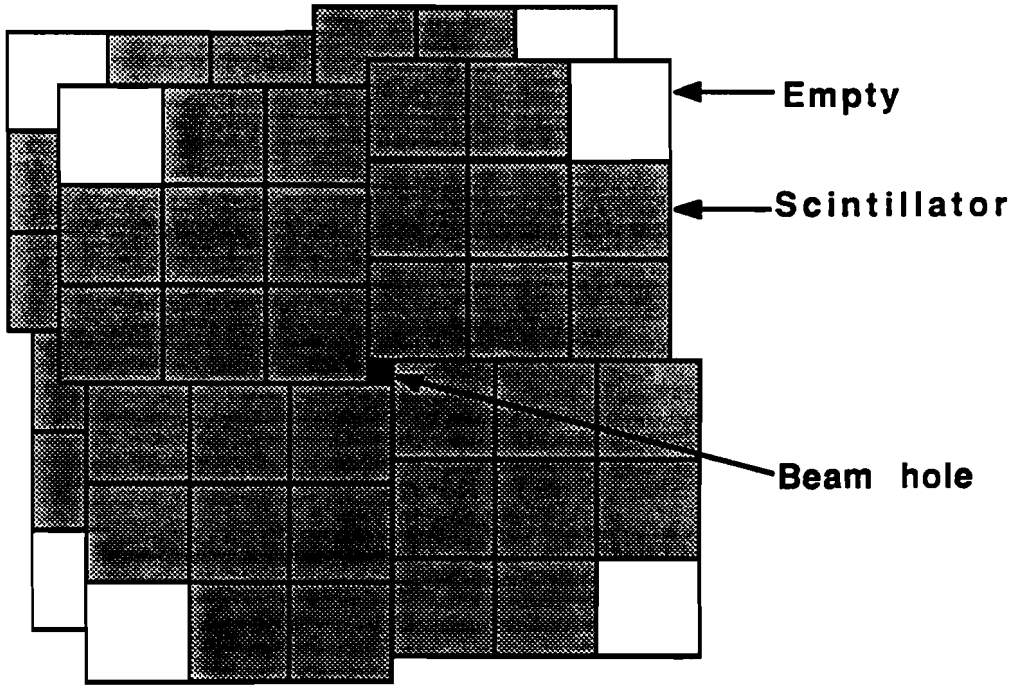

Figure 12: Veto Wall

Figure 13: Beam Counters

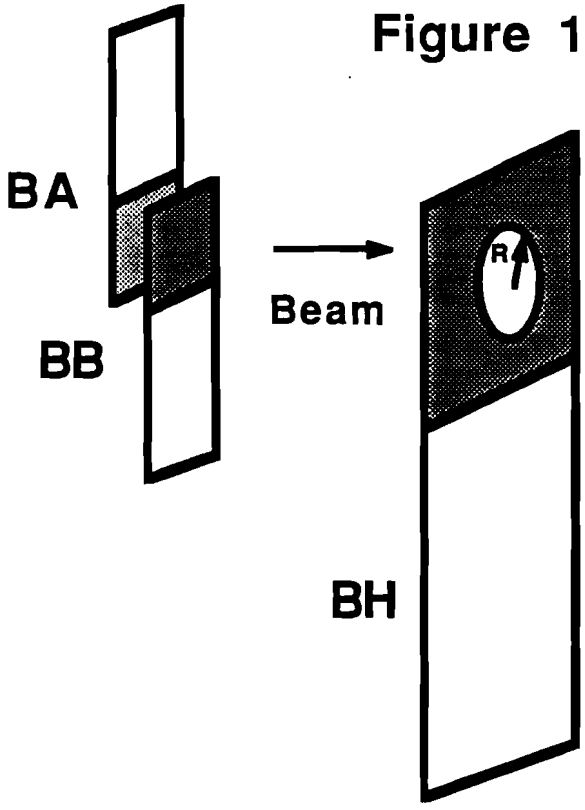

Name	Width	Radius	Z
Ba, Bb	1"	Na	-167 Cm
Bh	5"	0.2"	-164 Cm

Height = Width

Shaded areas = Scintillator

Unshaded areas = Light pipe

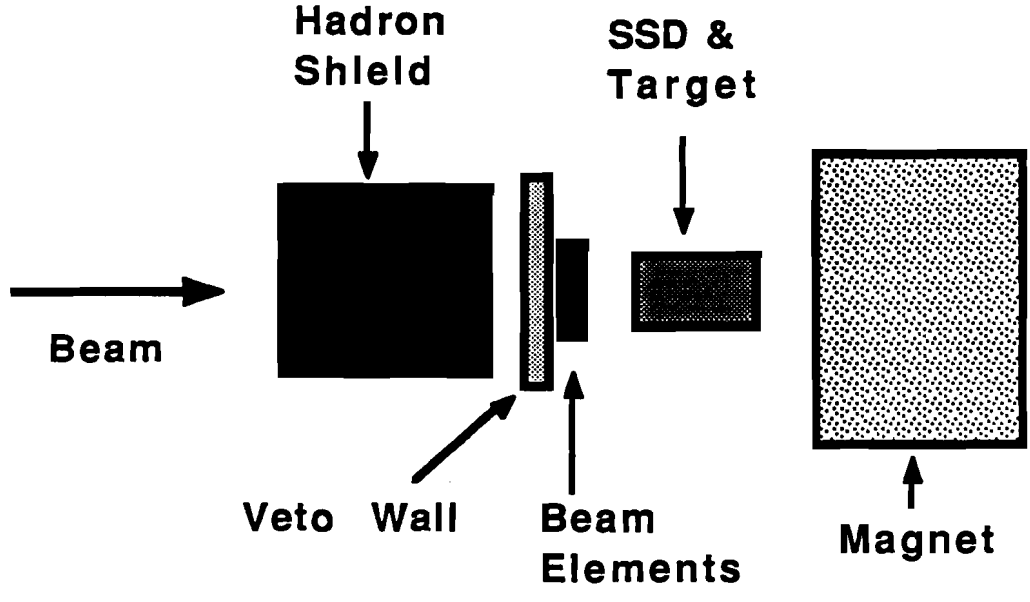

Figure 14: Interaction Counters

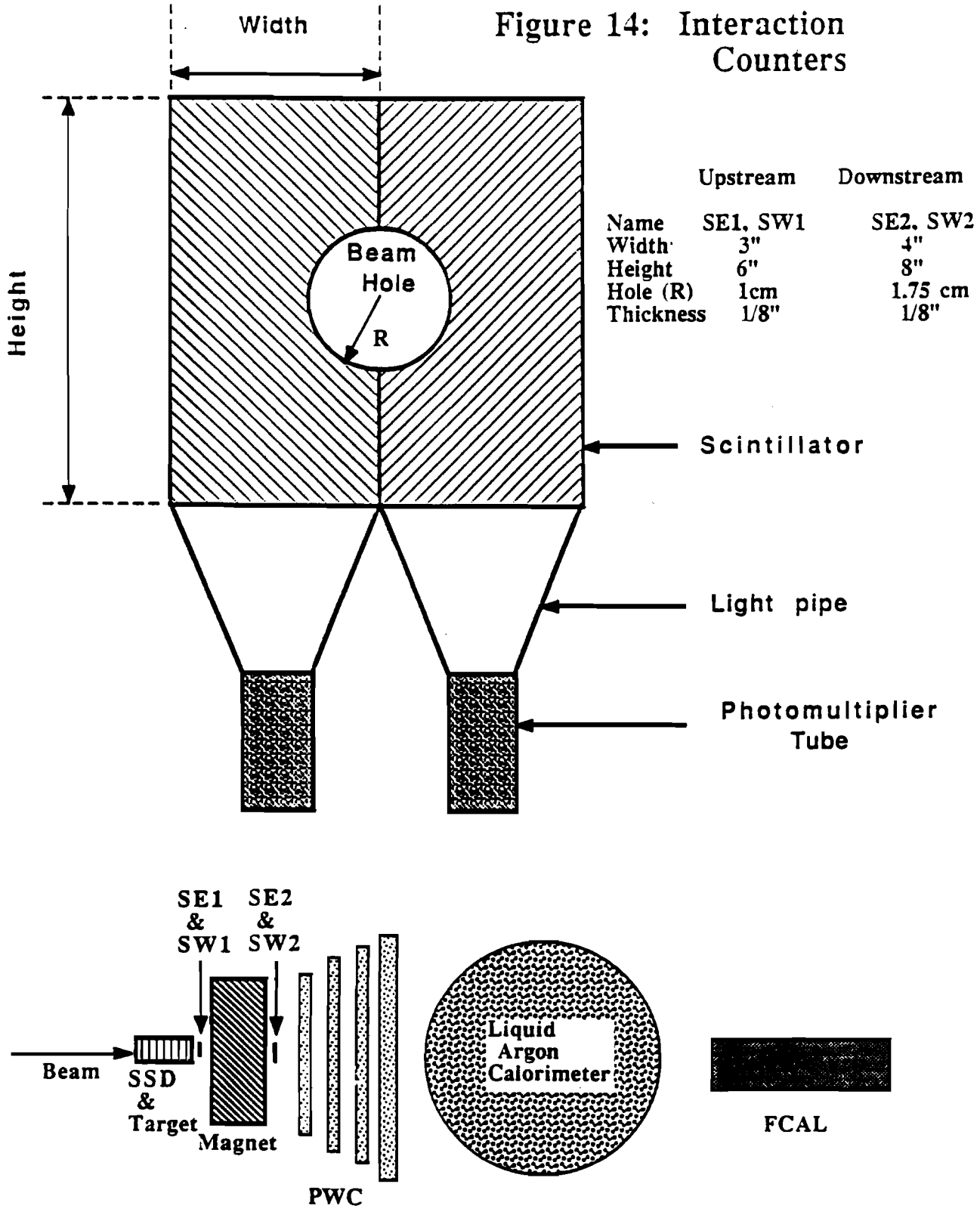

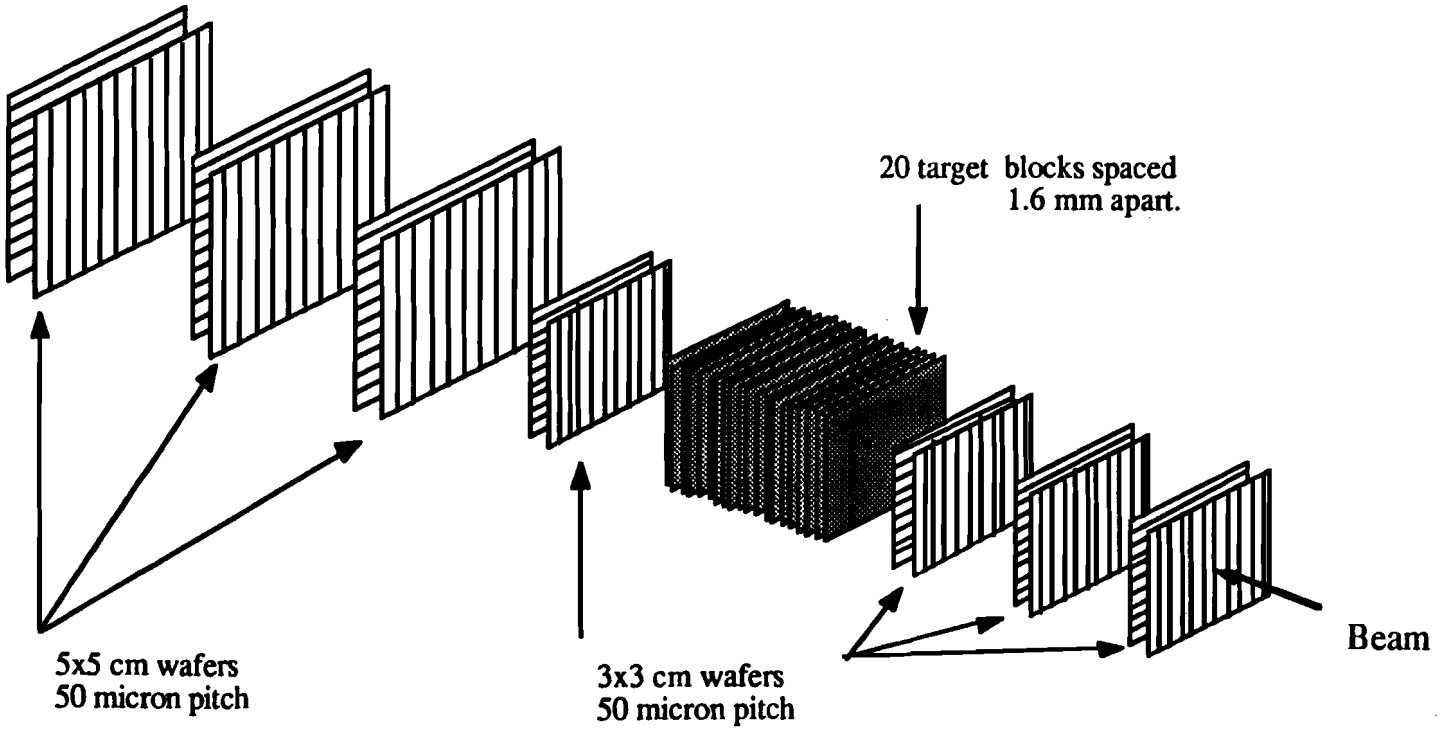

Figure 15: Vertex Detector

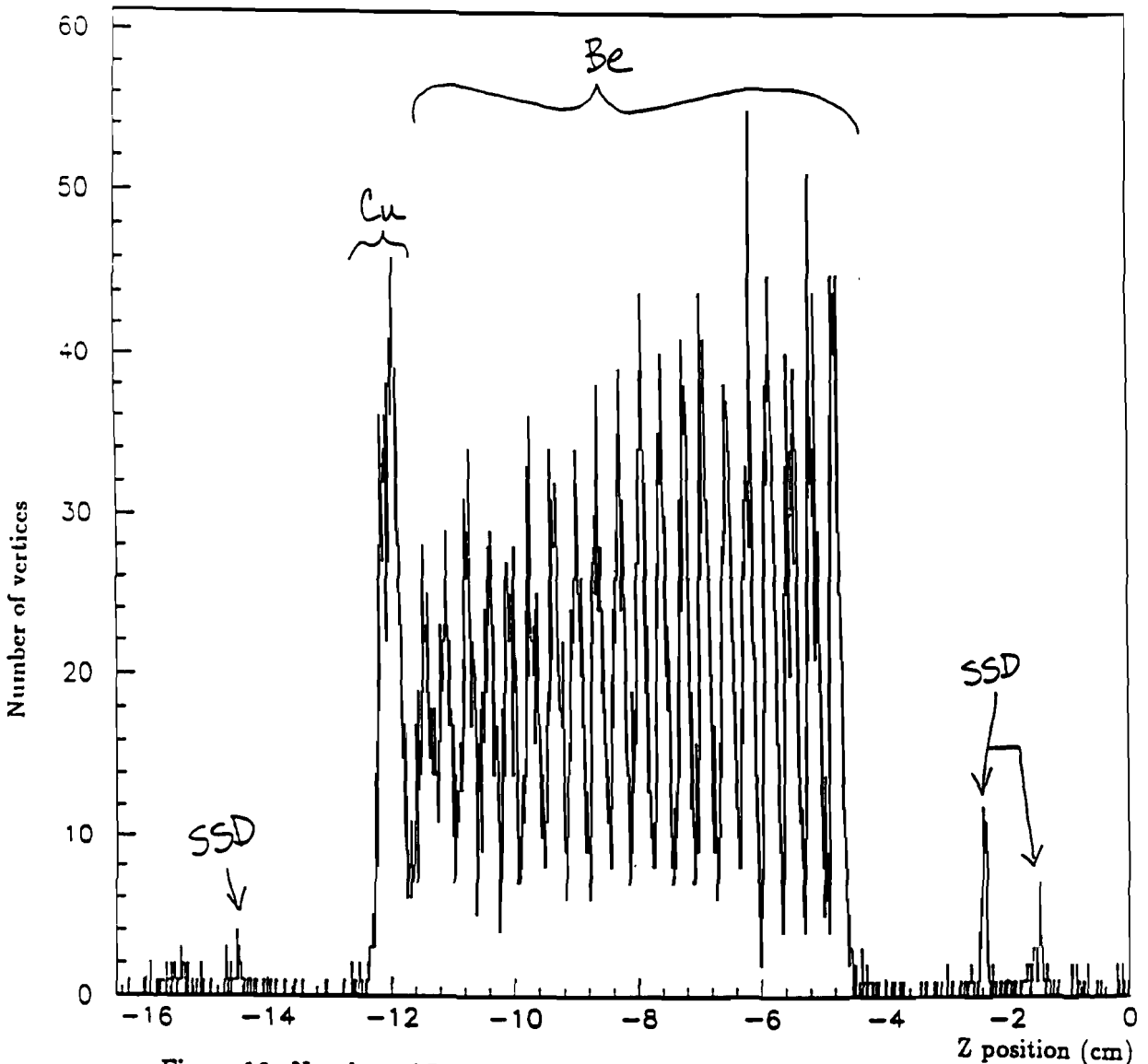

Figure 16: Number of Reconstructed Vertices as a function of the Z position.

Figure 17: LAC Dewar

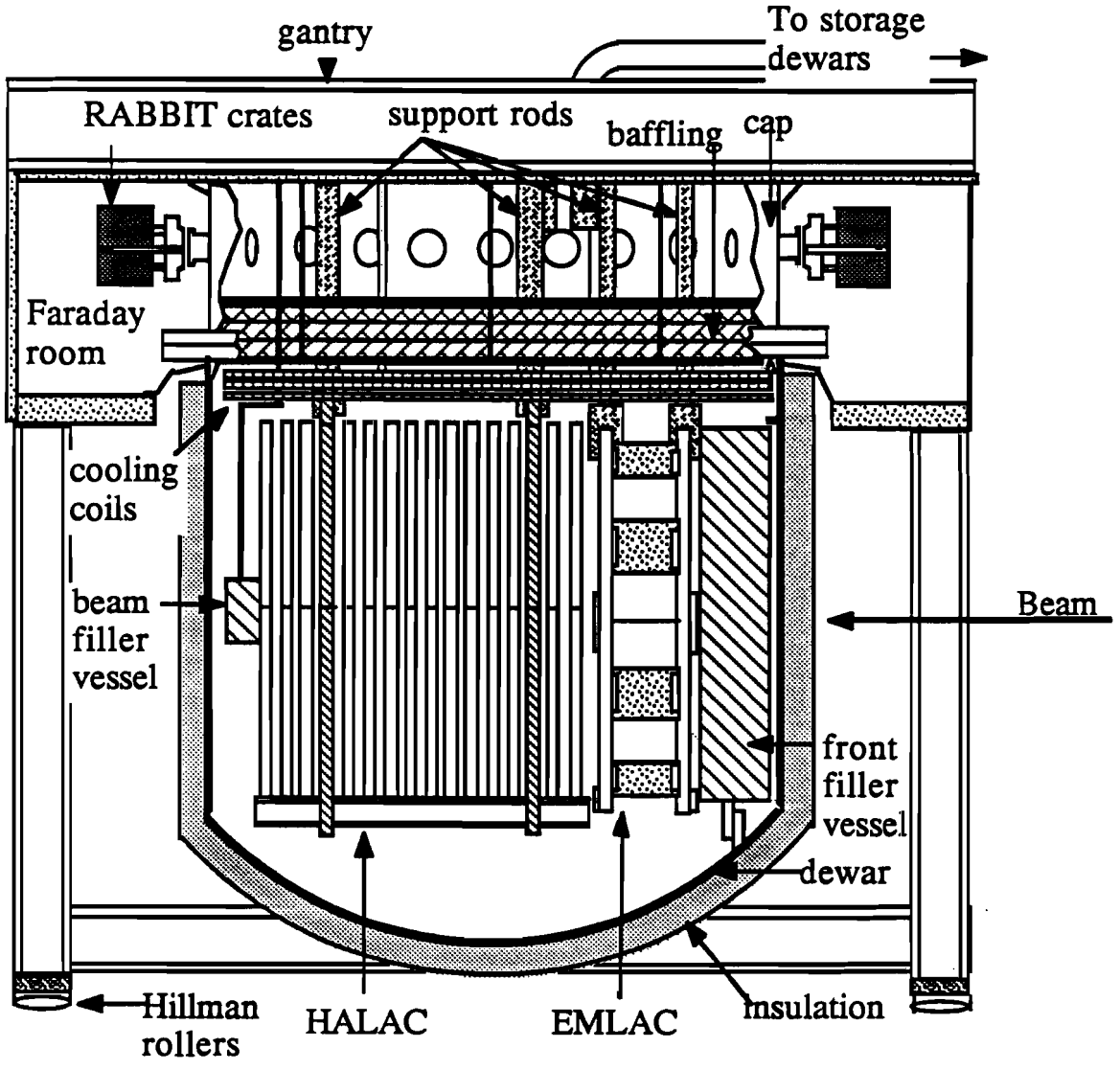

Figure 18: Photon Calorimeter

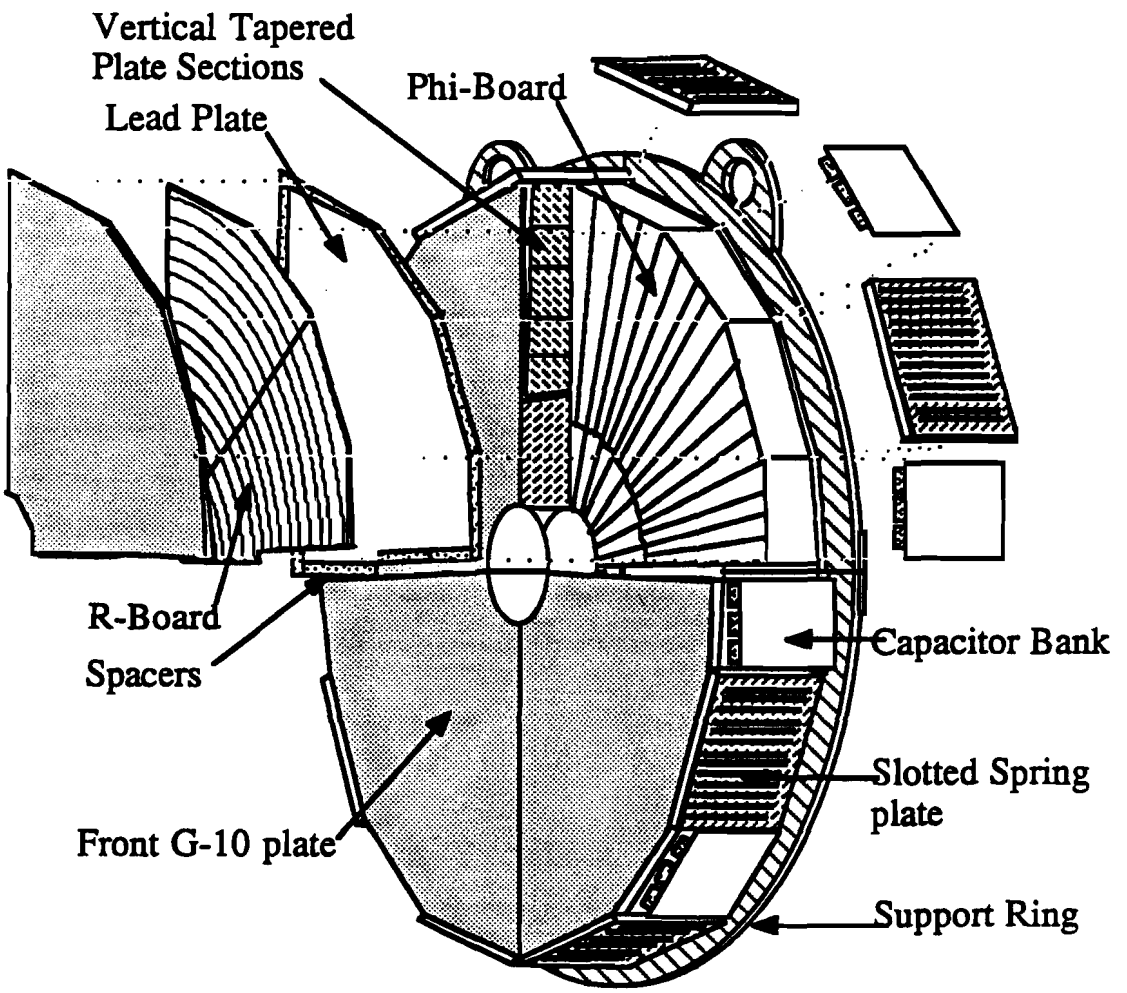

Figure 19: Hadron Calorimeter

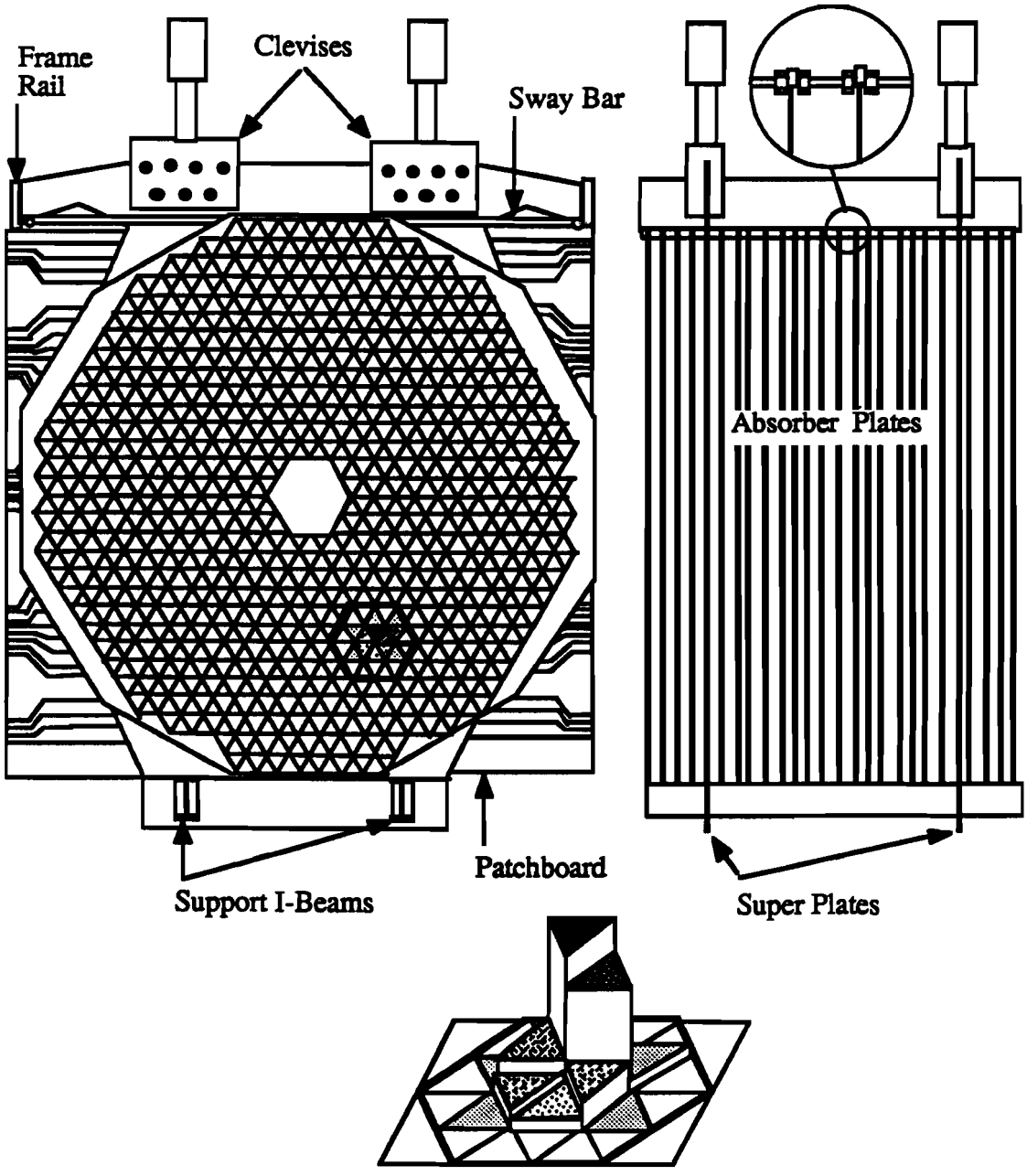

Typically 93% of a hadron's energy is contained in a 6-cell hexagon.

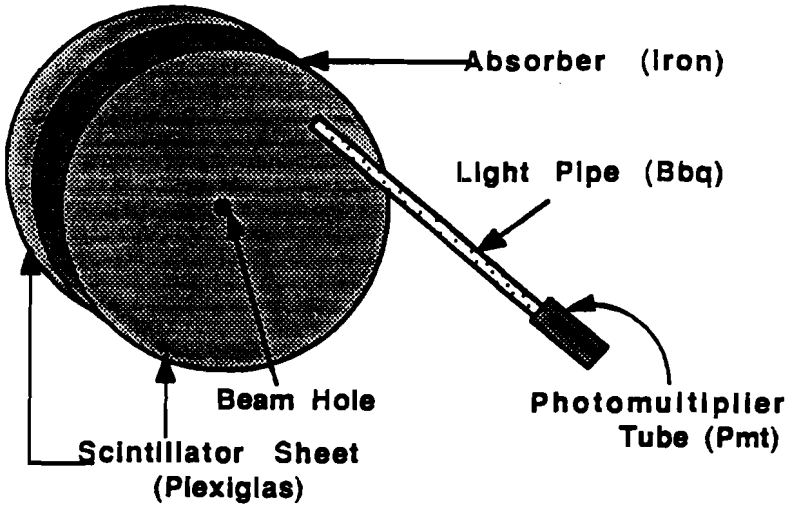

Figure 20: Forward Calorimeter Components

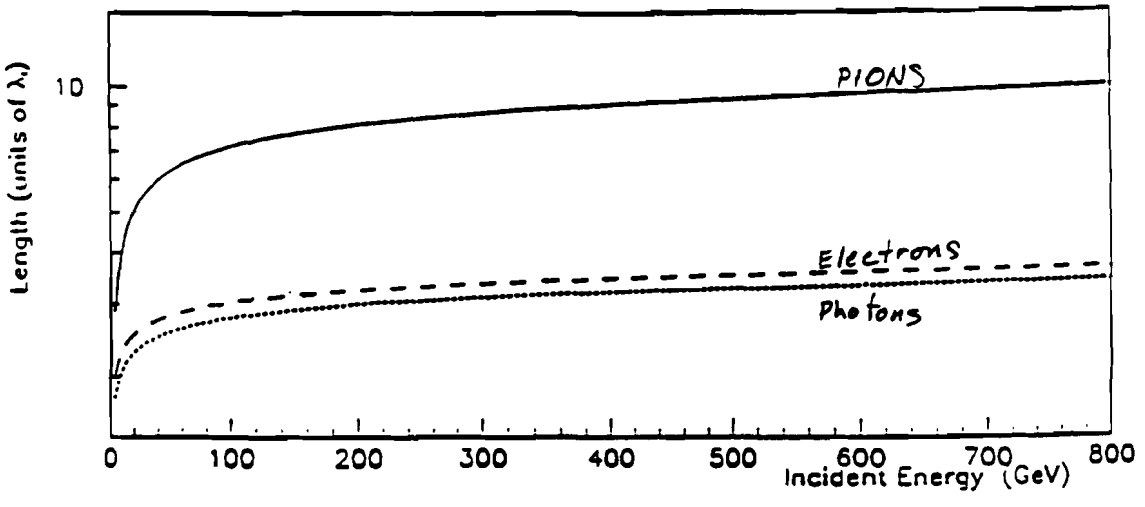

Figure 21: Amount of material required to contain 95% (98%) of the total energy from an incident pion (electron or photon) as a function of the incident energy.

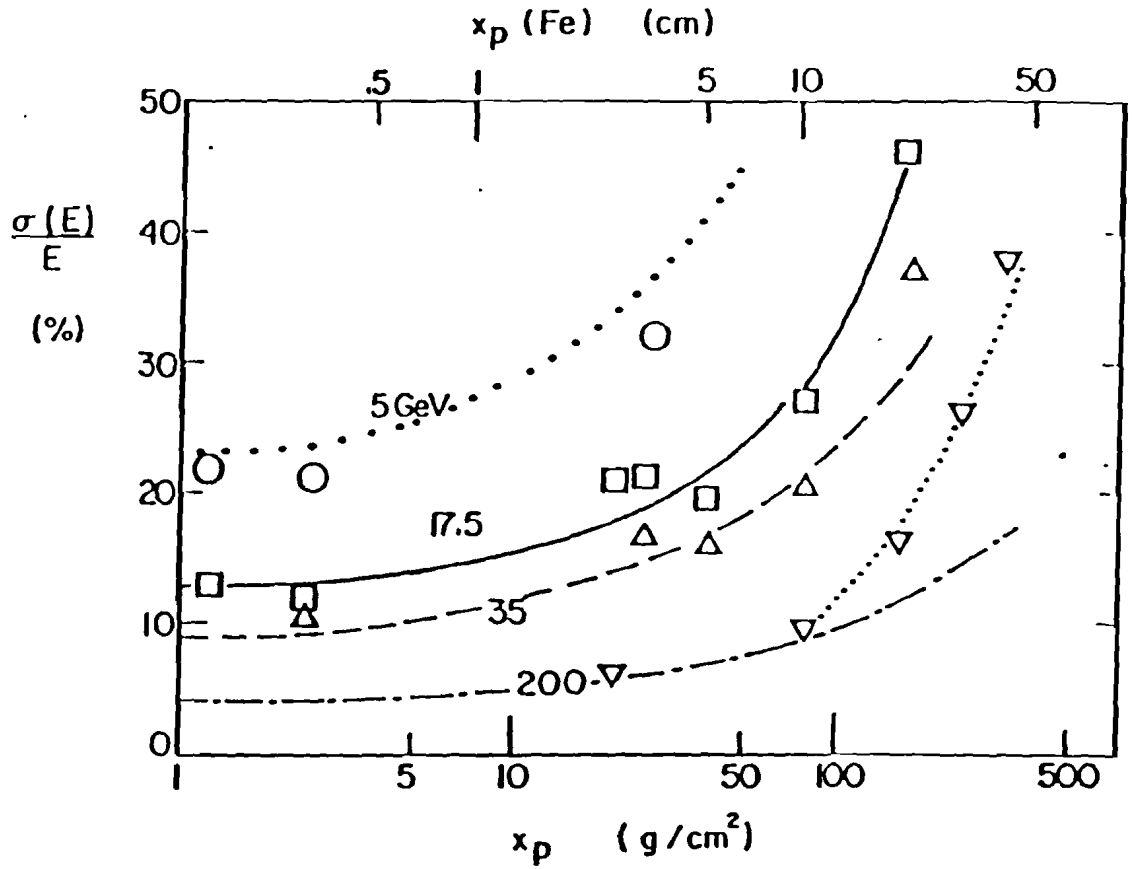

Figure 22: The compilation by Iwata on the thickness dependence of measured hadronic resolutions at 5, 17.5, 35 and 200 GeV compared to some predictions.

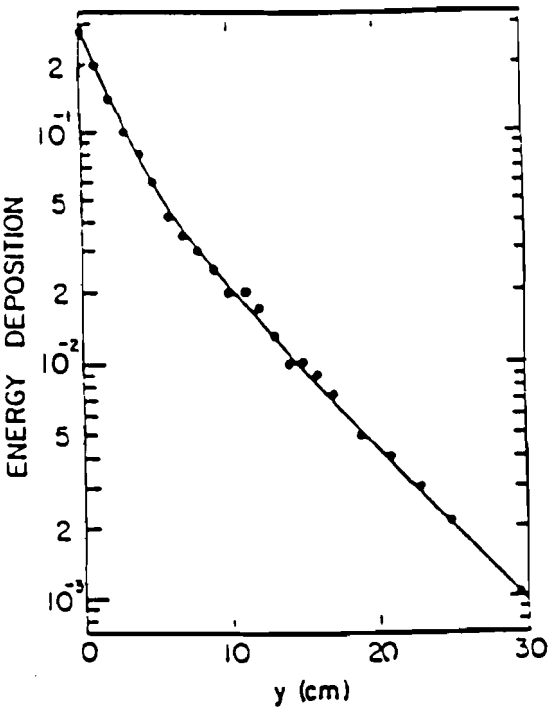

Fig. 23 Lateral distribution of a shower initiated by a 30 GeV anti-proton in the iron calorimeter of the IHEP–IISN–LAPP group. Note the two components of different slope

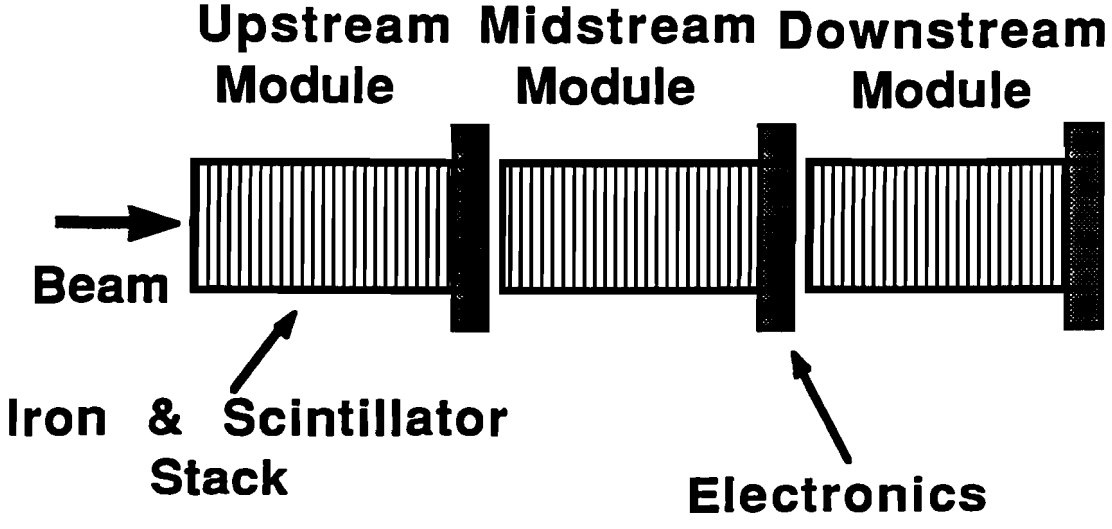

Figure 24: FCAL Placement

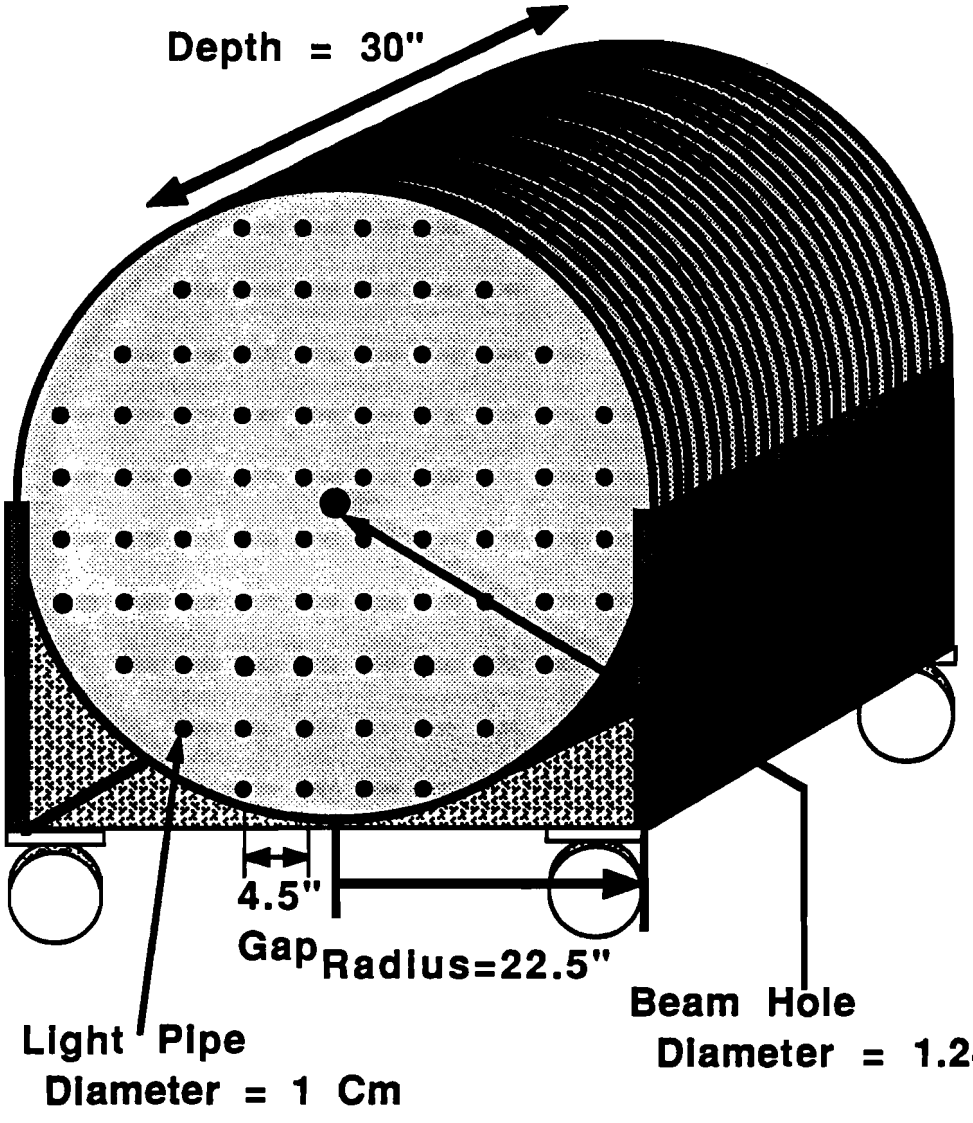

Material	Thickness	# Layers
Iron	0.75"	28, 32
Scintillator	1cm	29, 33

Figure 25: FCAL Module

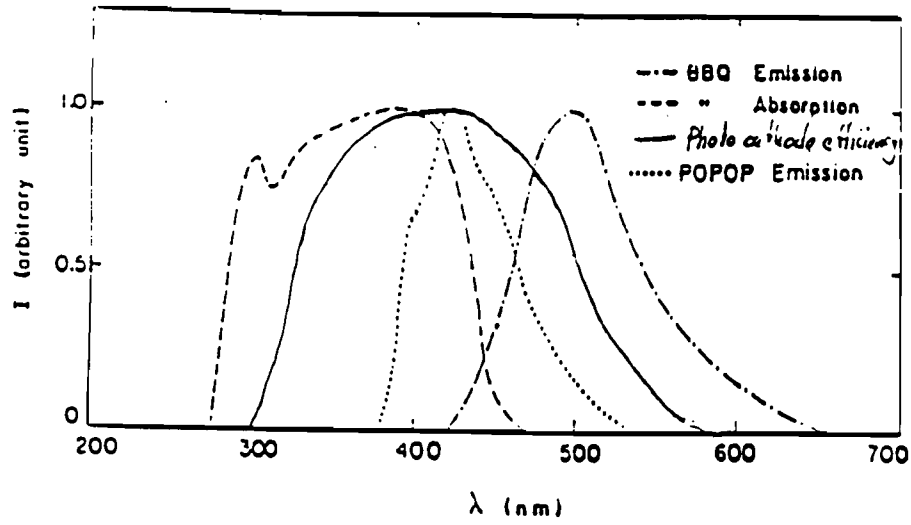

Figure 26: Absorption and Emission Spectra of BBQ.

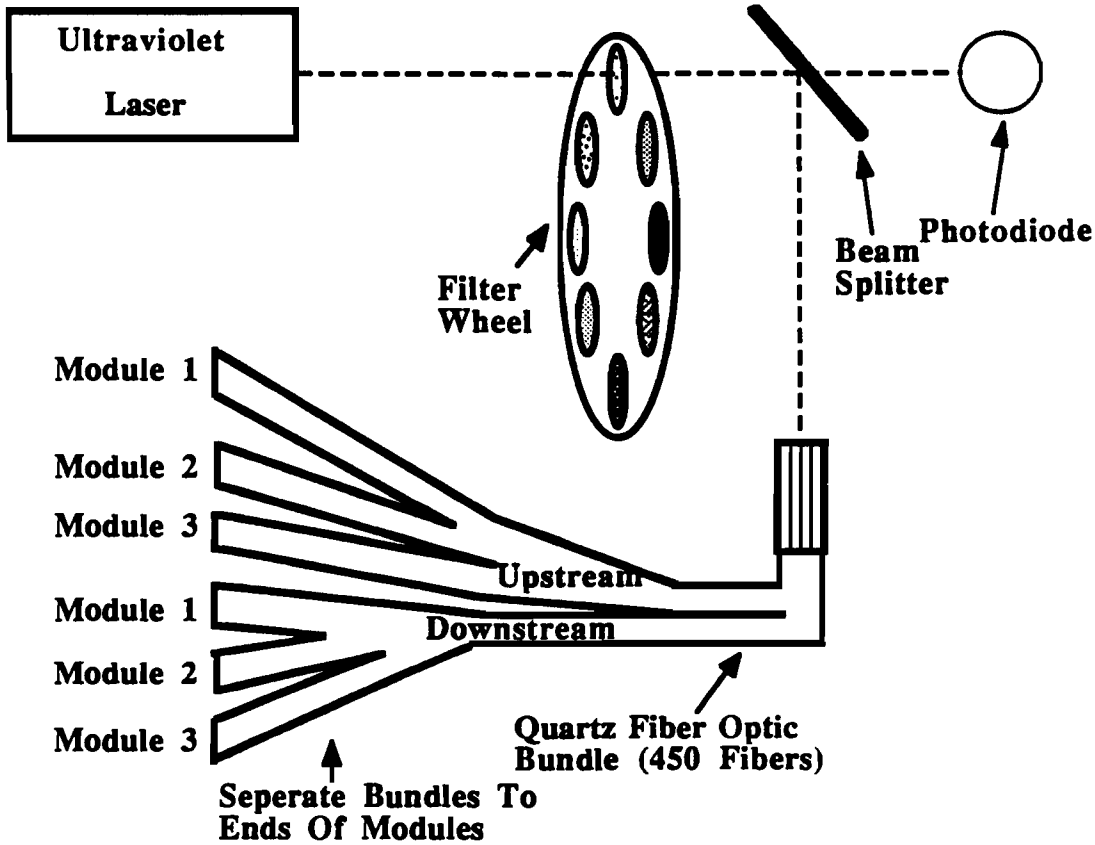

Figure 27: Laser Calibration System

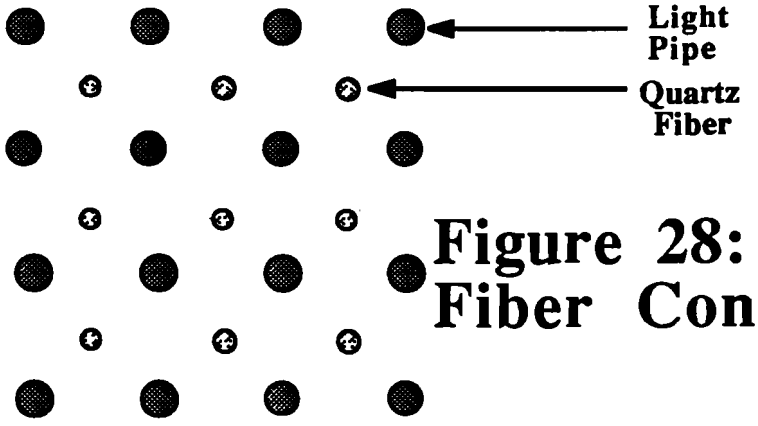

Figure 28: Light Fiber Configuration

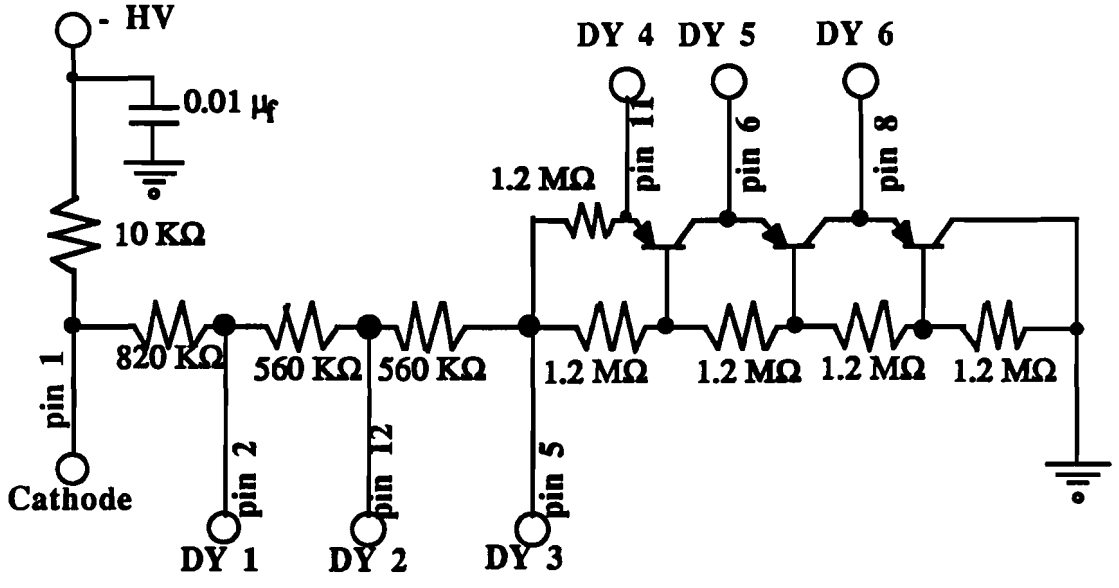

Figure 29: PMT High Voltage Circuit

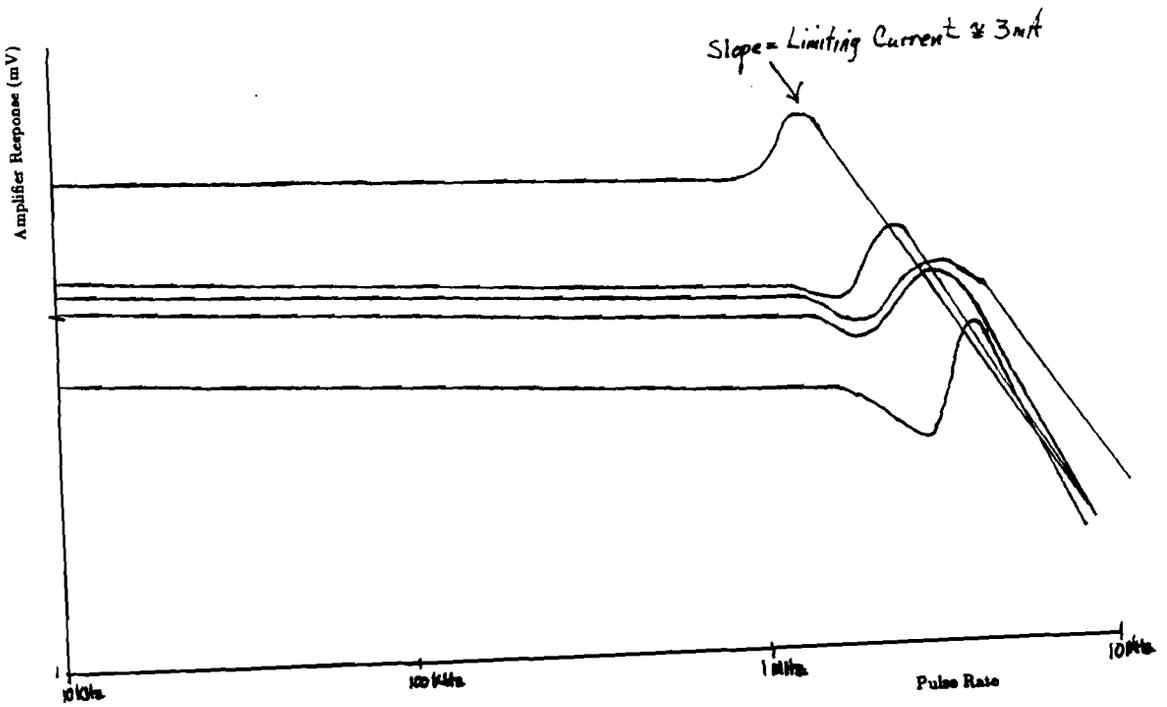

Figure 30: Amplifier response VS Pulse Rate for a standard input pulse.

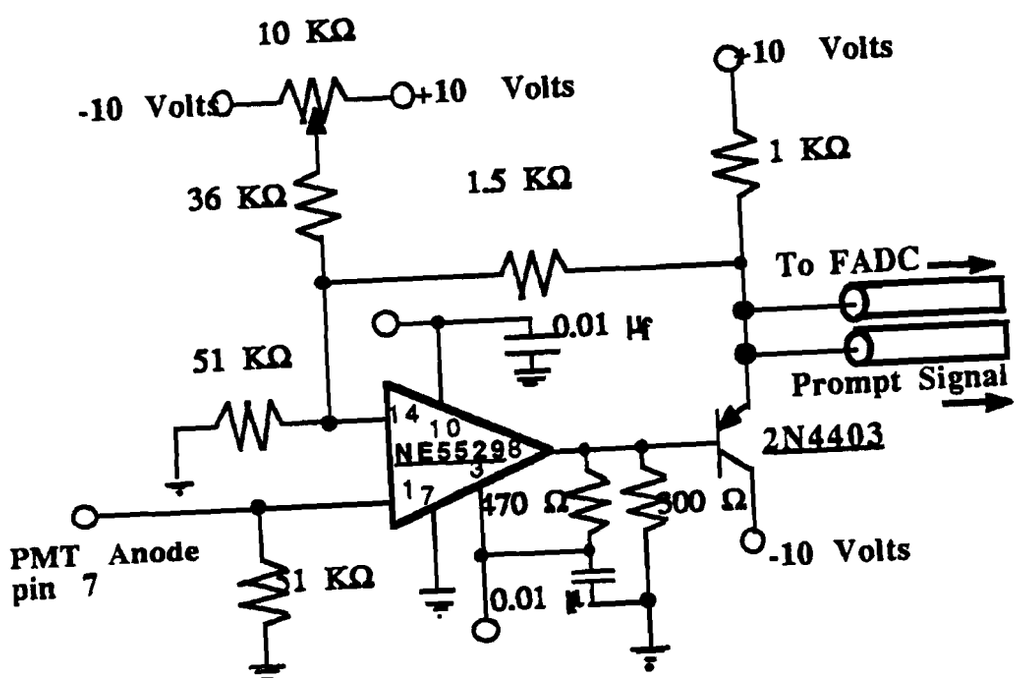

Figure 31: PMT Amplifier Circuit

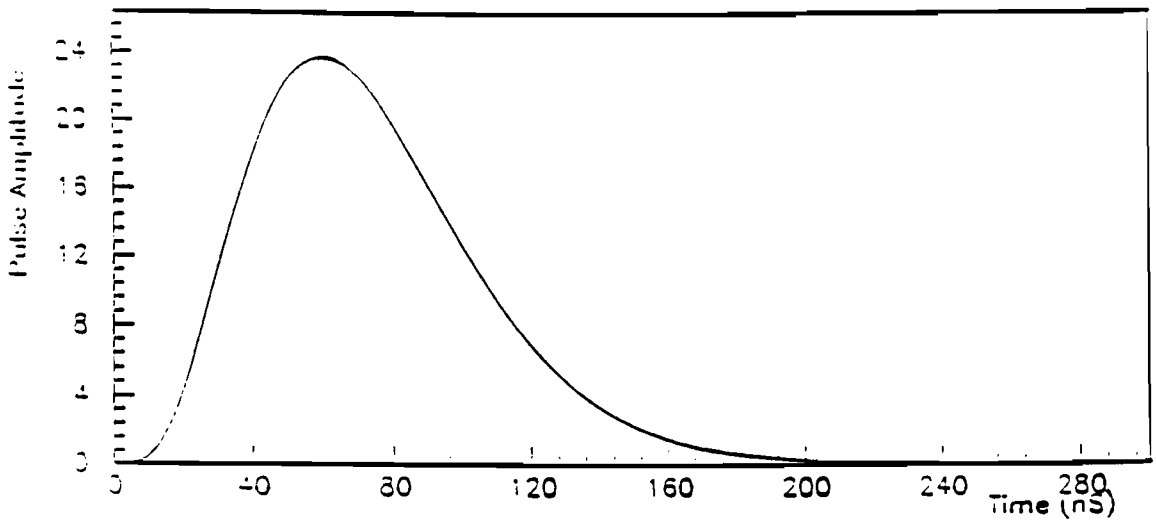

Figure 32: Typical Pulse Profile from PMT Amplifier.

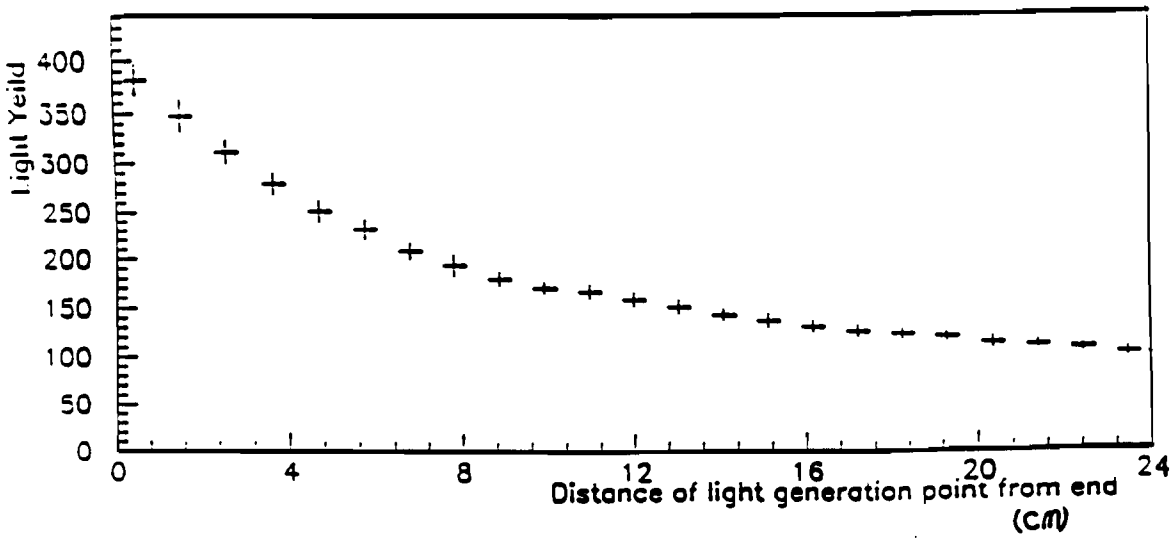

Figure 33: Light Attenuation in a typical BBQ rod.

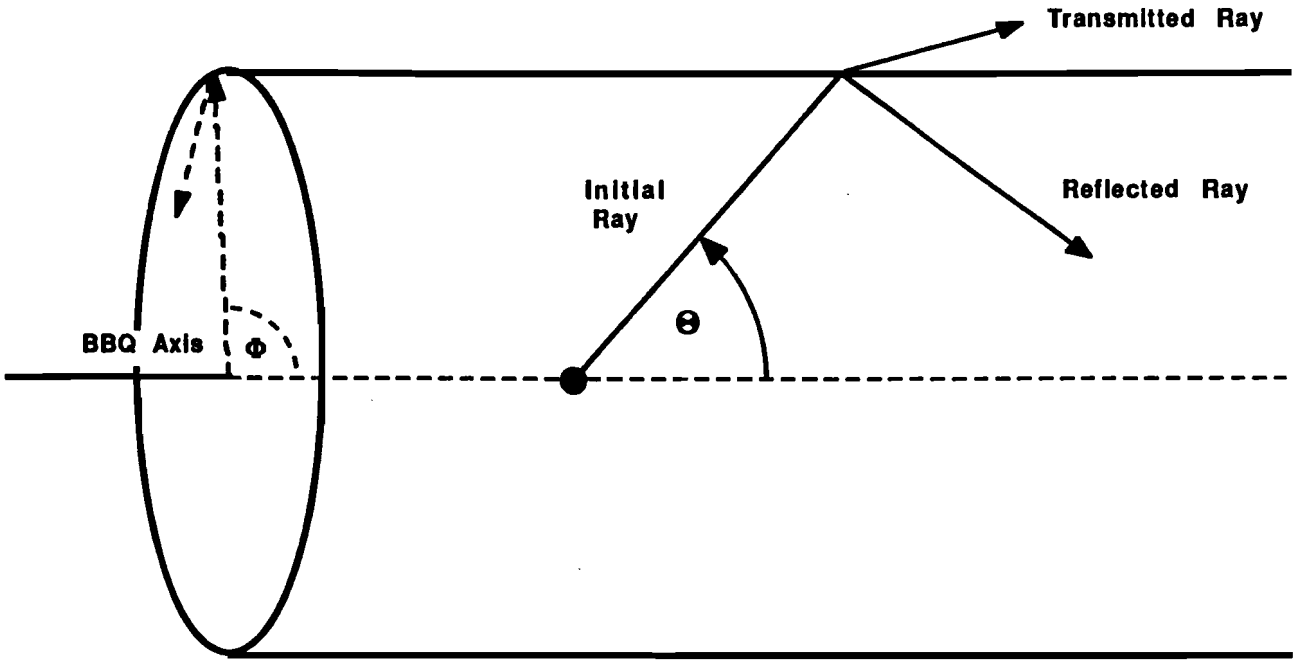

Figure 34: Light Path in BBQ

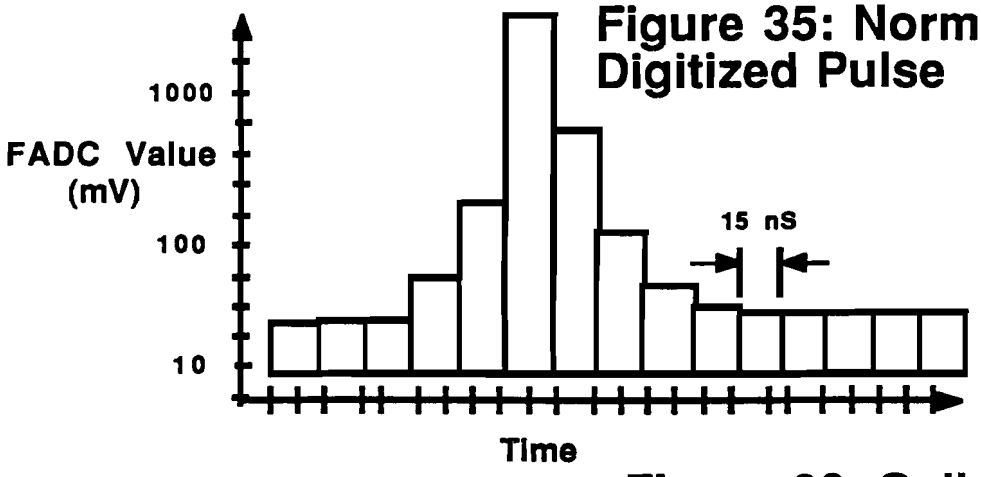

Figure 35: Normal Digitized Pulse

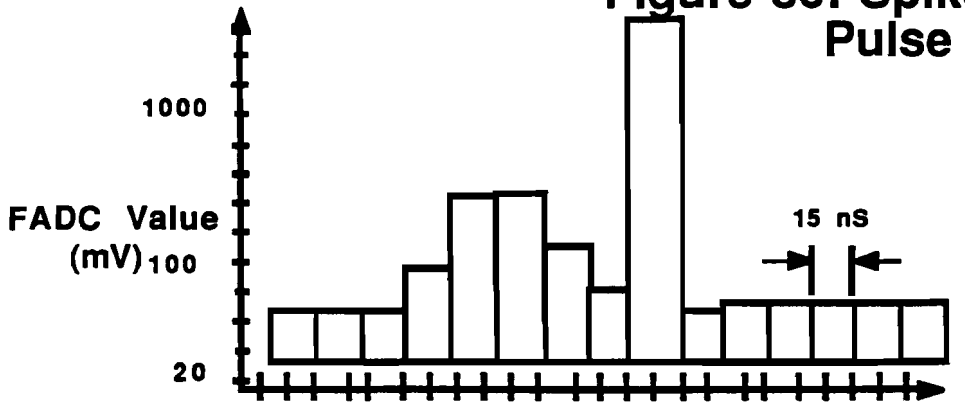

Figure 36: Spike Pulse

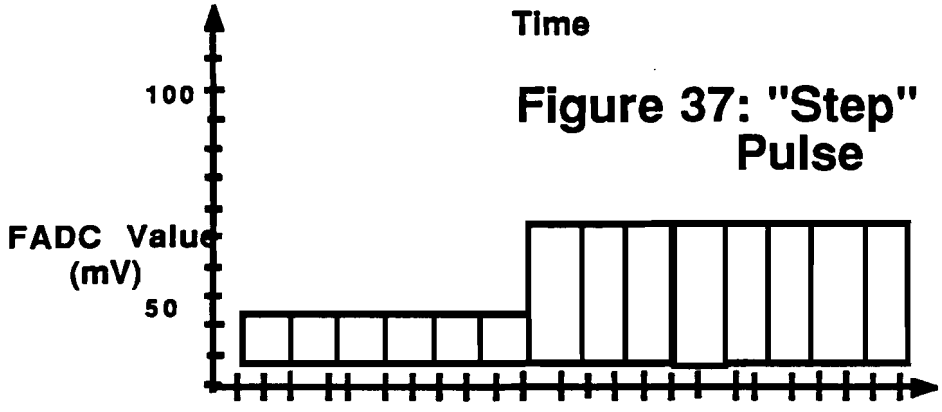

Figure 37: "Step" Pulse

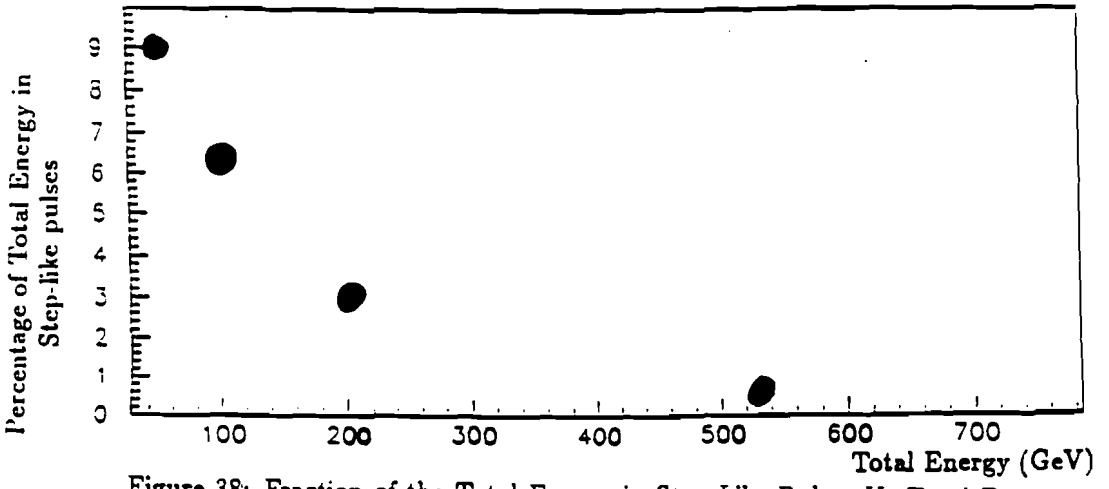

Figure 38: Fraction of the Total Energy in Step-Like Pulses Vs Total Energy.

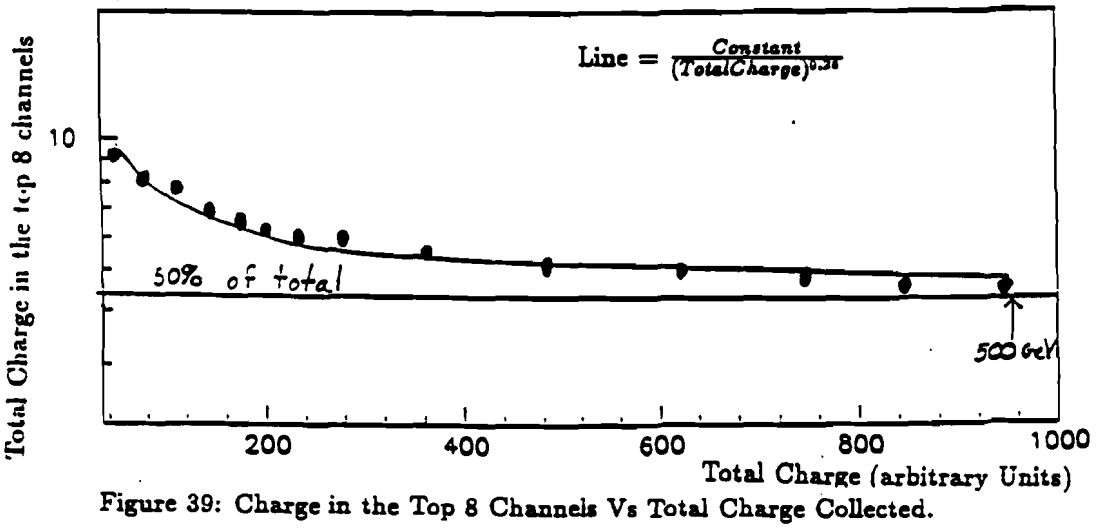

Figure 39: Charge in the Top 8 Channels Vs Total Charge Collected.

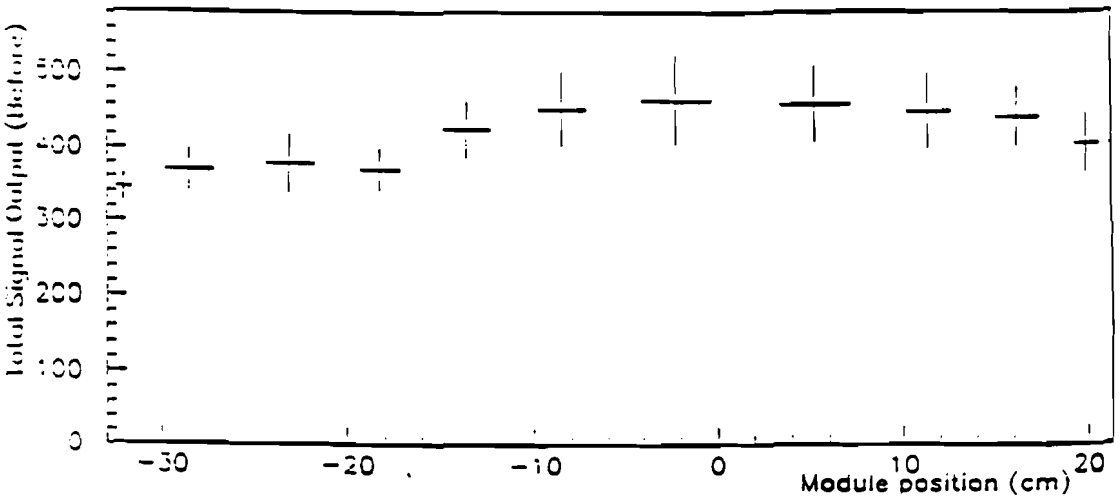

Figure 40: Total Raw Reconstructed Signal from the FCAL VS Position.

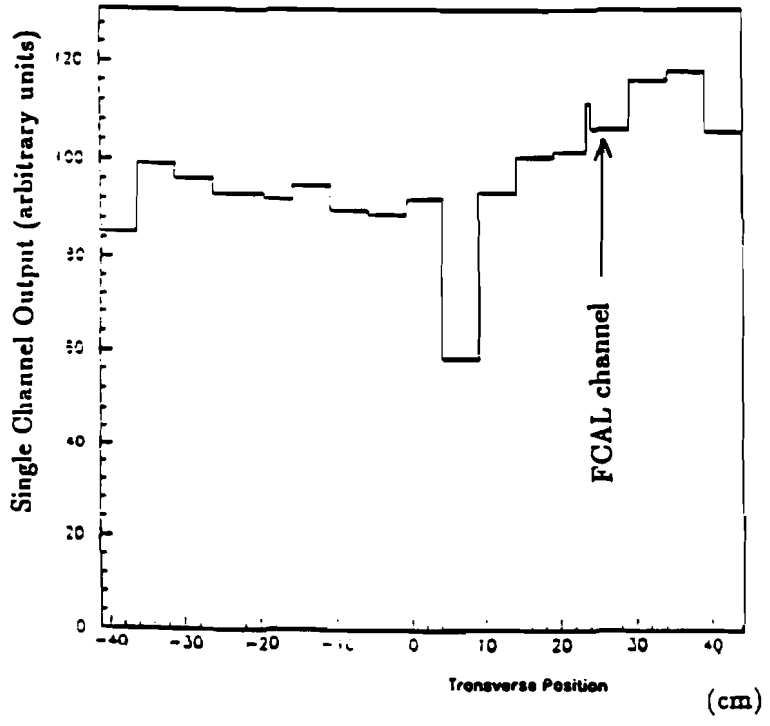

Figure 41: Total Signal from a single FCAL channel VS Beam Position.

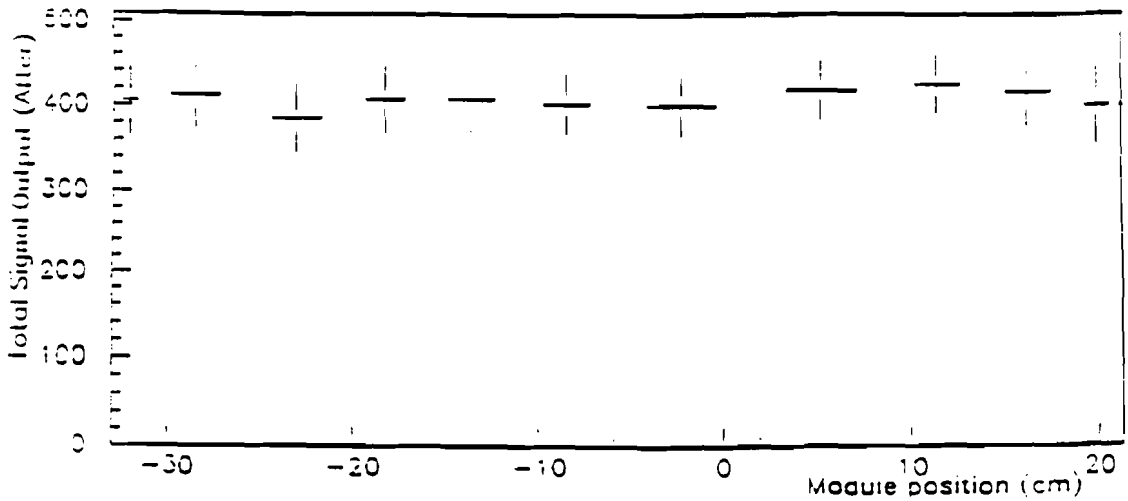

Figure 42: Total Raw Reconstructed Signal from the FCAL after adjusting PMT gains VS Position.

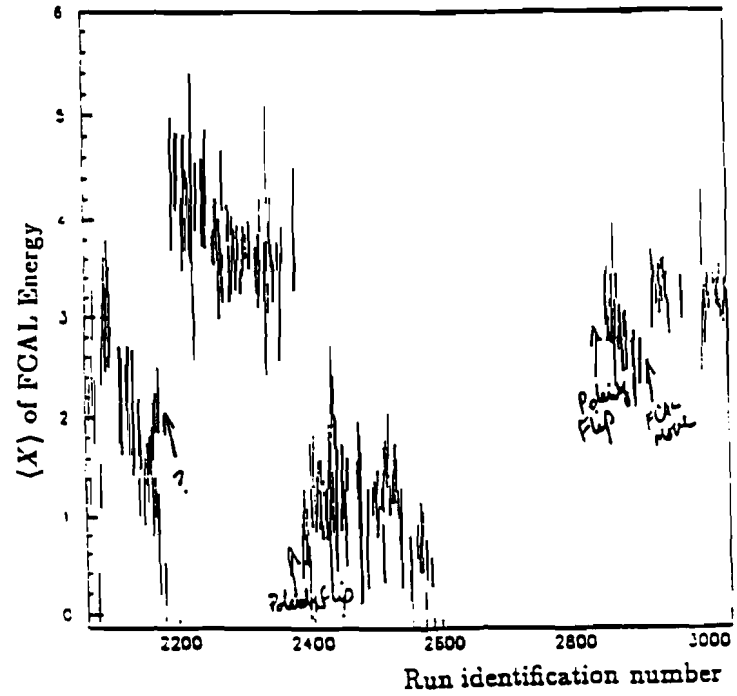

Figure 43: Run Dependence of Reconstructed Beam Position.

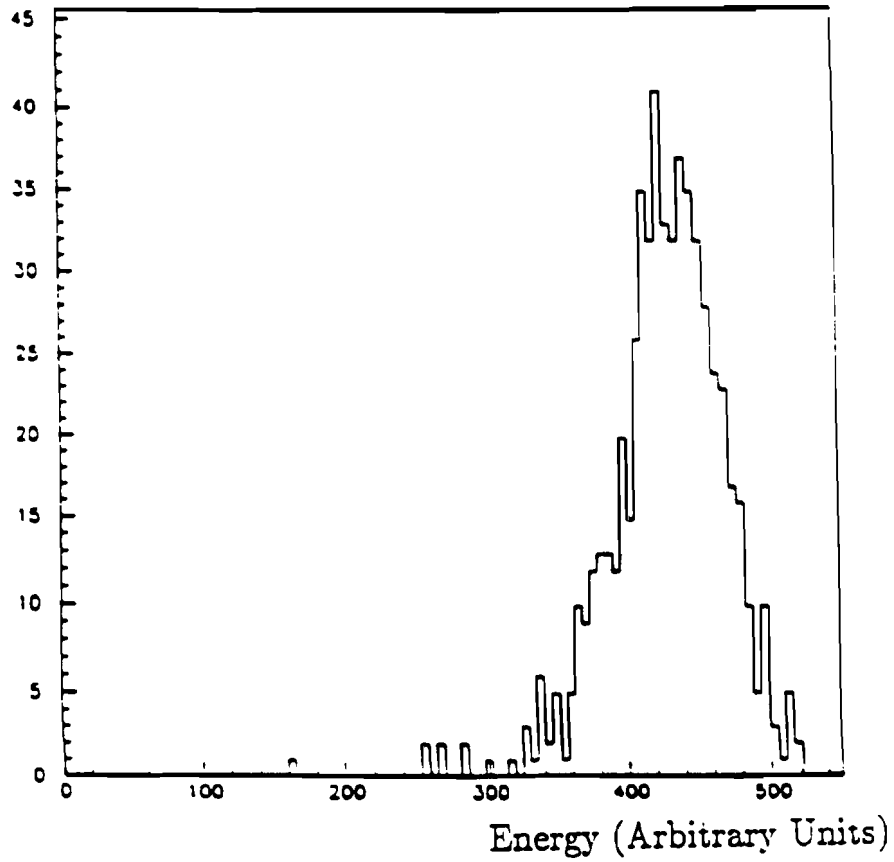

Figure 44: : Monte Carlo reconstructed raw energy spectrum in the FCAL for 530 GeV Pions starting in the target.

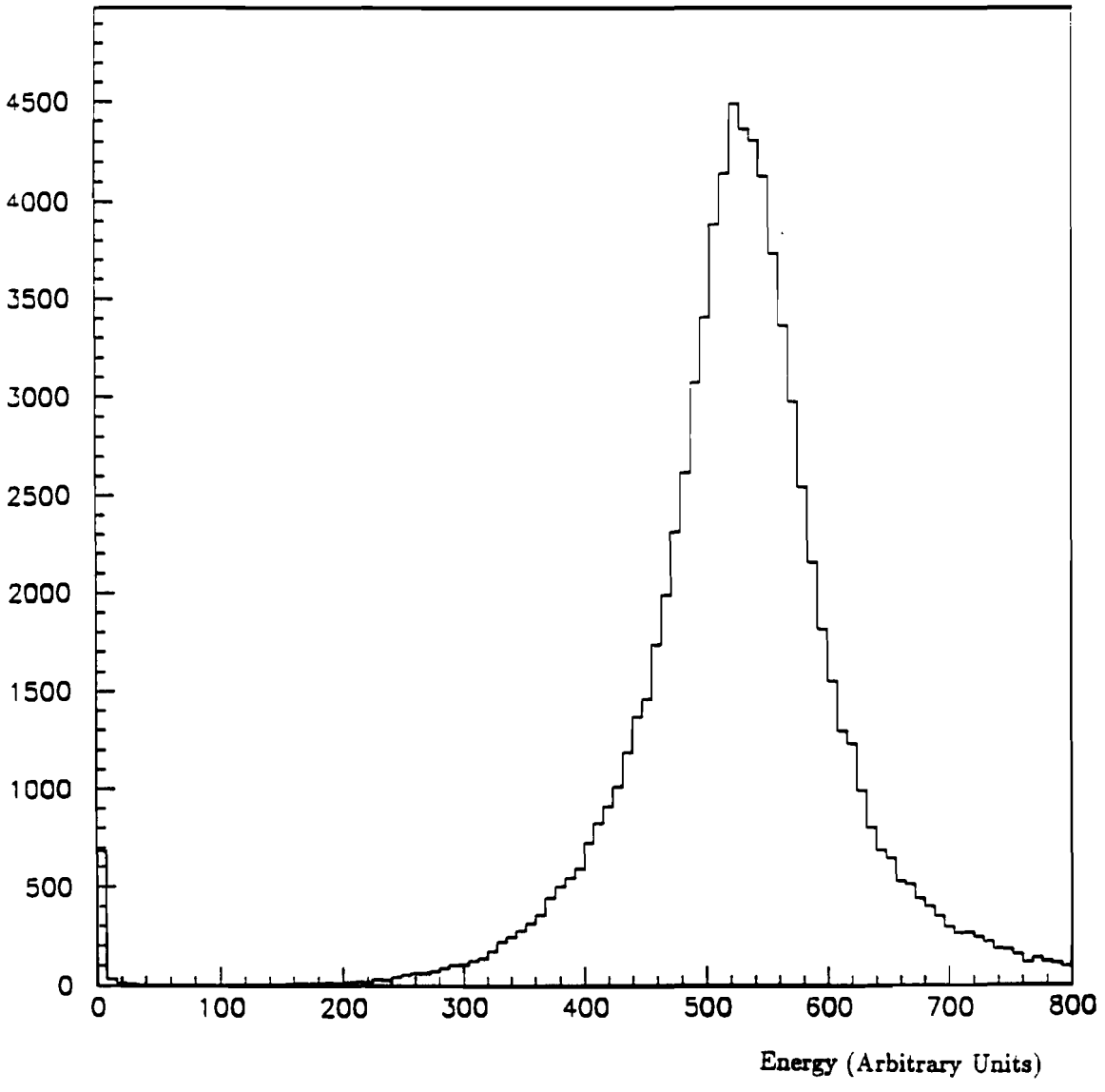

Figure 45: Reconstructed Raw Energy Spectrum of 530 GeV Calibration Beam.

Figure 46: ISAJET (MINBIAS) energy spectrum used to determine the FCAL calibration curve.

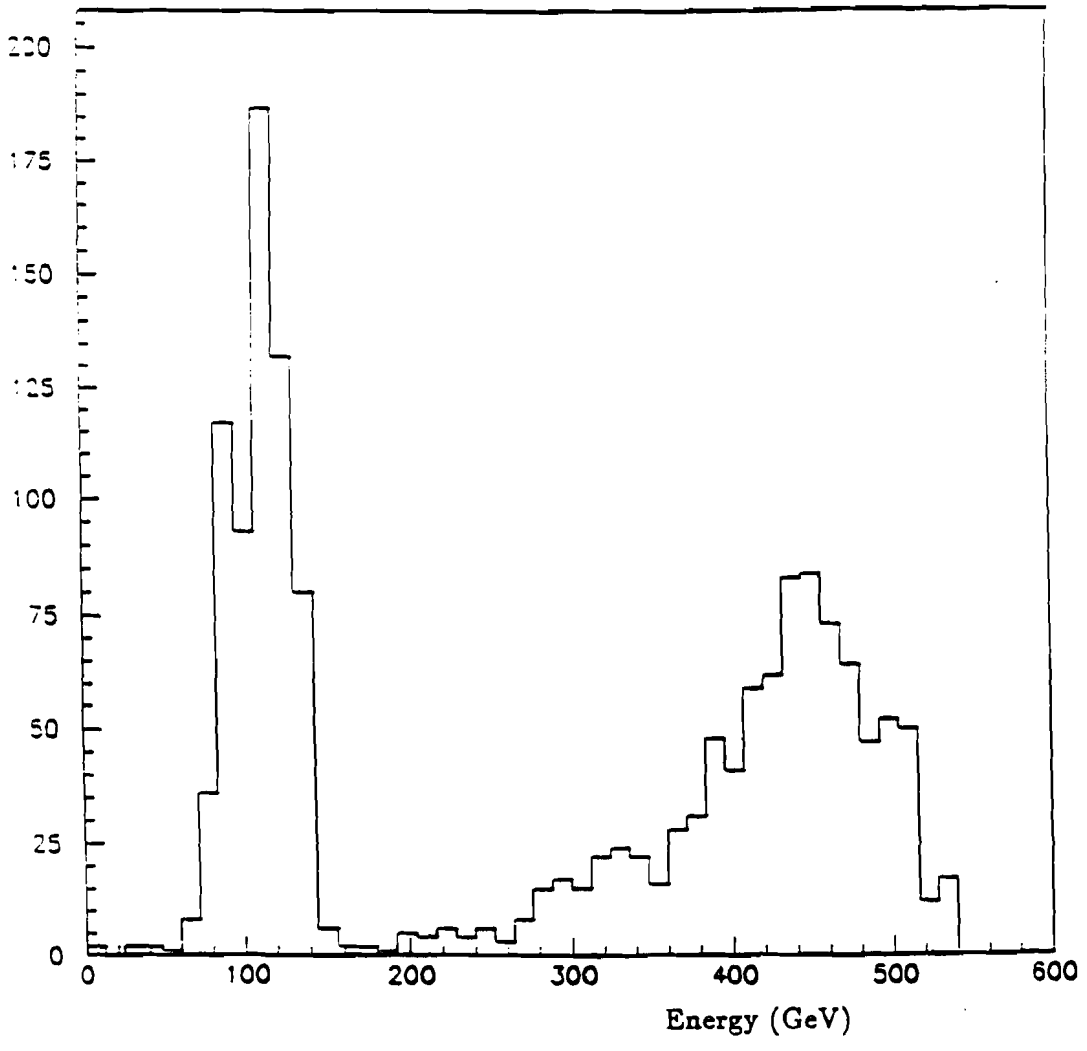

Figure 47: Fractional Error VS Reconstructed Energy (Before calibration).

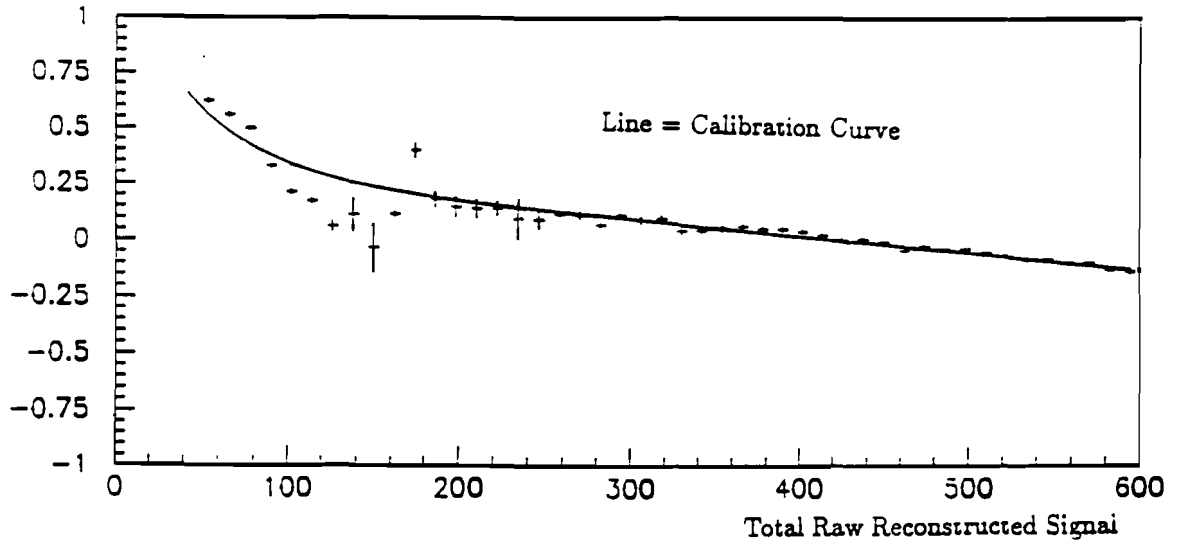

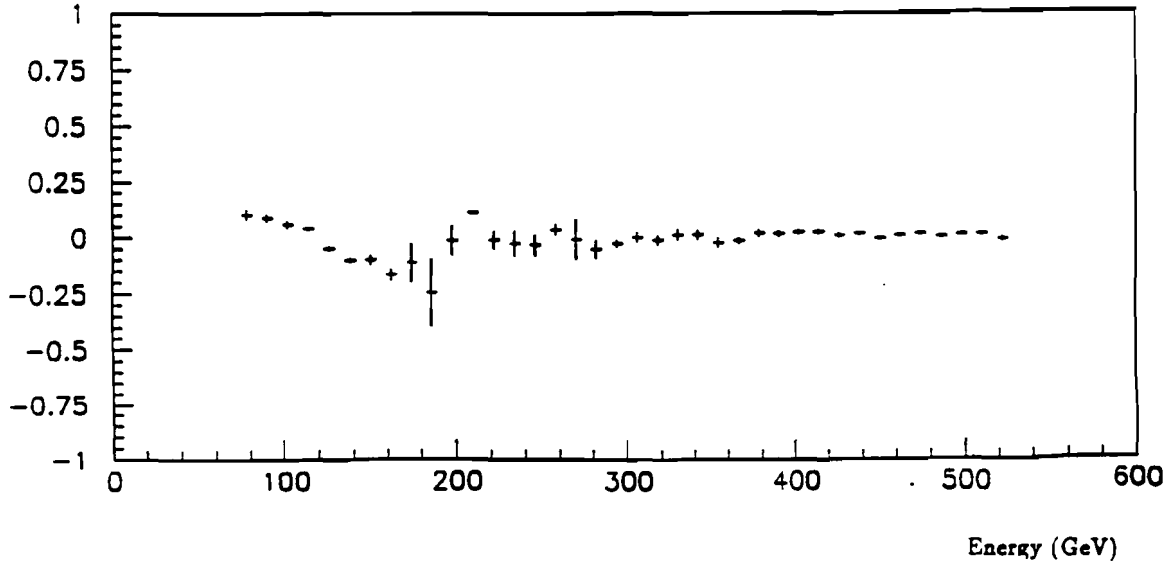

Figure 48: Fractional Error VS Reconstructed Energy (After calibration).

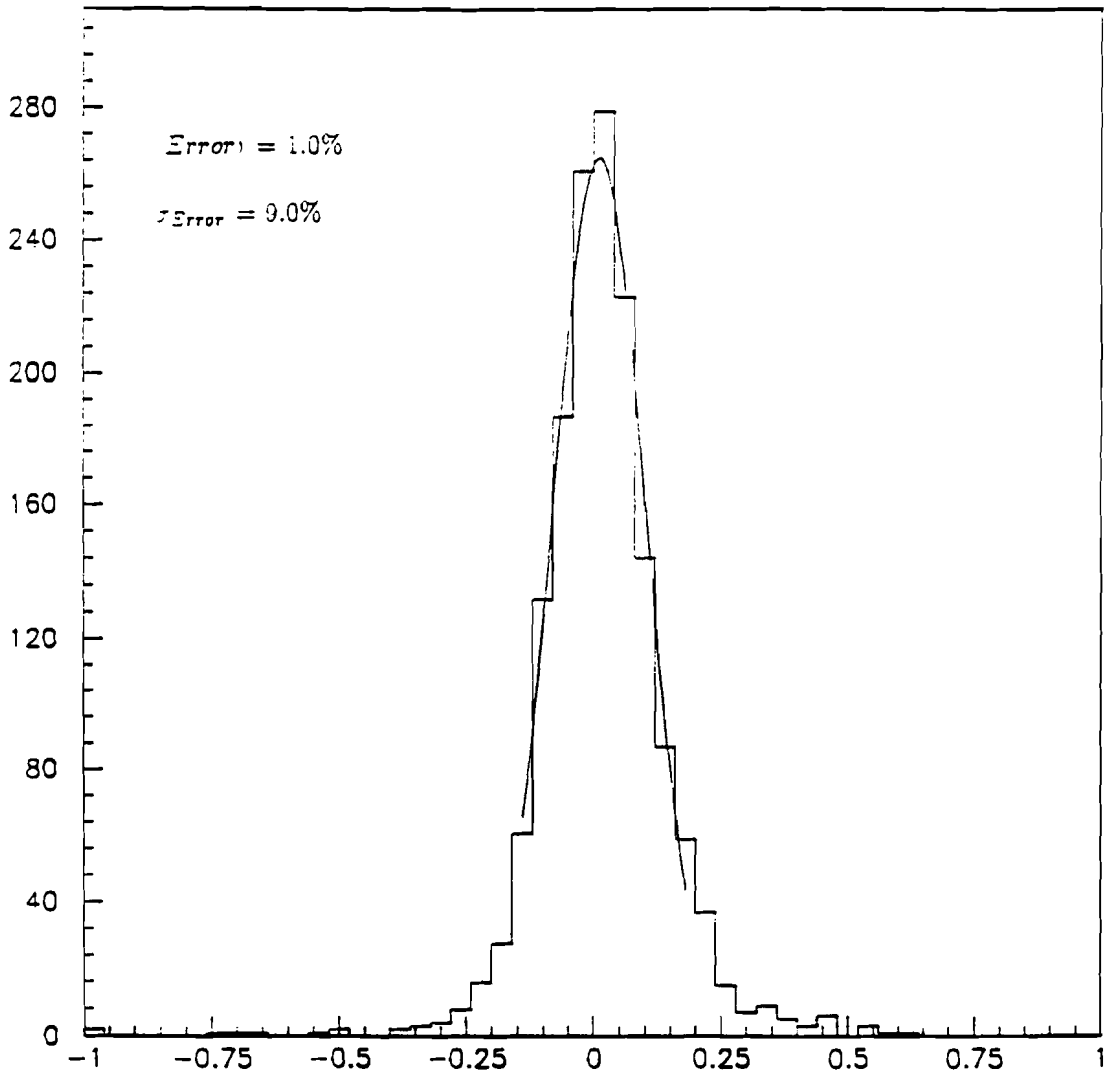

Figure 49: Fractional Error (After calibration).

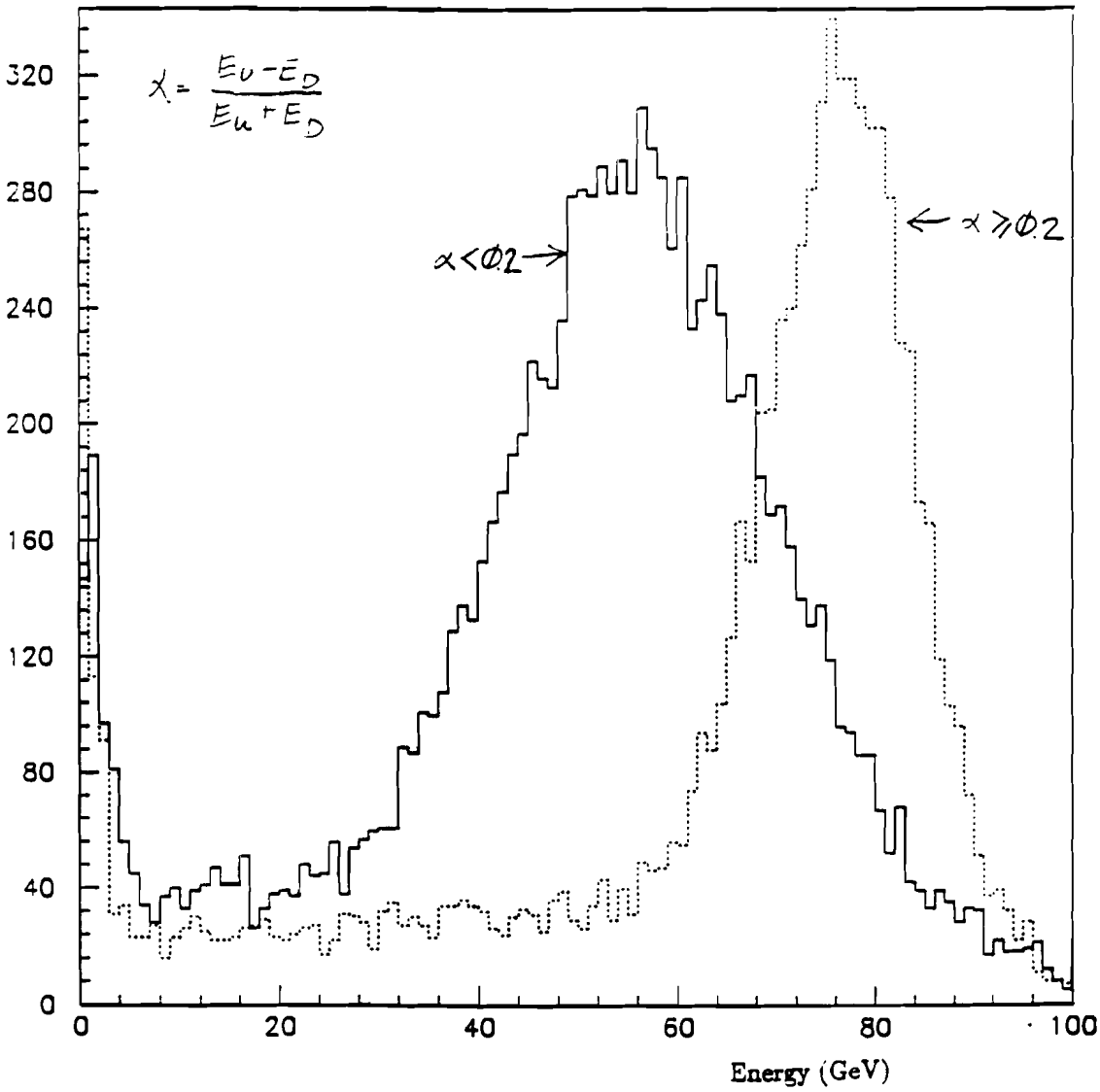

Figure 50A: Reconstructed Energy Spectrum of 50 GeV Calibration Beam.

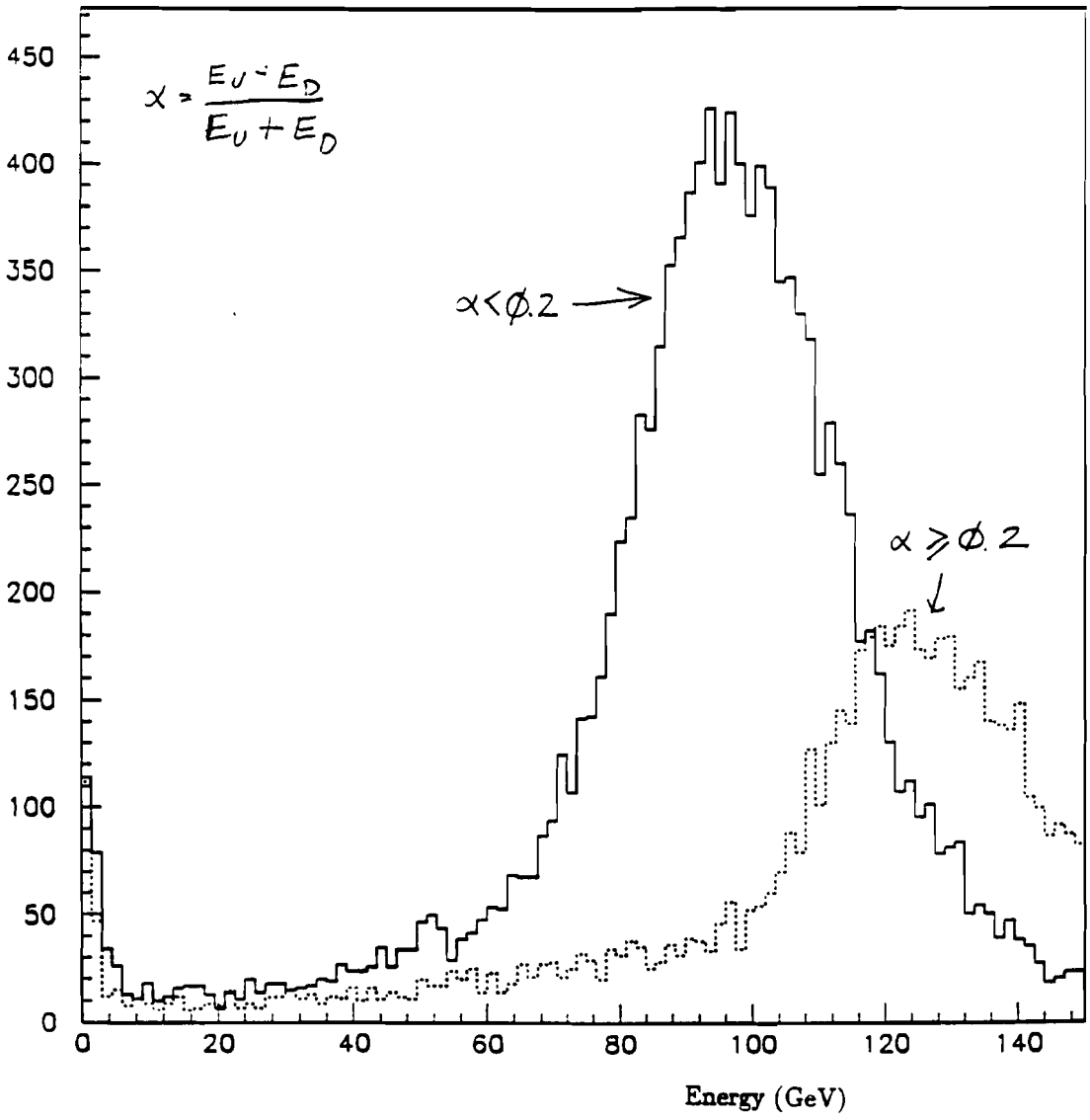

Figure 50B: Reconstructed Energy Spectrum of 100 GeV Calibration Beam.

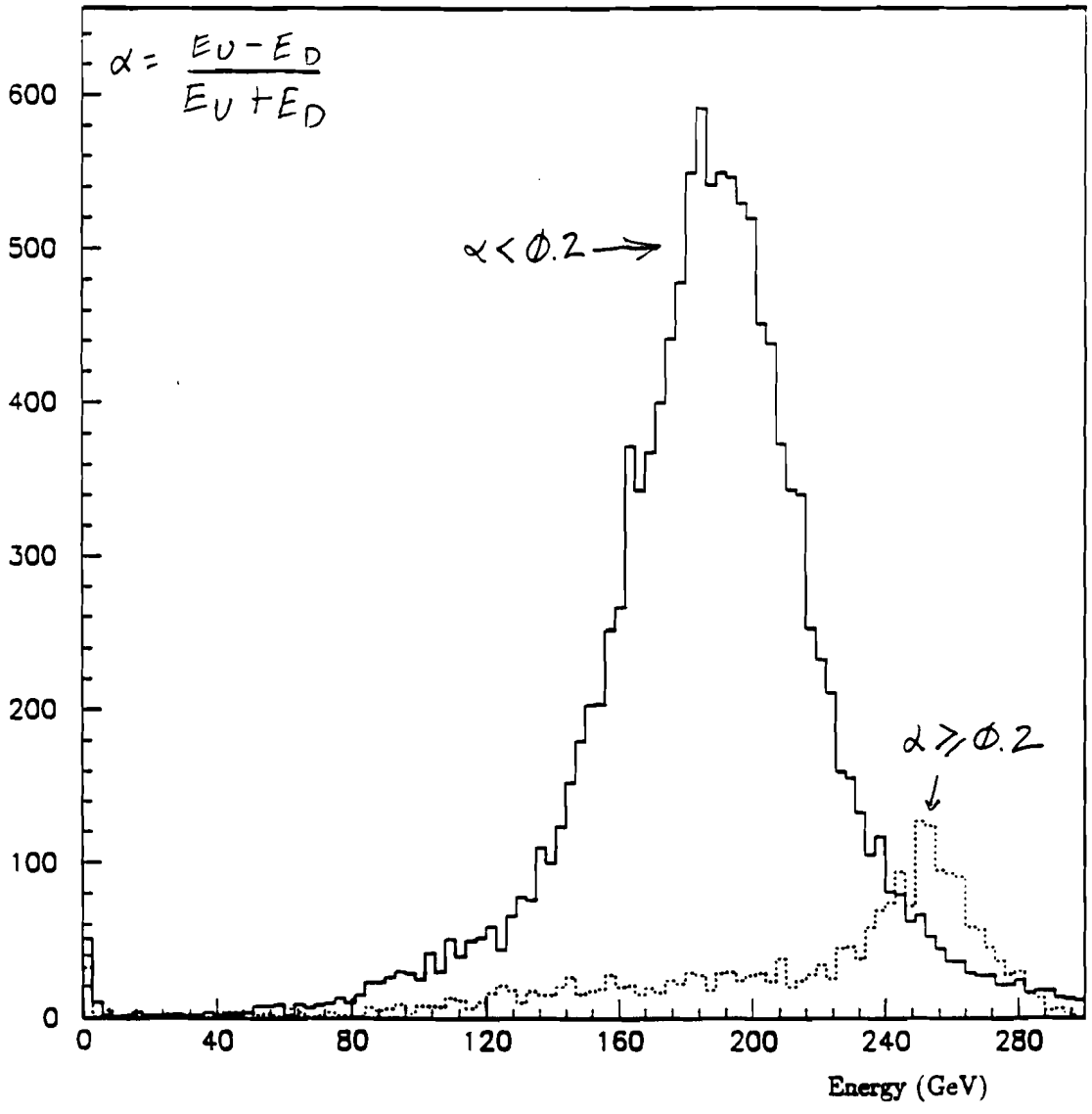

Figure 50C: Reconstructed Energy Spectrum of 200 GeV Calibration Beam.

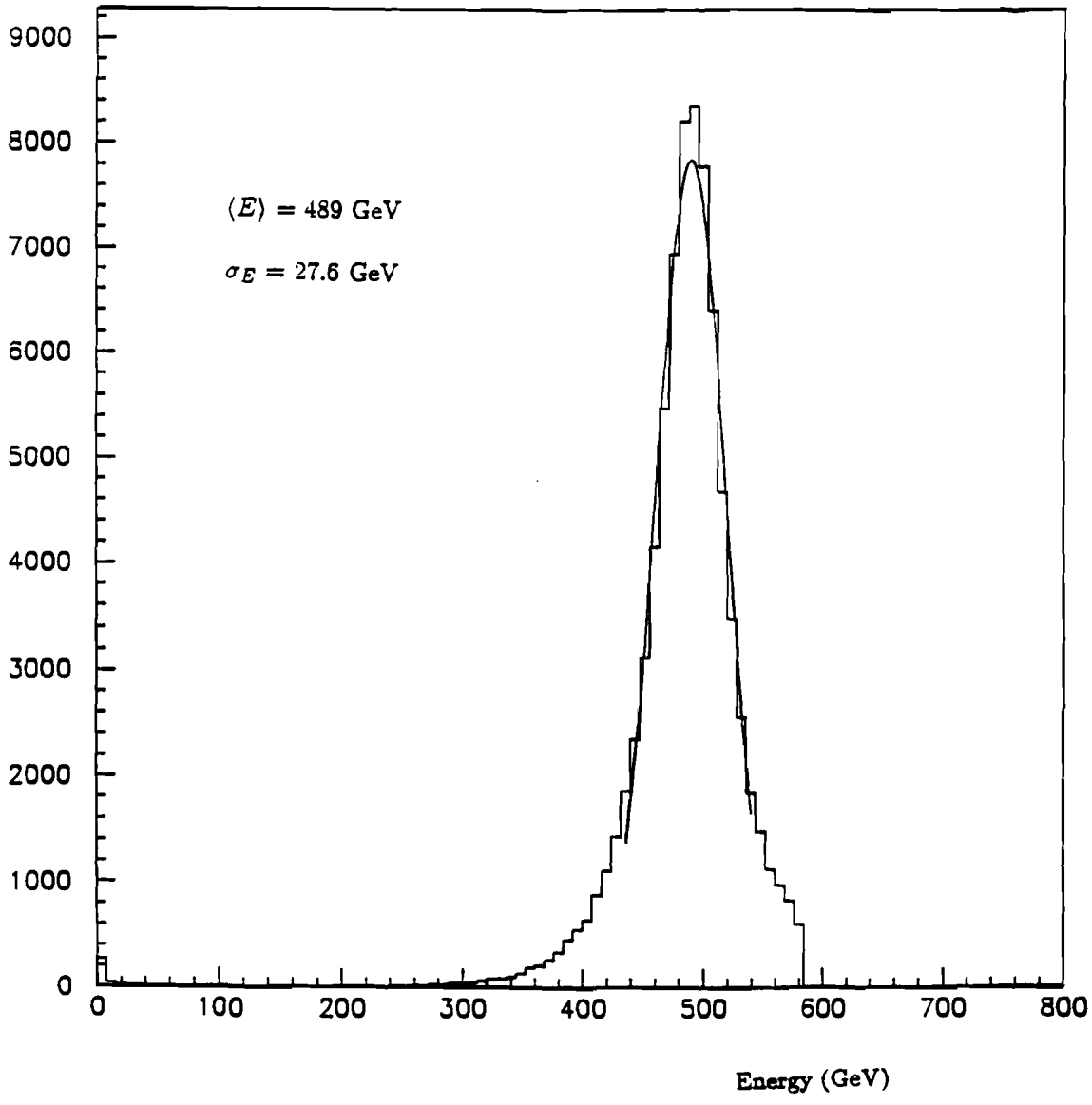

Figure 50D: Reconstructed Energy Spectrum of 530 GeV Calibration Beam.

Figure 51: Longitudinal Asymmetry Vs Raw Energy Signal for the 50 GeV Calibration Data.

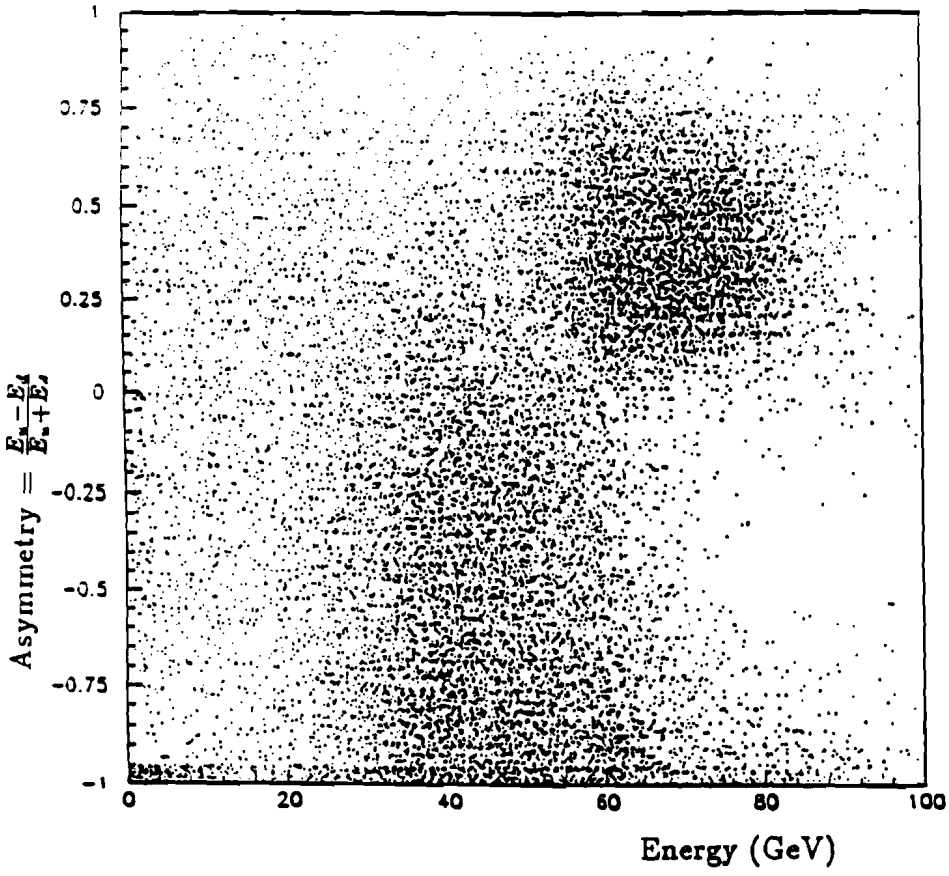

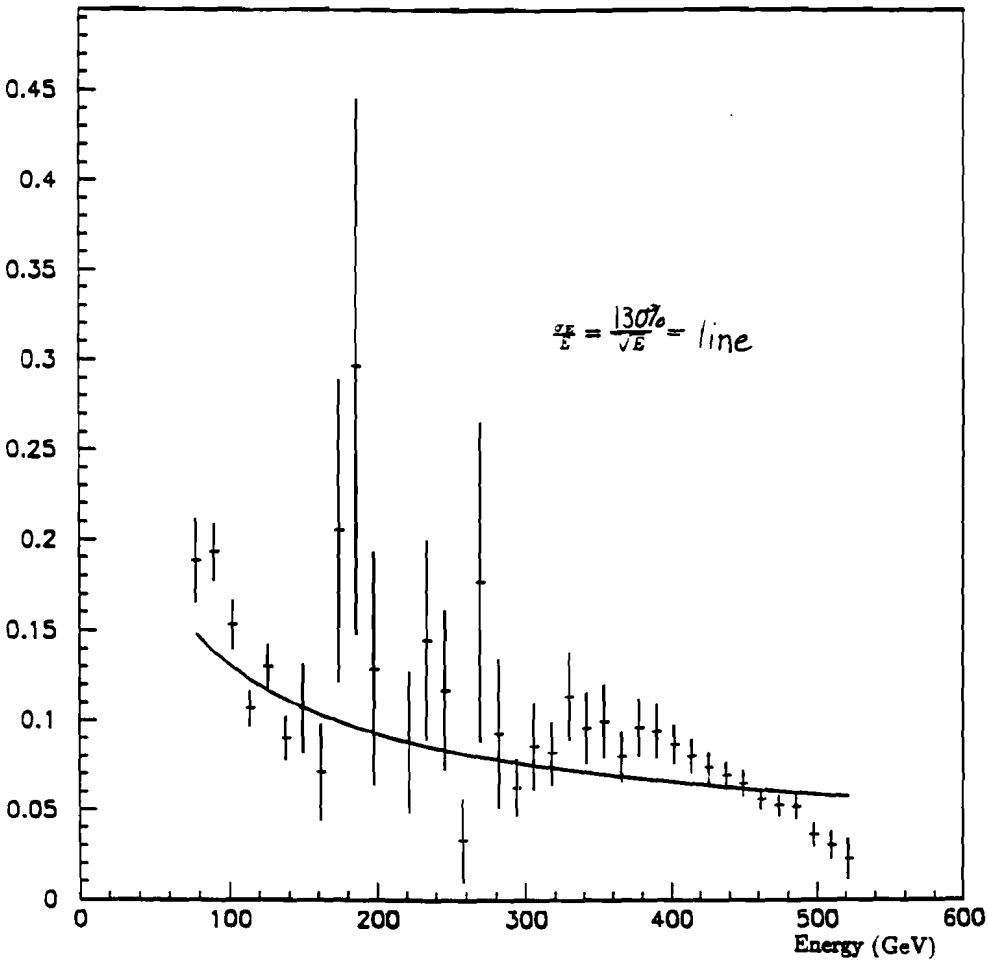

Figure 52: Energy Spread Vs Energy for monte carlo calibration data.

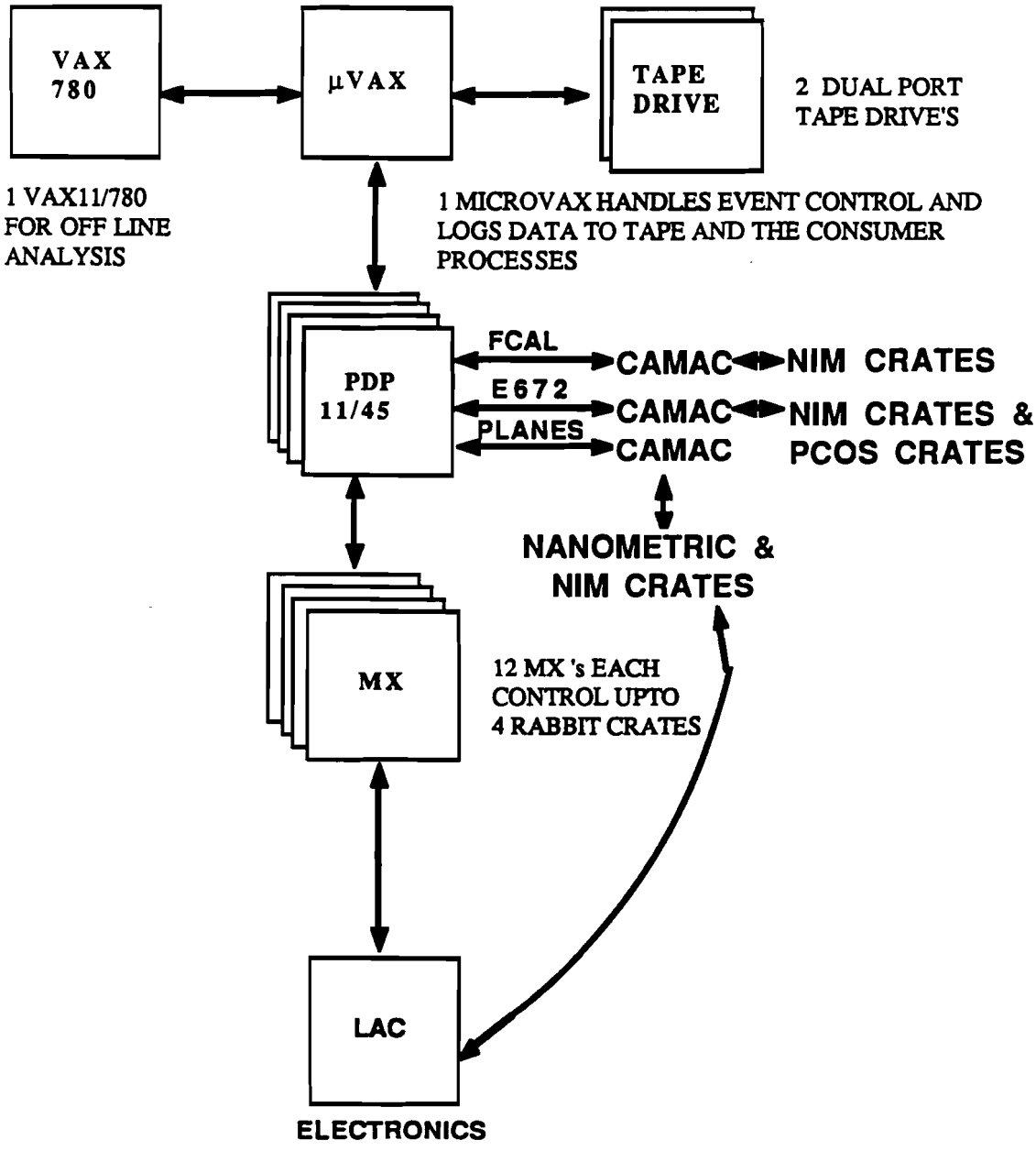

Figure 53: Data Acquisition Hardware

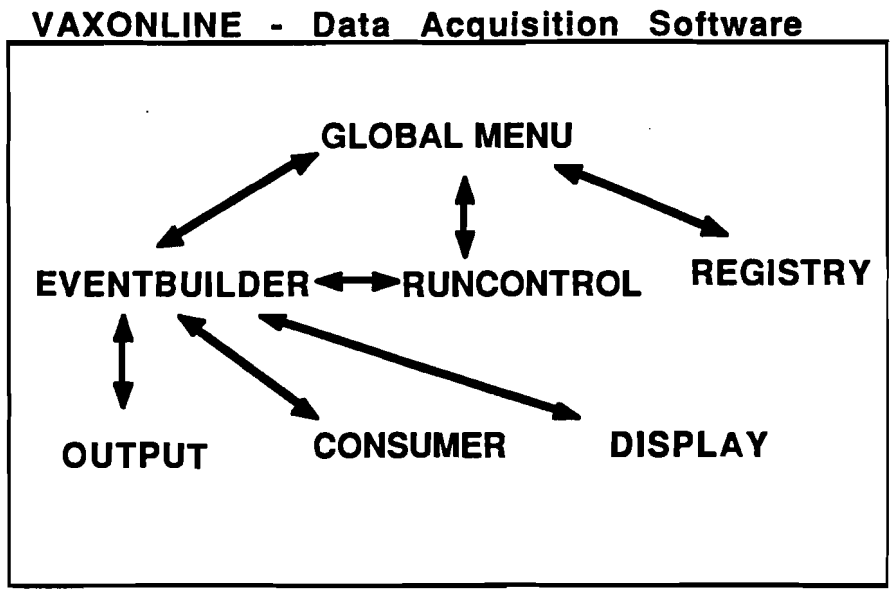

CERNLIB - Library of statistical and graphical routines

DI3000 - Commercial high resolution, color graphics routines

EPICS - Beamline and monitoring utility

GEANT - Monte Carlo library of routines

MAGIC - Main code for data analysis

MCE706 - Numerical model of experiment (see GEANT)

MENCOM - Menu creation routines

PATCHY - Code development and management utility

ZEBRA - Dynamic memory manager

(Note: Almost all code was written in the FORTRAN programming language)

Figure 54: Data Acquisition Software

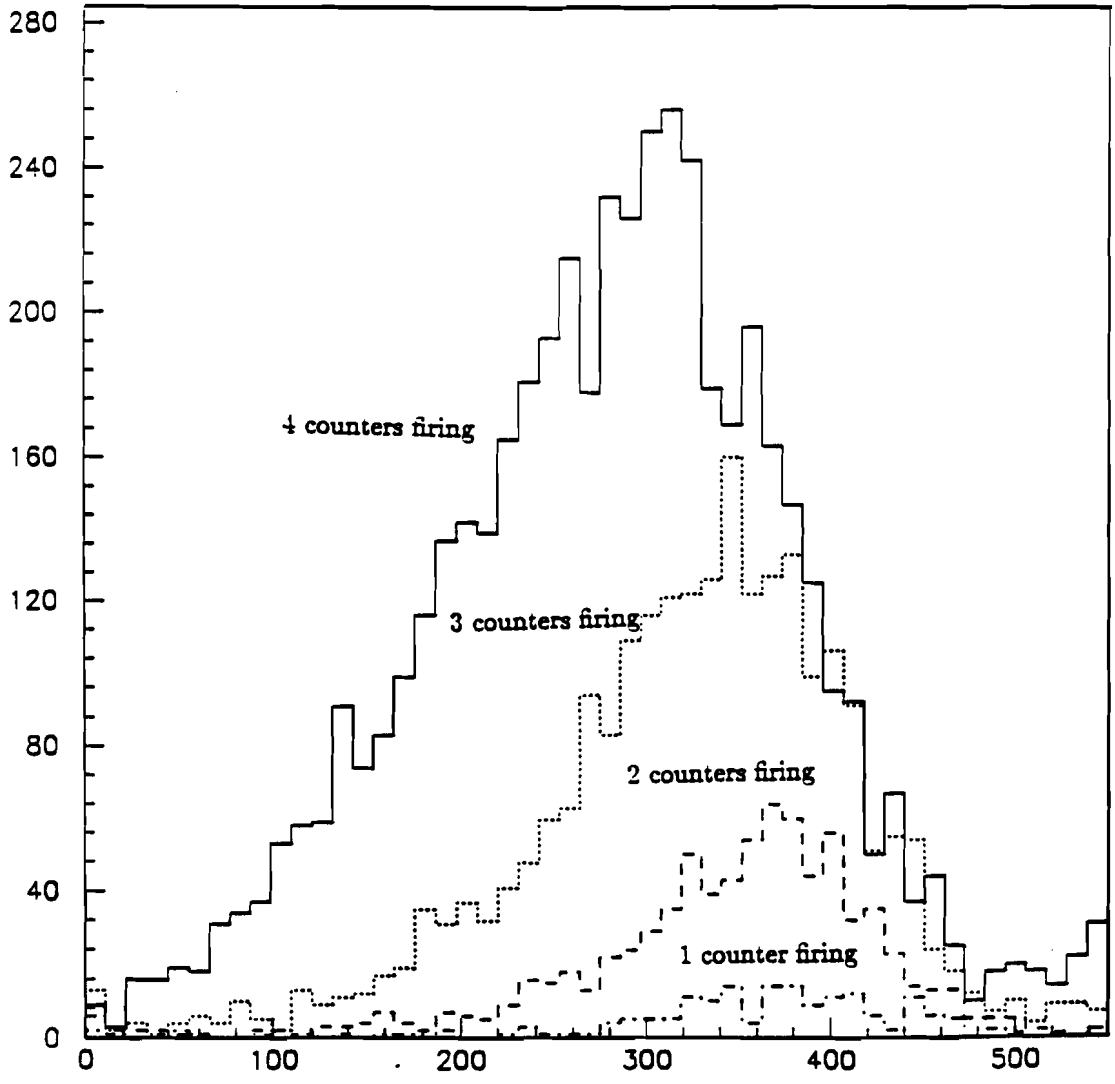

Figure 55A: Forward Energy Spectra for Protons.

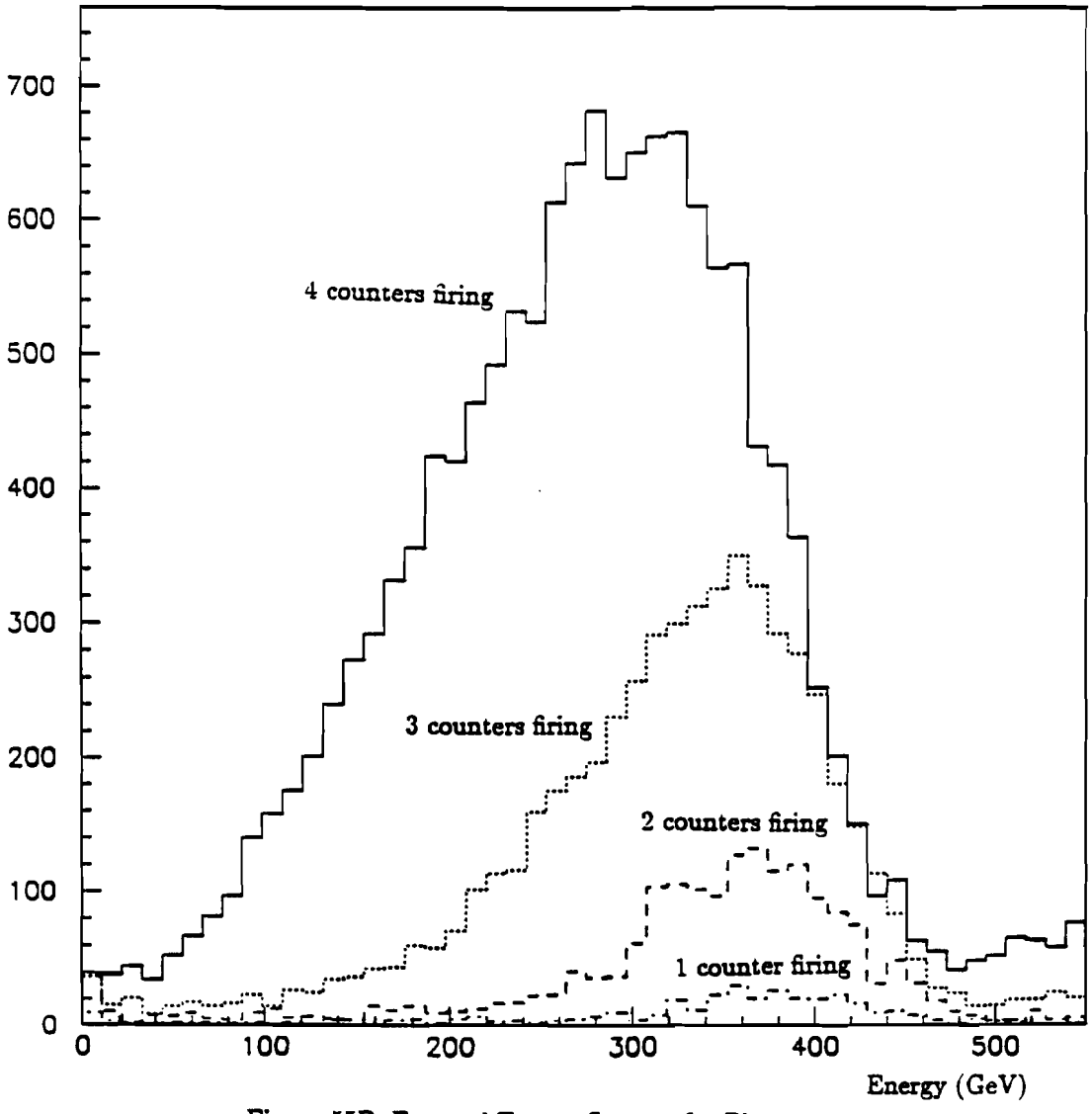

Figure 55B: Forward Energy Spectra for Pions.

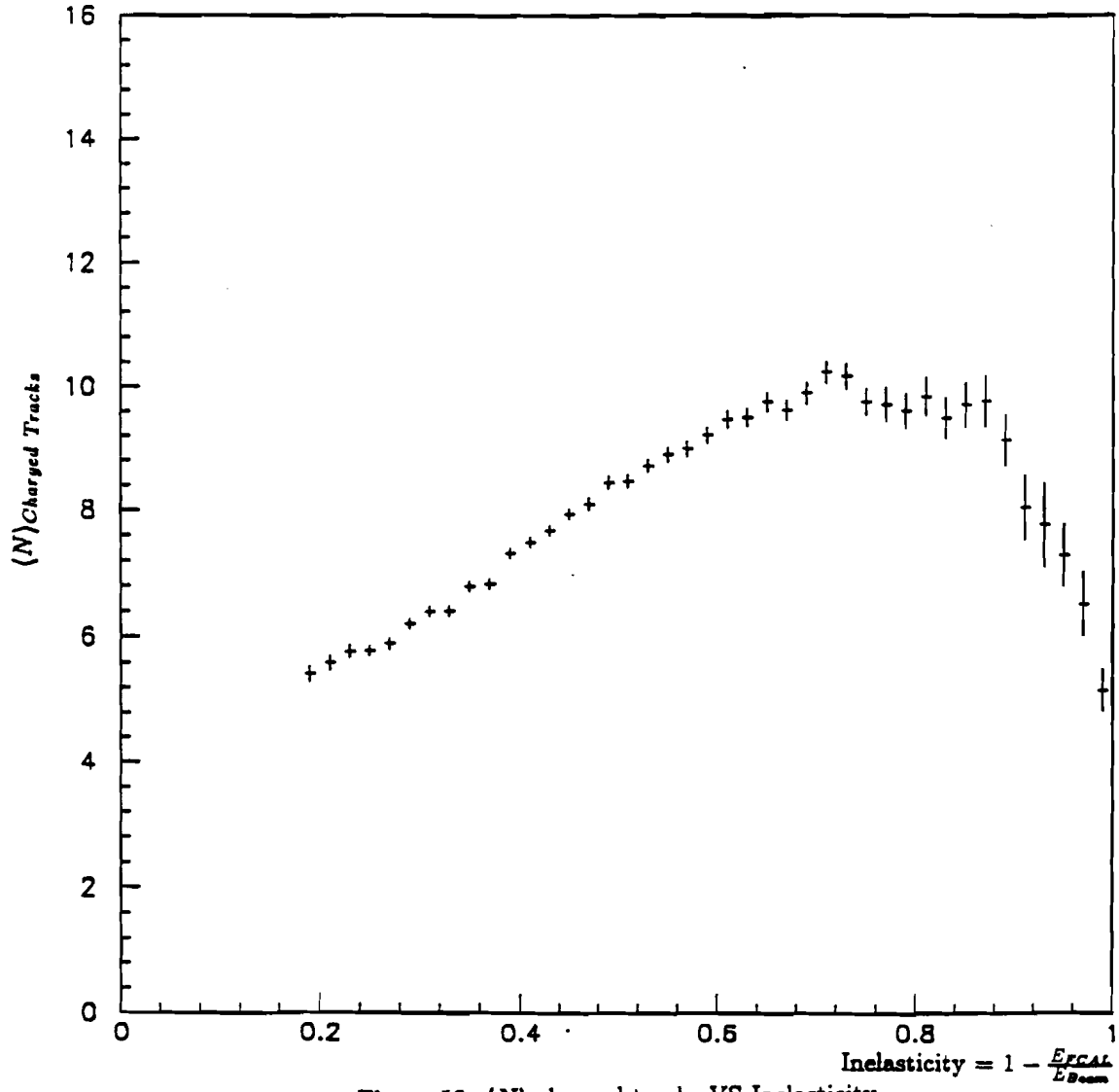

Figure 56: $\langle N \rangle$ charged tracks VS Inelasticity.

Figure 57: Charged Track Multiplicity Distribution.

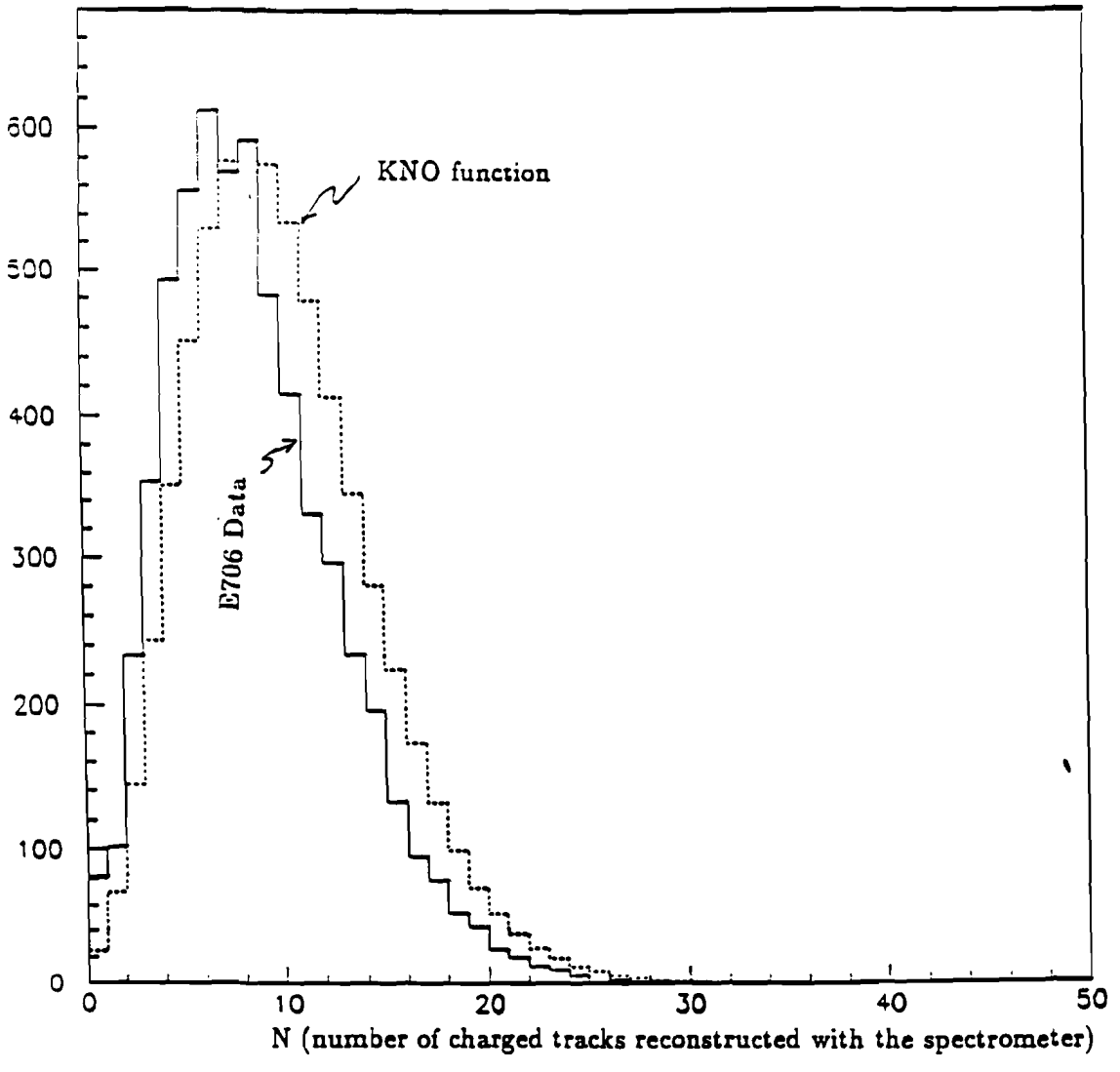

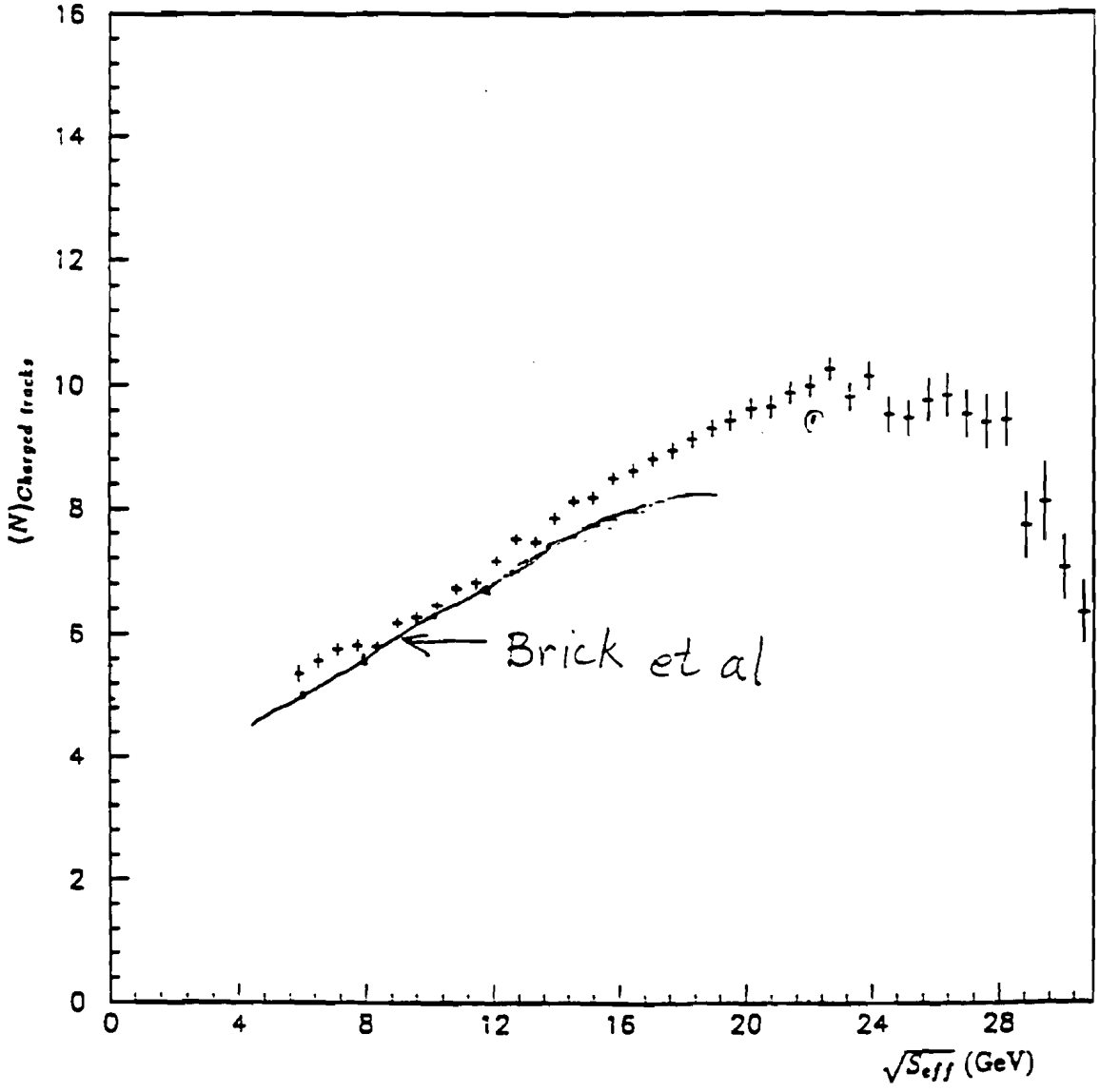

Figure 58: $\langle N \rangle$ charged tracks VS $\sqrt{S_{eff}}$.

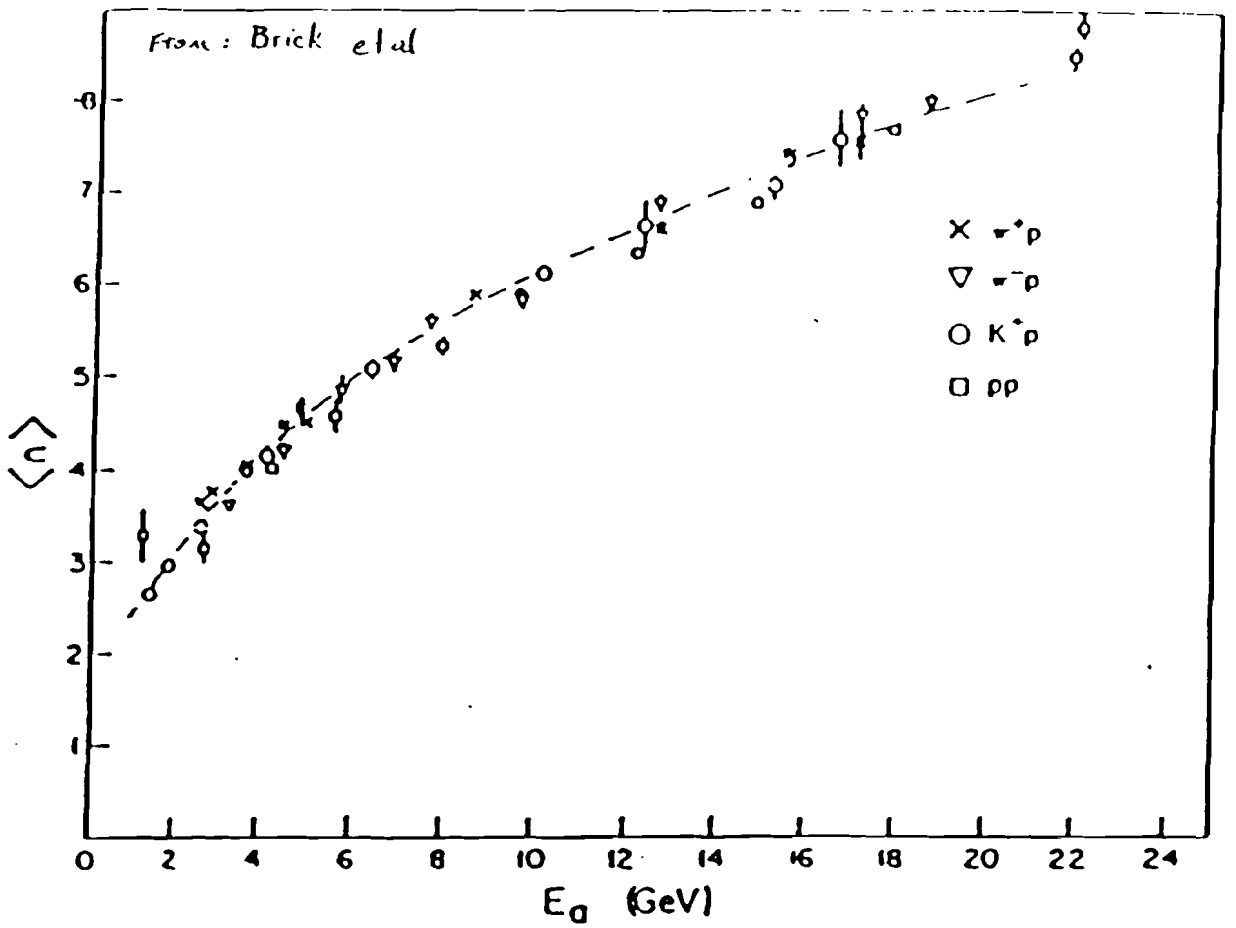

FIG.59 Average charge multiplicity $\langle n \rangle$ as a function of the available energy, $E_a = \sqrt{s} - (m_{\text{beam}} + m_{\text{target}})$, for $\pi^+ p$, $K^+ p$, and pp interactions.

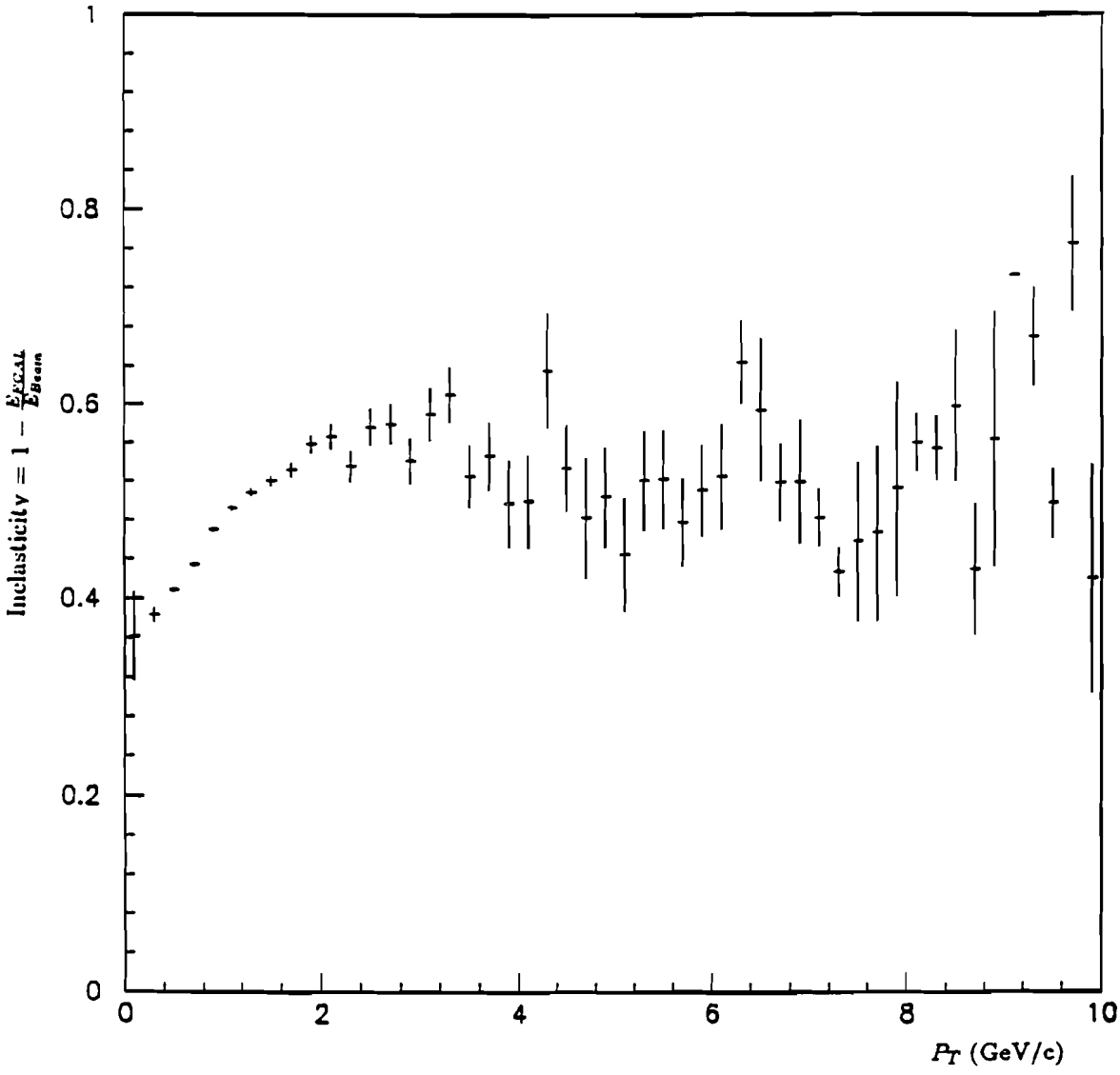

Figure 60: Inelasticity Vs P_T of the highest P_T charged track.

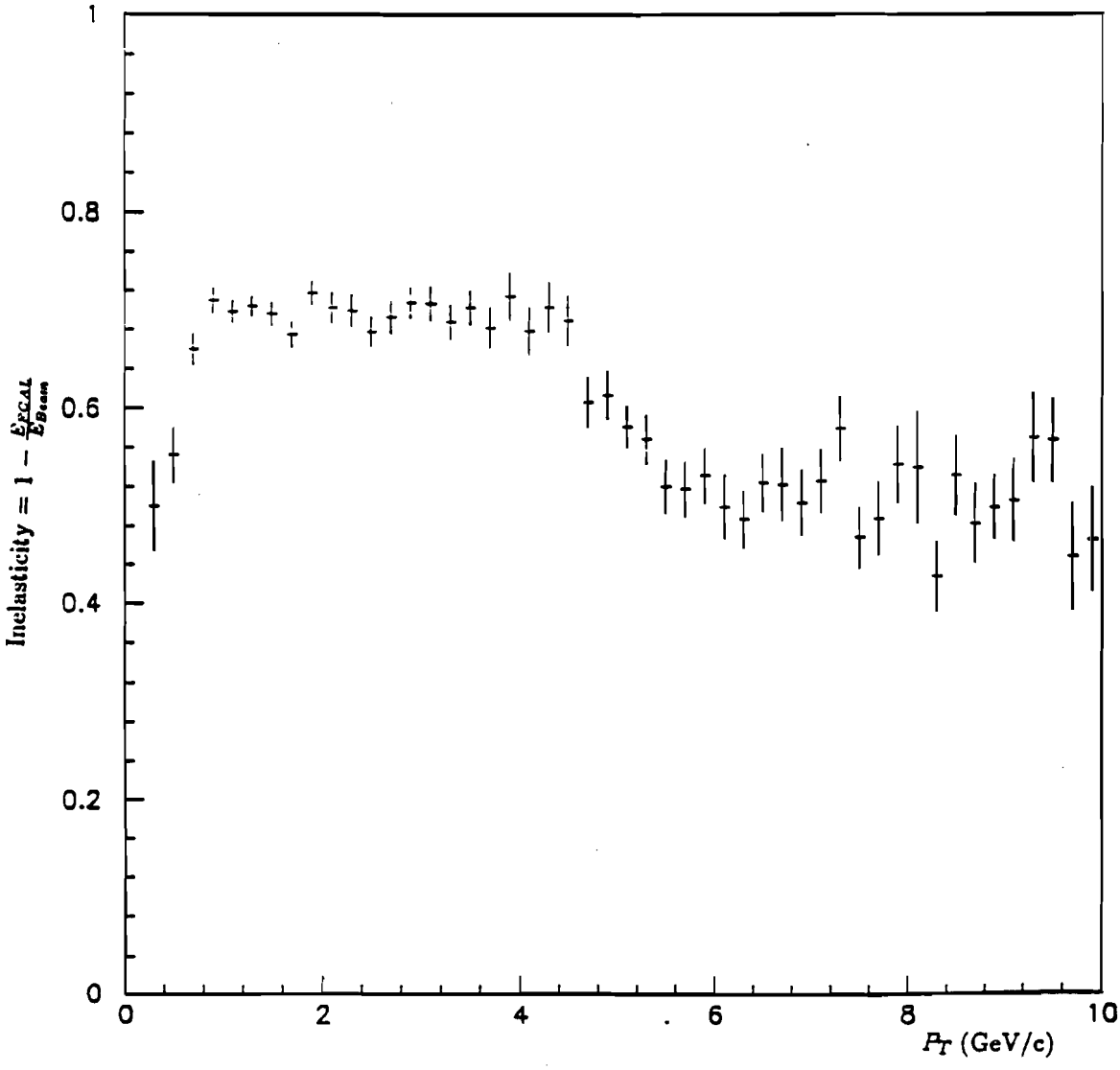

Figure 61: Inelasticity Vs P_T of the highest P_T photon.

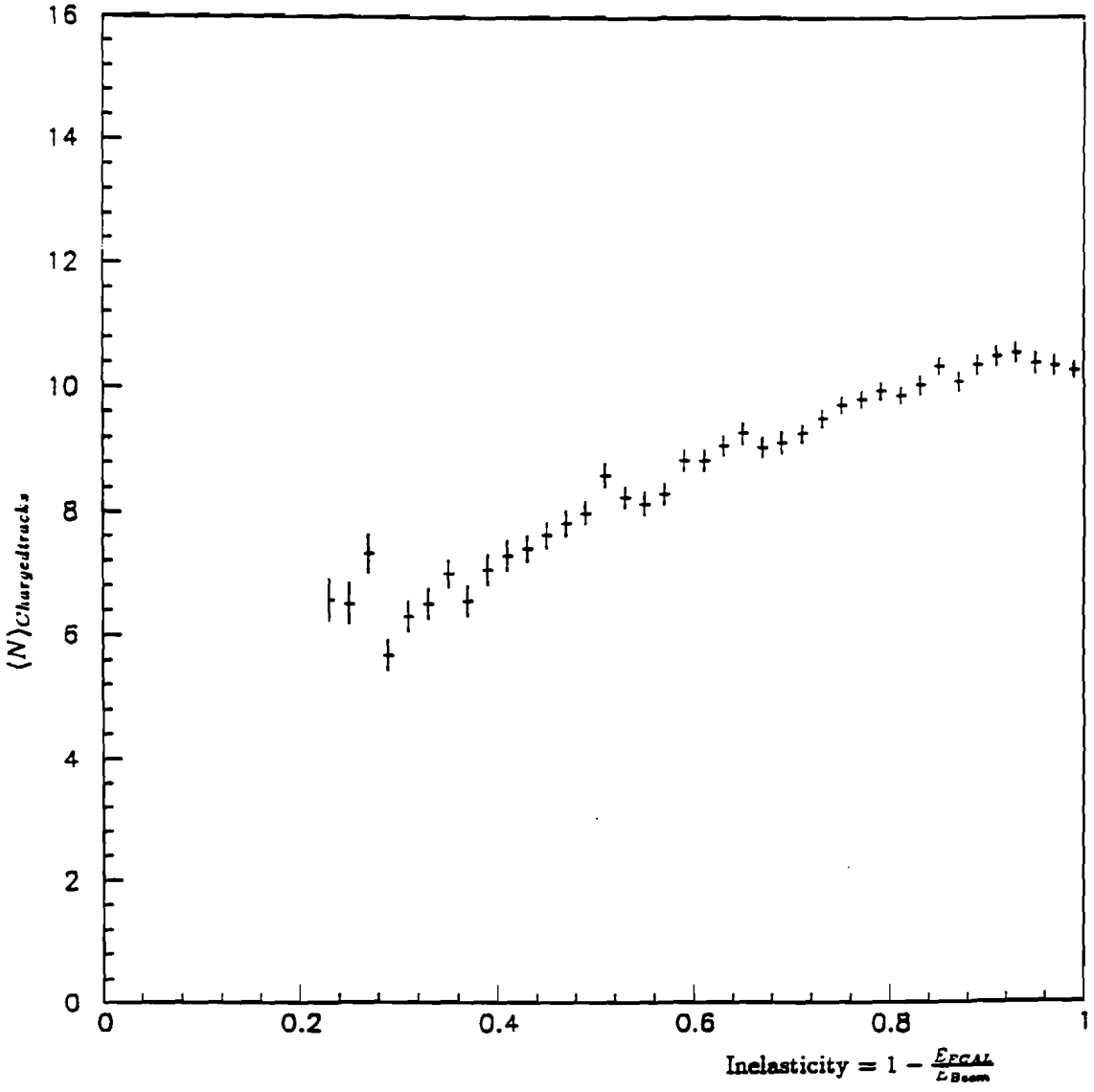

Figure 62: Number of charged tracks Vs Inelasticity.

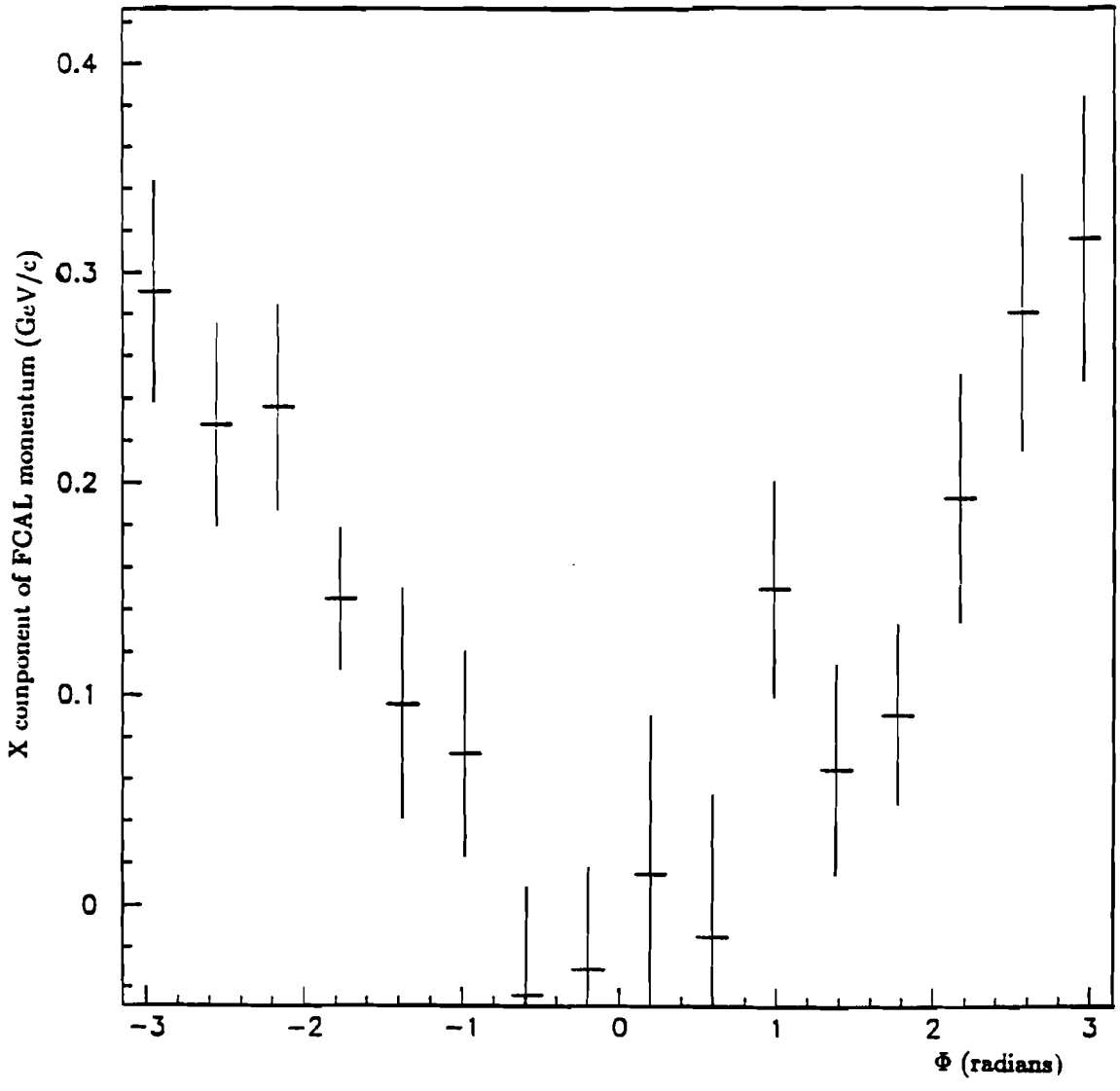

Figure 63: X component of FCAL momentum Vs Φ of the highest P_T photon.

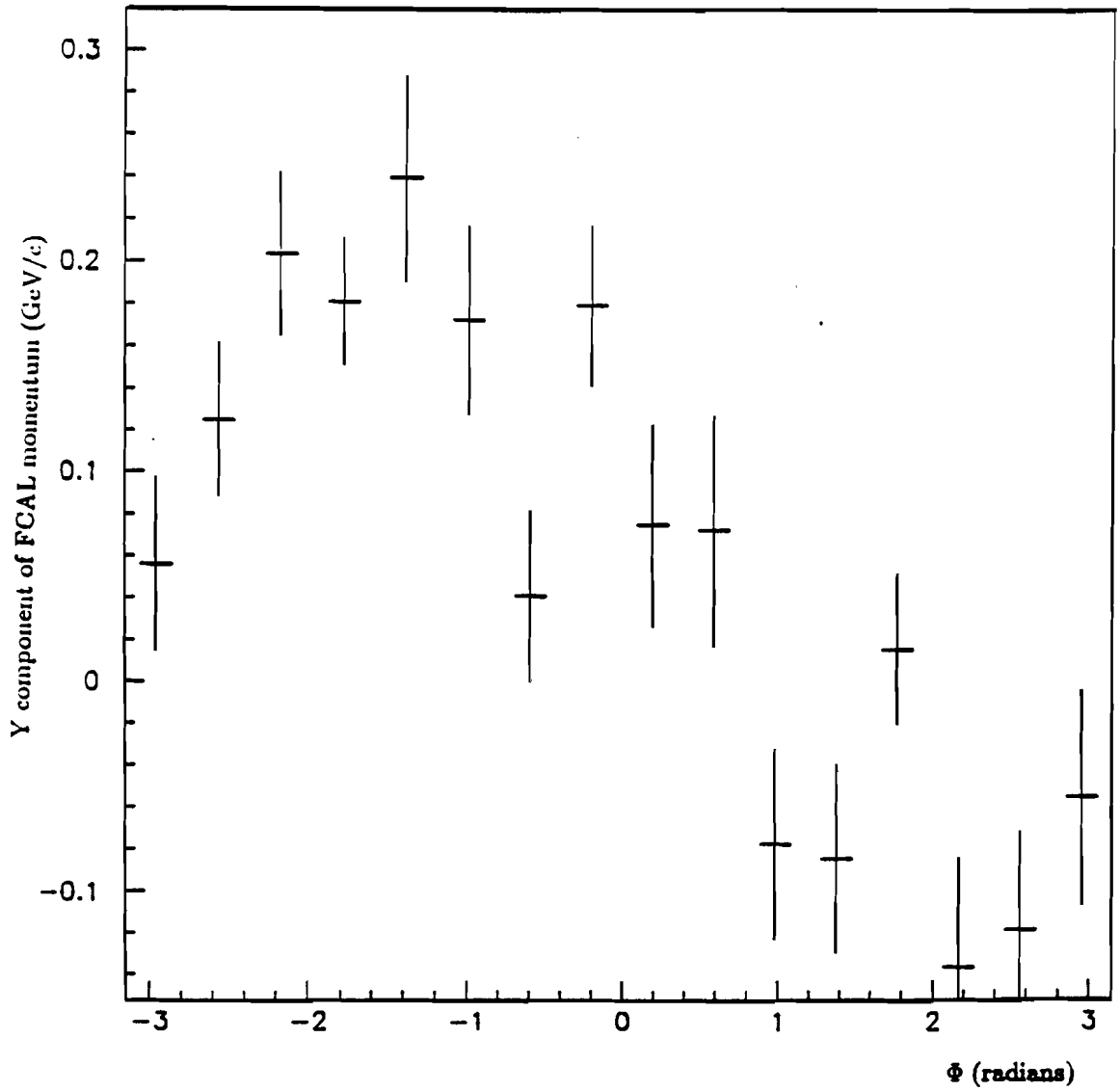

Figure 64: Y component of FCAL momentum Vs Φ of the highest P_T photon.

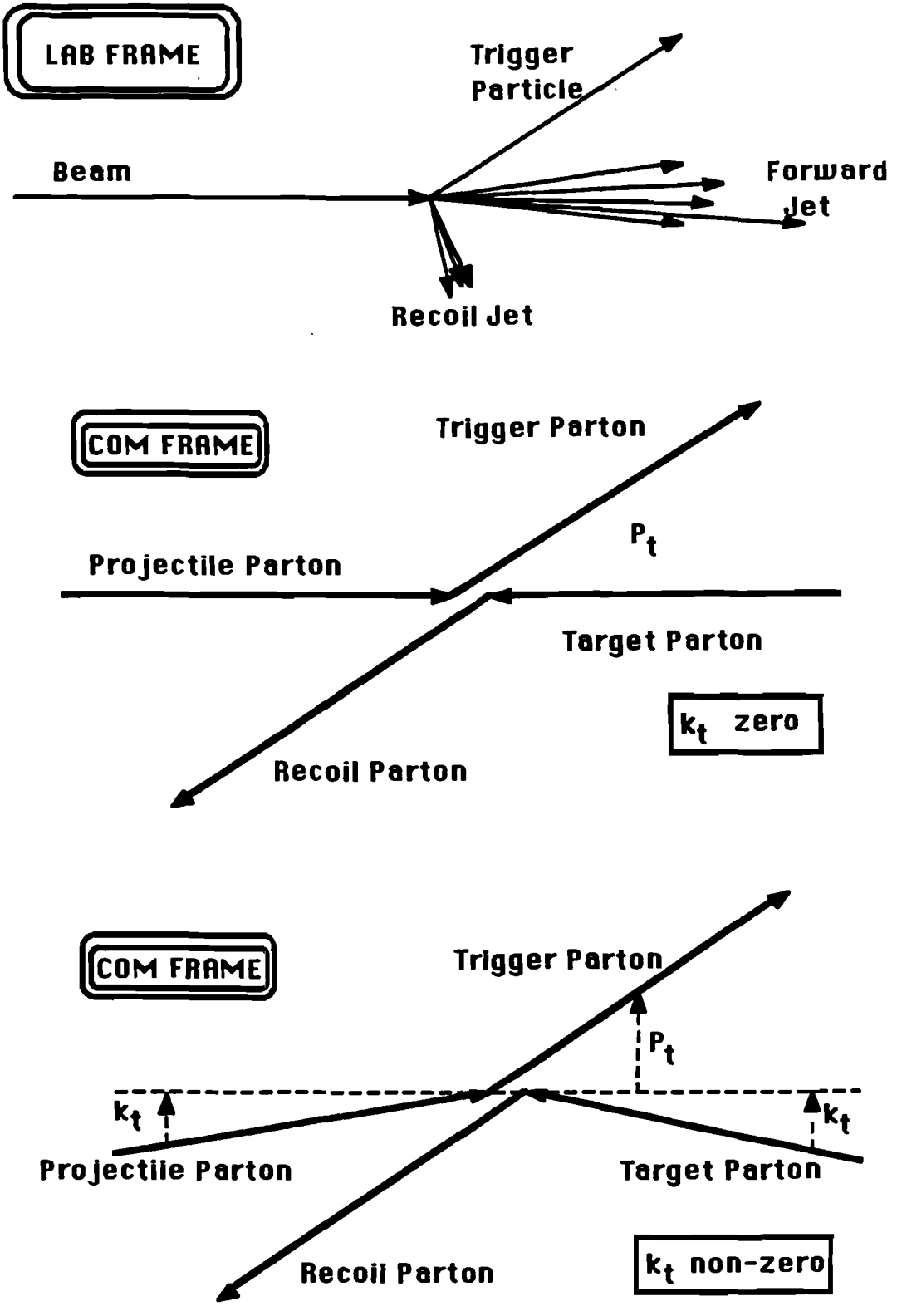

Figure 65: Hard Scattering Processes

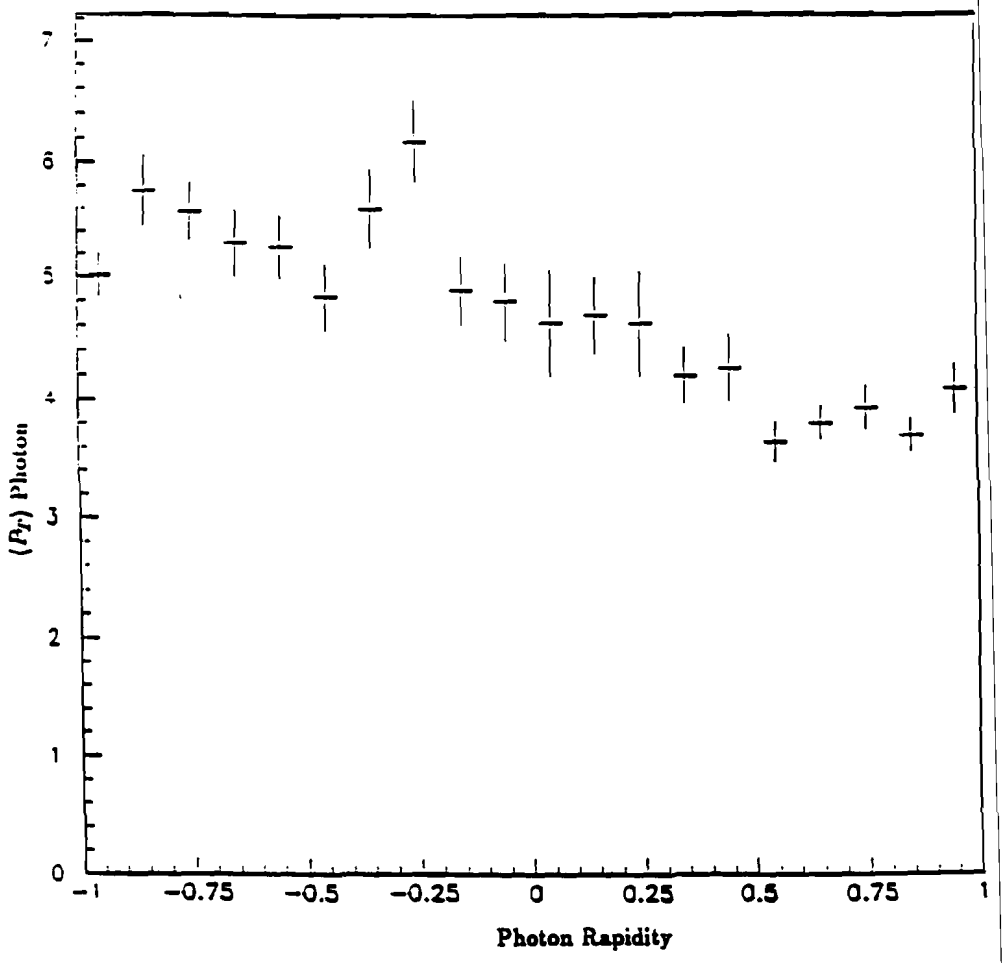

Figure 66: $\langle P_T \rangle$ Photon VS Photon Rapidity.

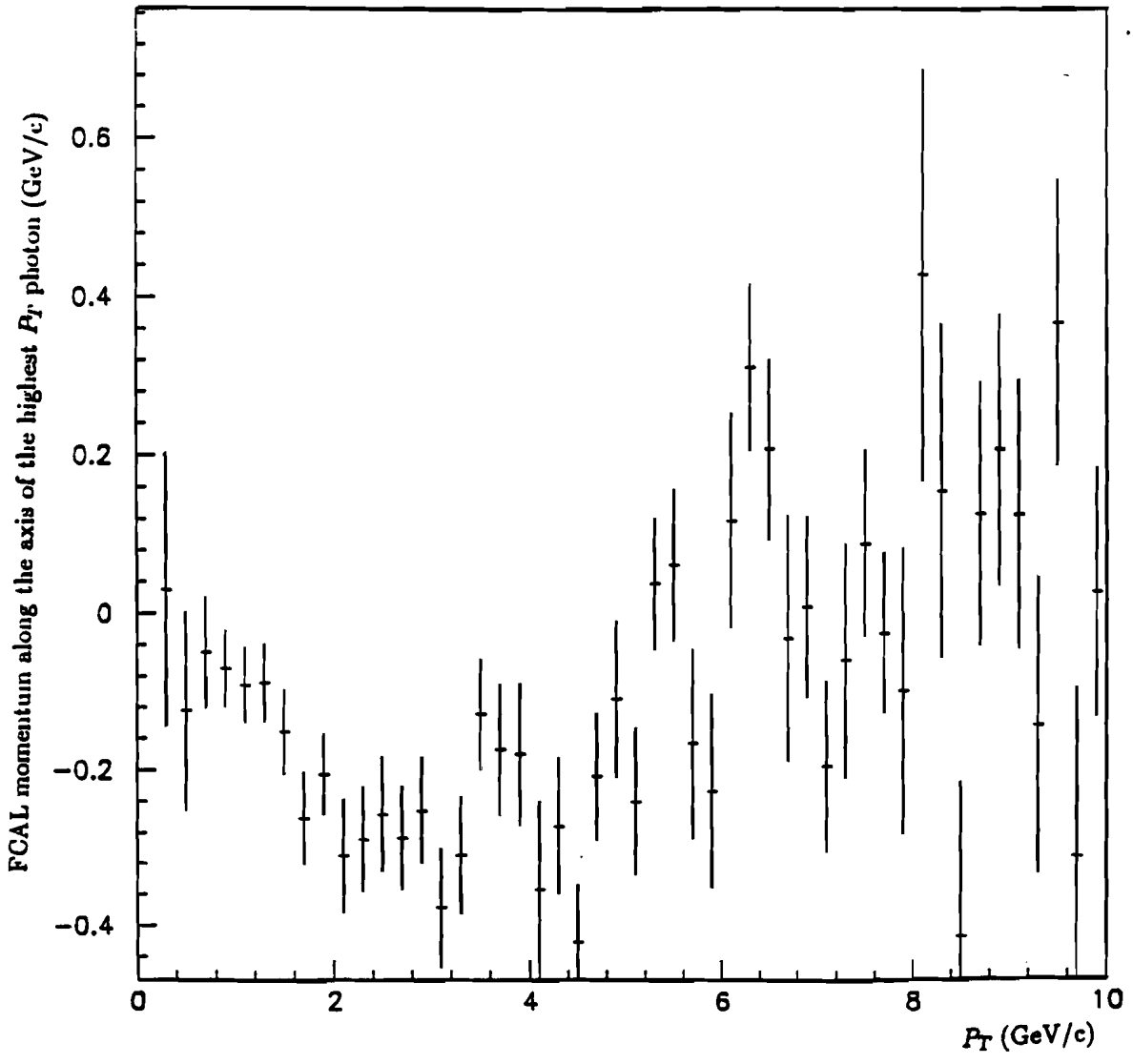

Figure 67: FCAL momentum along the axis of the highest P_T photon Vs P_T of the highest P_T photon.